

INFORMATION TO USERS

This reproduction was made from a copy of a document sent to us for microfilming. While the most advanced technology has been used to photograph and reproduce this document, the quality of the reproduction is heavily dependent upon the quality of the material submitted.

The following explanation of techniques is provided to help clarify markings or notations which may appear on this reproduction.

1. The sign or "target" for pages apparently lacking from the document photographed is "Missing Page(s)". If it was possible to obtain the missing page(s) or section, they are spliced into the film along with adjacent pages. This may have necessitated cutting through an image and duplicating adjacent pages to assure complete continuity.
2. When an image on the film is obliterated with a round black mark, it is an indication of either blurred copy because of movement during exposure, duplicate copy, or copyrighted materials that should not have been filmed. For blurred pages, a good image of the page can be found in the adjacent frame. If copyrighted materials were deleted, a target note will appear listing the pages in the adjacent frame.
3. When a map, drawing or chart, etc., is part of the material being photographed, a definite method of "sectioning" the material has been followed. It is customary to begin filming at the upper left hand corner of a large sheet and to continue from left to right in equal sections with small overlaps. If necessary, sectioning is continued again—beginning below the first row and continuing on until complete.
4. For illustrations that cannot be satisfactorily reproduced by xerographic means, photographic prints can be purchased at additional cost and inserted into your xerographic copy. These prints are available upon request from the Dissertations Customer Services Department.
5. Some pages in any document may have indistinct print. In all cases the best available copy has been filmed.

**University
Microfilms
International**

300 N. Zeeb Road
Ann Arbor, MI 48106

8415065

Fu, Tao-yi

**INFORMATION TRANSFER EFFICIENCY OF X-RAY IMAGE INTENSIFIER-
BASED IMAGING SYSTEMS**

The University of Arizona

PH.D. 1984

**University
Microfilms
International** 300 N. Zeeb Road, Ann Arbor, MI 48106

PLEASE NOTE:

In all cases this material has been filmed in the best possible way from the available copy. Problems encountered with this document have been identified here with a check mark .

1. Glossy photographs or pages
2. Colored illustrations, paper or print _____
3. Photographs with dark background
4. Illustrations are poor copy _____
5. Pages with black marks, not original copy _____
6. Print shows through as there is text on both sides of page _____
7. Indistinct, broken or small print on several pages _____
8. Print exceeds margin requirements _____
9. Tightly bound copy with print lost in spine _____
10. Computer printout pages with indistinct print _____
11. Page(s) _____ lacking when material received, and not available from school or author.
12. Page(s) _____ seem to be missing in numbering only as text follows.
13. Two pages numbered _____. Text follows.
14. Curling and wrinkled pages _____
15. Other _____

University
Microfilms
International

INFORMATION TRANSFER EFFICIENCY OF X-RAY
IMAGE INTENSIFIER-BASED IMAGING SYSTEMS

by

Tao-yi Fu

A Dissertation Submitted to the Faculty of the
COMMITTEE ON OPTICAL SCIENCES (GRADUATE)
In Partial Fulfillment of the Requirements
For the Degree of
DOCTOR OF PHILOSOPHY
In the Graduate College
THE UNIVERSITY OF ARIZONA

1 9 8 4

THE UNIVERSITY OF ARIZONA
GRADUATE COLLEGE

As members of the Final Examination Committee, we certify that we have read
the dissertation prepared by Tao-vi Fu

entitled Information Transfer Efficiency of X-Ray Image
Intensifier-Based Imaging Systems

and recommend that it be accepted as fulfilling the dissertation requirement
for the Degree of Doctor of Philosophy.

Eustace R. Beremak

2/20/84
Date

A. Slater

2/20/84
Date

Glenn Rodwin

2/20/84
Date

Date

Date

Final approval and acceptance of this dissertation is contingent upon the
candidate's submission of the final copy of the dissertation to the Graduate
College.

I hereby certify that I have read this dissertation prepared under my
direction and recommend that it be accepted as fulfilling the dissertation
requirement.

Eustace R. Beremak
Dissertation Director

Feb 20, 1984
Date

Glenn Rodwin
Co-Dissertation Director

2/20/84
Date

STATEMENT BY AUTHOR

This dissertation has been submitted in partial fulfillment of requirements for an advanced degree at The University of Arizona and is deposited in the University Library to be made available to borrowers under rules of the Library.

Brief quotations from this dissertation are allowable without special permission, provided that accurate acknowledgment of source is made. Requests for permission for extended quotation from or reproduction of this manuscript in whole or in part may be granted by the head of the major department or the Dean of the Graduate College when in his judgment the proposed use of the material is in the interests of scholarship. In all other instances, however, permission must be obtained from the author.

SIGNED:

A handwritten signature in cursive script, appearing to read "Larry J. ...", written over a horizontal line.

ACKNOWLEDGEMENTS

I would like to express my sincere appreciation to Dr. Hans Roehrig and Dr. Sol Nudelman for their enthusiastic support and encouragement during this study. Under their direction, I have learned much and shared the excitement in this growing research area of photo-electronic diagnostic imaging.

I am especially grateful to Mr. Charles West and Dr. Robert F. Wagner of the National Center for Devices and Radiological Health. The discussions and suggestions received from them have proven to be most valuable. Special thanks are extended to Mr. Richard Lamoreaux and Mr. Marvin E. Arthur for their assistance in preparing the experiments; and to Dr. Philip N. Slater and Dr. Eustace Dereniak for serving on my dissertation committee and providing helpful suggestions in the preparation of this dissertation.

I am greatly indebted to my parents and my wife for their long endurance and constant encouragement. Finally, I thank Ms. Jean Phillips and Ms. Norma Emptage for their outstanding efforts in editing and typing this final draft.

This work has been supported by the National Center for Devices and Radiological Health, Grant No. 5 R01 FD 00804, and the National Science Foundation, Grant No. ECS-7918518.

TABLE OF CONTENTS

	Page
LIST OF ILLUSTRATIONS.	vi
LIST OF TABLES	viii
ABSTRACT	ix
1. INTRODUCTION	1
The X-Ray Image Intensifier-Based System	1
Outline of Remaining Chapters.	5
2. EVALUATION CRITERIA.	7
Problem Definition	7
Observer Performance	8
Inherent Information	9
Maximum Displayed Information.	14
3. INFORMATION TRANSFER	17
Non-imaging Properties	17
Quantum Efficiency and Information Factor.	18
Physical Parameters Affecting DQE.	20
Imaging Properties	25
Image Signal Transfer.	25
Image Noise Transfer	28
Effect of Signal-Induced Background on DQE	32
4. EXPERIMENTAL METHODS	35
Non-imaging Properties	35
CsI Sensor Thickness	35
Pulse Height Distributions	38
X-Ray Source and Calibration	41
PMT Adaptor.	41
Analog Integrator.	44
Imaging Properties	47
Signal-Induced Background.	47
General Experimental Conditions.	49
Special Experimental Conditions.	54
Modulation Transfer Function	55
Algorithm of NPS Calculation	57

TABLE OF CONTENTS--Continued

	Page
5. RESULTS AND DISCUSSION.	62
Numerical Calculations.	62
Non-imaging Properties.	63
Scintillation Distribution.	63
Quantum Efficiency and DQE.	70
Imaging Properties.	73
Signal-Induced Background and X-Ray Scatter	73
Modulation Transfer Function.	76
Noise Power Spectrum.	78
Detective Quantum Efficiency.	92
Design Considerations	94
6. CONCLUSION.	105
Suggested Future Work	105
Summary	107
APPENDIX A: DERIVATION OF THE INFORMATION FACTOR RESULTING FROM AN X-RAY ENERGY DISTRIBUTION	109
APPENDIX B: THE NOISE POWER SPECTRUM OF A CASCADED LINEAR SYSTEM	112
REFERENCES.	123

LIST OF ILLUSTRATIONS

Figure		Page
1.1.	X-ray image intensifier-based digital imaging system. . .	2
1.2.	Analog components of an x-ray image intensifier system. .	4
3.1.	X-ray interactions in the CsI layer	23
3.2.	Influence of signal-induced background on the MTF	27
3.3.	Sources of signal-induced background in an XRII	33
4.1.	Experimental setup for CsI layer thickness measurement. .	36
4.2.	Schematic of pulse height distribution measurements . . .	40
4.3.	X-ray source, holder and collimator	43
4.4.	Integrator and pile-up detection circuit.	45
4.5.	Integrator control circuit.	46
4.6.	Schematic of contrast factor measurement.	50
4.7.	Timing diagram for exposure and camera operation.	52
4.8.	Schematic illustrating the noise power spectrum analysis.	58
4.9.	Noise images before and after subtraction of fixed pattern noise of output phosphor.	60
5.1.	Scintillation pulse height distributions for five XRIIs and five x-ray photon energies	64
5.2.	K-escape fraction as a function of CsI layer thickness. .	68
5.3.	X-ray spectra transmitted by various XRIIs.	69
5.4.	Multiple pulse height distribution as compared to Poisson distributions	71
5.5.	Contrast factor as a function of lead disc diameter . . .	74
5.6.	Modulation transfer function of the overall system and the XRII alone.	77

LIST OF ILLUSTRATIONS--Continued

Figure	Page
5.7. Modulation transfer function of the XRII for three x-ray spectra.	79
5.8. Modulation transfer function of the XRII in 4" and 9" modes	80
5.9. Noise power spectra due to x-ray and light exposure. . . .	81
5.10. NPS components of CsI layer, output phosphor, and camera tube	83
5.11. Noise power spectra resulting from high and low x-ray exposures.	85
5.12. Fitted noise power spectra for three x-ray spectra	87
5.13. NPS component of the CsI layer as compared with the system MTF ² in 9" mode.	88
5.14. NPS component of the CsI layer as compared with the system MTF ² in 4" mode.	90
5.15. Information transfer of the experimental system.	91
5.16. Noise power spectrum obtained without subtraction of fixed pattern noise.	93
5.17. Detective quantum efficiency of the CsI layer for three x-ray spectra.	95
5.18. Detective quantum efficiency of the experimental system. .	97
5.19. Information transfer of a typical clinical system.	99
5.20. Modulation transfer function of the XRII and a typical clinical system.	101
5.21. Square wave response of selenium vidicon	103

LIST OF TABLES

Table	Page
4.1. X-Ray Source Lines and Associated Flux Levels (Collimator diameter: 2mm)	42
5.1. First-order Statistical Parameters of Photo-peak Distributions (XR11: Thomson-CSF compact).	66
5.2. Summary of Non-imaging Properties of Five XR11s for Five X-ray Energies	72
5.3. Background Energy Fractions for two Magnification Modes and Three X-ray Spectra	75
5.4. Cumulative Quantum Gain at Each System Component (Mean Deposited X-ray Photon Energy: 41 keV)	84
5.5. Measured and Calculated DQE for Three X-ray Spectra (XR11: Thomson-CSF compact, CsI = 71.7 mg/cm ² , Pyrex window = 750 mg/cm ²).	96

ABSTRACT

The information transfer efficiency of any quantum detection imaging system can be described by a unique measure: the detective quantum efficiency [DQE(f)], which is a function of the statistically independent frequency channels. The DQE(f) is a combined descriptor which takes into account the signal transfer as well as noise transfer properties of a complete system. For a complicated multistage imaging system, each system component contributes noise. In this dissertation, physical and mathematical models for noise analysis are developed and verified experimentally with an x-ray image intensifier (XRII)-based imaging system.

In such a system, the DQE at low frequency range is primarily determined by the x-ray detection and scintillation processes at the CsI layer of the XRII. The effects of x-ray photon energy and sensor layer thickness on DQE are measured in detail. Numerical calculations based on a physical model of x-ray interactions show a general agreement with the experimental data. At higher frequencies, the DQE behavior becomes more complicated. A mathematical model which combines the micro-image properties and noise statistics is formulated to analyze the noise power spectrum (NPS) of a linear n-stage imaging system. Measurement of NPS components of an XRII system verifies the validity of this analytical prediction. The associated image transfer properties are also measured with emphasis on the effect of signal-induced background on the image information

transfer. The low frequency data derived from these image property measurements show further agreement with the numerical calculations based on the physical model. As a result of this predictability of information transfer efficiency, system gain and recording capacity are emphasized in the design consideration of a projected high performance XRII radiographic system.

CHAPTER 1

INTRODUCTION

Recent advances in the development of photoelectronic imaging devices (PEID) and of digital data storage devices have led to a potential alternative to the commonly used screen-film system in diagnostic radiology. Extensive research and development programs based on this concept of photoelectronic-digital radiology (PE-DI-R) have been undertaken at the University of Arizona since 1973 (Nudelman, 1983). The very first approach to this idea was brought into clinical application as digital subtraction angiography (DSA) (Christenson et al., 1980). Such a system has been proven to be of tremendous diagnostic value as applied to both intravenous and conventional angiography. Resulting from the success of various digital imaging modalities such as computed tomography, nuclear magnetic resonance, and DSA, the concept of the photoelectronic radiology department has emerged (Capp et al., 1981). However, new PEID systems must be developed to meet the more stringent requirements of general diagnostic procedures. It is the underlying motivation of this study to develop and apply quantitative evaluation criteria for the design of such new systems.

The X-Ray Image Intensifier-Based System

A typical x-ray image intensifier (XRII)-based digital system is shown in Figure 1.1. The acquisition system can be divided into

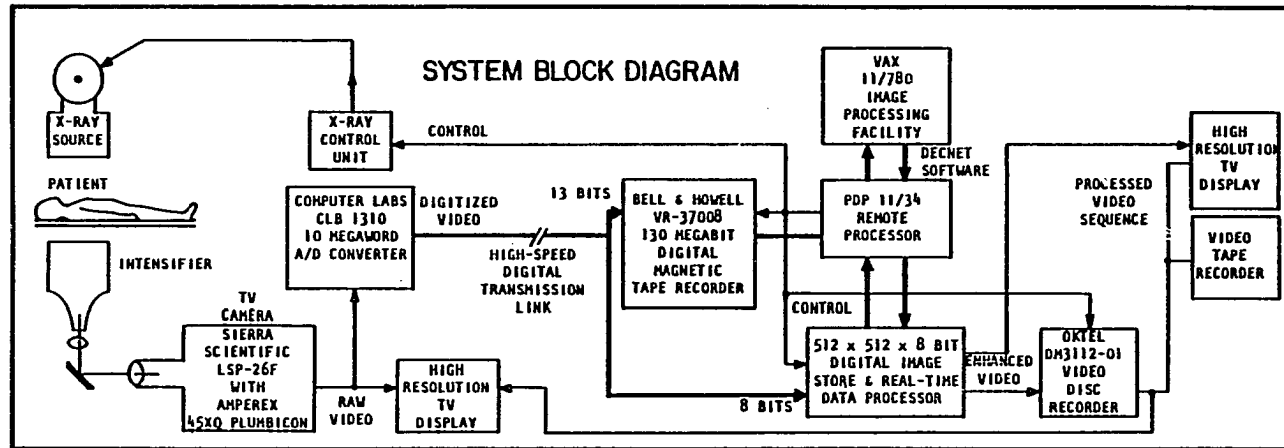


Fig. 1.1. X-ray image intensifier-based digital imaging system.

two main paths, analog and digital. While the analog path determines the image information transfer, once digitized, the image can be stored, processed, or distributed without introducing further degradation. The analog acquisition components include a cesium iodide (CsI) XRII optically coupled by a tandem lens to a video camera tube, as shown in Figure 1.2. The XRII is the primary component, as it converts the x-ray photon image to an intensified visible image at its output phosphor. Image conversion begins at the CsI sensor where each detected x-ray photon is converted into a burst of light comprising approximately two thousand individual scintillations. This light burst propagates to the adjacent photoemissive layer and generates photoelectrons. Those electrons are then accelerated and imaged by the electron optics onto the output phosphor. Bombarded by such high energy electrons, the output phosphor releases bursts of light pulses to form a minified visible image with a typical luminous gain of on the order of two thousand. This smaller output image format is essential for ease in optical coupling to the final image recording device, a 45XQ Plumbicon in this case. This video tube features linear response, low dark current, and low lag with its spectral response matched to the phosphor emission spectrum. A tandem lens configuration is used to achieve maximum optical collection efficiency. Both lenses are specifically designed for the XRII system by taking into consideration the substrate and spectral emission of the output phosphor.

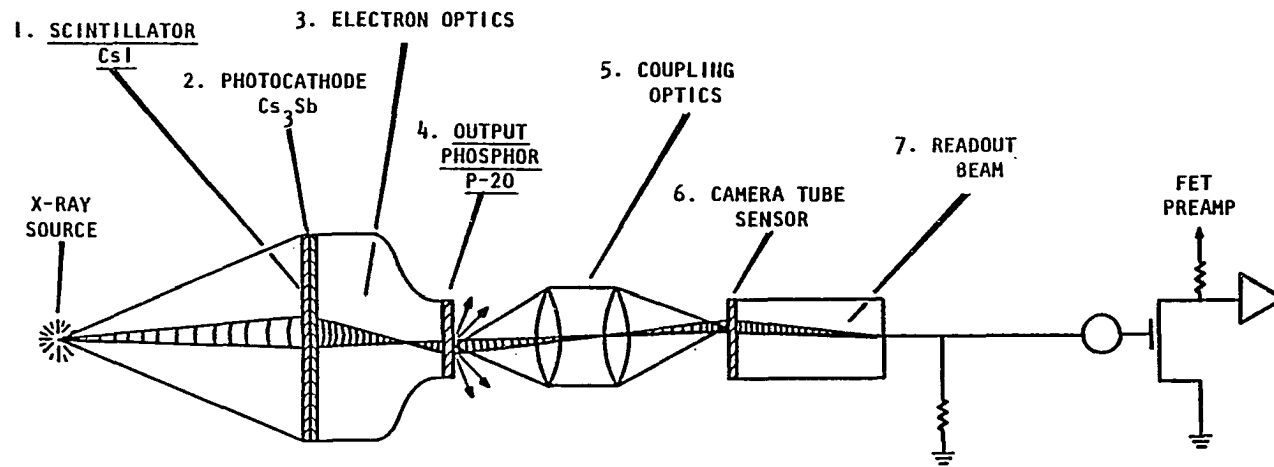


Fig. 1.2. Analog components of an x-ray image intensifier system.

The video signal generated feeds into a 10 megaword A/D converter with 13 bit accuracy, where the image enters its digital path. Only eight bits of the digitized signal are stored in real time into a 512X512 CCD digital memory. Mapping memories are incorporated at both input and output ends of the CCD memory to perform flexible data transformations in real time, such as contrast stretching and windowing functions. This buffered image is then transferred to the VAX11/780 image processing facility at a rate of one frame/second. The x-ray exposure and the camera operation are controlled by a micro-processor unit. Image subtraction, filtering, and other processing options are initiated once all image frames are stored in the host computer.

Outline of Remaining Chapters

Information transfer efficiency as a system evaluation criterion is defined in Chapter 2 following a general survey of the literature regarding the relationship between image quality and observer performance. A link between the physical measure of information transfer efficiency and the visual performance of a specific task is established. In Chapter 3, mathematical analyses of factors affecting information transfer efficiency are formulated, which also serve as a guideline for experimental investigations discussed in Chapters 4 and 5. Experimental methods for measuring imaging and non-imaging properties of the system are specified in Chapter 4. Results and implications for system design considerations based on theoretical models as well as experimental evidence will be discussed in Chapter

5. Chapter 6 concludes this study with suggestions for further work and a brief summary.

CHAPTER 2

EVALUATION CRITERIA

Due to the digital format of the stored image, a radiologist may increase his diagnostic accuracy through use of a proper processing algorithm. However, there exists a limited amount of inherent information which sets an upper limit on the diagnostic value of the image. It is the purpose of this chapter to define such inherent information to serve as basic criteria for system evaluation.

Problem Definition

The human observer is the most unpredictable component in a complete image system. It is a common experience that a faint object is more difficult to detect if it is located in a structured background than in an isolated position. Therefore, one can distinguish two disturbing sources in human perception process: clutter noise (structure noise) and random noise. For example, the bone and tissue structures form the clutter noise in angiography which involves the detection of occlusions in blood vessels. Their removal by subtraction has led to the success of digital subtraction angiography (DSA). However, while the clutter noise is completely removed from the area of interest to increase object detectability, the subtraction process effectively increases the random noise as the noise contents of the constituent images are added independently. To evaluate an imaging system, only random noise is considered. The simplicity

of the DSA imagery is emphasized here because it helps us to reach the definition of the inherent information along a more logical path starting from the visual perception problem.

Observer Performance

Since the invention of low-light-level electro-optical sensors, much attention has been focused onto the visual perception problems concerning the imagery produced by such sensitive devices. Rose (1948) considered such a problem and realized the fundamental limitation on visual perception, namely the statistical nature of the information-carrying photons. His fluctuation theory forms the basis for predicting the ultimate visual performance for all low-light-level applications today. Since that time, numerous research efforts have been conducted to correlate the visual performance to physical merit functions of a practical electro-optical system. Johnson (1958) defined four levels of discrimination tasks and experimentally determined the equivalent resolutions required per object dimension against their corresponding visual tasks. These so-called "Johnson criteria" have been of practical value even though noise characteristics were not considered. Another practically used merit function in photographic sciences is the Modulation Transfer Function Area (MTFA) originally proposed by Charman and Olin (1965). Although this figure of merit takes into consideration both signal and noise characteristics of the imaging system, quantitative interpretation is hardly obtained for our purpose. Extending Rose's fluctuation theory, Rosell (1969) developed a more quantitative display signal-to-noise ratio $[(S/N)_d]$

concept to quantify an imaging system. Based on this concept, Rosell and Willson (1973) conducted a series of psychophysical experiments using noisy televised images to correlate this merit function to the visual tasks defined by Johnson. The $(S/N)_d$ required for 50% detection probability was determined to be about three, which was in a good agreement with that predicted by binary decision theory. Due to its high reliability and ease in calculation, the $(S/N)_d$ will be adopted in our discussion as a link between system information and detectability for a specific object.

Inherent Information

All the merit functions discussed so far relate to the displayed image presented directly to an observer. As noted earlier, a displayed image can be optimized by suitable processing of the inherent information. The physical measure of such information should be defined and related to the display signal-to-noise ratio.

Modern image analysis methods are largely adopted from the statistical communication theories developed in parallel by Wiener (1949) and Shannon (1948). It was Fourier analysis which formed the mathematical basis for their pioneering theories. This Fourier domain analysis has an important implication in problem regarding inherent information. As the result of a fundamental theorem in communication theory (Fano, 1968), an imaging system can be viewed as though it were composed of a series of statistically independent frequency channels. Each channel is completely characterized by its image signal and noise transfer properties. Any linear

transformation in space, such as filtering and contrast stretching, preserves this statistical independence. The effect of such a transformation on each image channel is to scale both signal and noise by the same factor. Therefore, an invariant quantity under such transformation can be realized if it is defined as a function which depends only on the ratio of those two properties. One can infer that "inherent" information and information efficiency must be defined in such a way.

So far, the term "information" has been used without precise definition. However, a scientific measure of information exists. It was defined by Shannon (1948) as the statistical entropy of an ensemble of finite discrete messages. This concept forms the framework of so-called "information theory." This theory is primarily concerned with the optimum distribution of a given number of messages to statistically independent frequency channels of known characteristics for transmission. Along this line, an integral performance index, called "channel capacity," was quantitatively defined to characterize a physical transmission channel. This quantity gives the limit on the absolute information attainable through such a channel and it can be reached theoretically only when the message is optimally distributed. When adopted to the evaluation of imaging devices, this integral performance index is of little value since the scene to be imaged cannot be artificially coded into the available frequency channels. As MTF is a better descriptor than "resolution," the

frequency-dependent information capacity is superior to channel capacity when information theory is applied to the imaging system evaluation.

Following the arguments in this section, one reaches the evaluation criteria for a quantum imaging system: the noise equivalent quanta [NEQ(f)] and the detective quantum efficiency [DQE(f)], both as a function of spatial frequency. The DQE concept was originated from Rose (1946) for a non-imaging quantum detector and subsequently was extended to imaging detectors by Dainty and Shaw (1974) with the introduction of NEQ. In its original form, the DQE was defined as

$$\text{DQE} = \frac{(\text{S/N})_{\text{out}}^2}{(\text{S/N})_{\text{in}}^2} \quad (2.1)$$

Here, the signal-to-noise ratio square is used to represent the information provided at input and output of the detector. Assuming that the input quantum stream has a Poisson distribution about a mean quantum number, n_0 , during the observation time, the input signal-to-noise ratio square is

$$(\text{S/N})_{\text{in}}^2 = n_0 \quad (2.2)$$

Similarly the output information can be represented by an equivalent quantum stream with mean number NEQ for the same observation time

$$\text{NEQ} = (\text{S/N})_{\text{out}}^2 \quad (2.3)$$

This leads to the following equation for the DQE

$$\text{DQE} = \frac{\text{NEQ}}{n_0} \quad (2.4)$$

This can be interpreted as the effective quantum utilization efficiency as though the detector acts as an ideal photon counter with somewhat degraded detection ability.

When these interpretations are extended to the frequency channels of an imaging detector, a conceptual problem may arise. In talking about signal-to-noise ratio, one usually refers to the "signal" as a deterministic quantity, that is the mean value; and the "noise" as the random fluctuation around that mean value. The noise power spectrum is generally used to characterize the noise in the frequency channels. It is not defined if the input quantum stream is not stationary. However, a stationary quantum stream carries no pictorial information. Therefore, it seems that the signal and noise cannot be defined at the same time. One practical solution to this problem is to assume a very small image modulation so that the stationary condition can be approximated. In addition to this, one realizes that the DQE and NEQ both measure the equivalent quantum utilization ability of a detector. One can therefore characterize the signal of a frequency channel by its signal transfer ability, MTF, which is independent of the deterministic input signal strength.

On the other hand, the noise is similarly characterized by a relative quantity, $W_{\Delta z/z}(f)$, the noise power spectrum of the relative fluctuation $\Delta z/z$, where z stands for the observable output of the system. A further advantage of using such a relative quantity is that the power spectrum is independent of the physical unit of the system output. In particular, for a linear system, the output noise spectrum can be directly transformed into its input equivalence,

$$\frac{\Delta z}{z} = \frac{\Delta q}{q} ,$$

$$W_{\Delta z/z}(f) = W_{\Delta q/q}(f) ,$$
(2.5)

where q stands for the equivalent input quantum fluence.

By forming the ratio of the relative signal power and the noise power, the NEQ(f) is defined

$$NEQ(f) = \frac{MTF^2(f)}{W_{\Delta q/q}(f)} .$$
(2.6)

It should be pointed out that NEQ(f) has units of quanta/area as opposed to its non-imaging counterpart NEQ (Equation 2.3) which uses units of quanta. This can be explained by the fact that pictorial information is represented as density differences instead of a single number. By forming the ratio between NEQ(f) and the incident quantum fluence q_0 , as in Equation 2.4, one obtains the DQE(f),

$$\begin{aligned}
 \text{DQE}(f) &= \frac{\text{NEQ}(f)}{q_0} \\
 &= \frac{\text{MTF}^2(f)}{q_0 W_{\Delta q/q}(f)} \quad . \quad (2.7)
 \end{aligned}$$

From the discussion early in this section, both $\text{NEQ}(f)$ and $\text{DQE}(f)$ are invariant under a linear transformation since they are defined by the ratio of the two channel characteristics. In other words, they are inherent to the system. At this point, it should be pointed out that the DQE is a unitless quantity, and therefore

$$\text{DQE} = \text{DQE}(f=0) \quad , \quad (2.8)$$

where DQE is the quantity obtained when the imaging system is operated as a non-imaging detector. For clarity, the frequency-dependent quantity is termed "image DQE" as distinguished from the simple "DQE" which characterizes the non-imaging properties.

Maximum Displayed Information

As pointed out earlier in this chapter, the displayed image can be optimized by properly processing the inherent information. As well, Rosell's display signal-to-noise ratio $[(S/N)_d]$ correctly predicts the visual performance. The remaining problem is then how to maximize the $(S/N)_d$ from the inherently recorded information. As implied in Rose's fluctuation theory, the eye-brain system performs

a matched filtering process on a noisy object as the detection threshold is approached. Based on this assumption on the eye-brain system, Sandrik and Wagner (1982) showed that the $(S/N)_d$ can be maximized by pre-whitening the noise. Under this processing algorithm, the $(S/N)_d$ is given by

$$(S/N)_d^2 = C^2 q_o \int |S(f)|^2 DQE(f) df, \quad (2.9)$$

where C is the object contrast,

q_o is the incident photon fluence, and

$|S(f)|^2$ is the power spectrum of an object with normalized peak amplitude.

Here the squared $(S/N)_d$ is used in order to link it to the information concept as implied in the NEQ definition (Equation 2.3). We may therefore call it "displayed information" for brevity from now on.

For a disk, square, or any shape of object with uniform amplitude, this equation can be written as

$$(S/N)_d^2 = C^2 q_o a \frac{\int |S(f)|^2 DQE(f) df}{\int |S(f)|^2 df} \quad (2.10)$$

where a is the object area.

This particular form is of great interest to illustrate the interplay between the $DQE(f)$ and the object spectrum $S(f)$ on the displayed information. For an ideal image detector where $DQE(f)$ is unity, Equation 2.10 is in the same form as given by fluctuation theory.

This is the amount of information carried by the primary quanta in the object. For a real detector, the efficiency for detecting a particular object is then the DQE averaged over the object power spectrum. It is the image DQE, instead of the MTF, that determines the ability to detect object detail. A term "information bandwidth" can then be defined as the cutoff frequency where the image DQE falls to a certain percentage of its zero-frequency value. Of equal importance is the magnitude of the image DQE at zero frequency. From Equation 2.8, this value can be obtained experimentally by operating the imaging system as a non-imaging detector. In the following three chapters, these imaging and non-imaging properties on information transfer efficiency will be studied both analytically and experimentally.

CHAPTER 3

INFORMATION TRANSFER

As discussed in the last chapter, pictorial information is transmitted through statistically independent image channels characterized by their signal (MTF) and noise (NPS) transfer properties. In this chapter, various physical processes which contribute to the system noise will be examined first by ignoring the imaging capability of the system. This analysis provides greater physical insight as to how the magnitude of image DQE is affected. In a subsequent mathematical treatment, imaging properties, such as system MTF and NPS, are explored to derive the transfer efficiencies of the image channels. The effect of signal-induced background on information transfer will also be discussed. Poisson statistics on the primary quantum stream is assumed in all theoretical treatments for this dissertation.

Non-imaging Properties

In an XRII, various high gain quantum conversion processes occur which generate a burst of light pulses following the detection of a primary x-ray photon. The number of such light pulses is subjected to a random distribution because of the statistical nature of the underlying physical processes. A spatial density distribution of those recorded statistical units represents the pictorial information originally carried by the incident x-ray photon stream. Ignoring

the image feature, the only information provided by the system is the total number of counts on those secondary events.

Quantum Efficiency and Information Factor

Let us first imagine that the recording device has a counting ability to distinguish each and every statistical unit transmitted by the system. Each detected x-ray photon would be registered as a single event. The resulting signal-to-noise ratio is given by the well-known Poissonian relation

$$(S/N)_{\text{out}} = \sqrt{\eta n_0} \quad , \quad (3.1)$$

where n_0 is the mean number of the incident x-ray photons, and η is the quantum efficiency of the x-ray sensor. Using Equations 2.1 and 2.2, the DQE is given simply by

$$\text{DQE} = \eta. \quad (3.2)$$

However, XRII systems are commonly operated by integrating the secondary events rather than counting the primaries. Therefore, the statistical fluctuations due to the gain mechanisms contribute to additional uncertainty. Let us denote the mean gain provided by the system by μ_s and the associated variance by σ_s^2 , then the mean μ , variance σ^2 , and the S/N of the output are given by

$$\begin{aligned} \mu &= n_0 \eta \mu_s \quad , \\ \sigma^2 &= (\eta n_0) \mu_s^2 + (\eta n_0) \sigma_s^2 \end{aligned}$$

$$= \eta n_0 (\mu_s^2 + \sigma_s^2) ,$$

$$(S/N)_{\text{out}}^2 = \eta n_0 \frac{\mu_s^2}{\mu_s^2 + \sigma_s^2} . \quad (3.3)$$

The DQE for this integrating mode is thus given by

$$\text{DQE} = \eta \frac{\mu_s^2}{\mu_s^2 + \sigma_s^2} \quad (3.4)$$

$$= \eta I .$$

The quantity I , called "information factor," was first introduced by Swank (1973) in dealing with the noise properties of various types of x-ray phosphors. It was originally defined in an equivalent form

$$I = \frac{M_1^2}{M_0 M_2} \quad (3.5)$$

due to the simplicity of its calculation from the measured pulse height distribution. Here M_i stands for the i^{th} moment of the distribution. For a cascaded system, the statistics of the resultant burst of secondaries is derived from several independent statistical laws. Since the information factor specifies any statistical distribution in the information sense, it can be used either for each individual physical process or a combination of such processes. However, it should be noted that individual information factors cannot simply

be cascaded in a system. As a special case at zero frequency in Appendix B, the information factor of a complete system can be expressed as

$$\begin{aligned} \frac{1}{I} = & \frac{1}{I_1} + \frac{1}{\bar{m}_1} \left(\frac{1}{I_2} - 1 \right) + \frac{1}{\bar{m}_1 \bar{m}_2} \left(\frac{1}{I_3} - 1 \right) \\ & + \dots + \frac{1}{\bar{m}_1 \dots \bar{m}_{n-1}} \left(\frac{1}{I_n} - 1 \right) , \end{aligned} \quad (3.6)$$

where I_i and \bar{m}_i are the information factor and the mean gain at the i^{th} stage, respectively. From this expression, the information factor of the whole system may be approximated by a single term if a dominant quantum sink exists in the system. In an XRII system, this is normally the case and the quantum sink is at the very first CsI layer. Under such a condition

$$\frac{1}{I} \approx \frac{1}{I_1} , \quad (3.7)$$

and the information factor is determined at the CsI layer.

Physical Parameters Affecting DQE

According to Equation 3.4, the DQE is determined by two factors: the x-ray quantum efficiency and the information factor resulting from the scintillation distribution. For an XRII, the quantum efficiency is determined by the CsI absorption α as well as by the x-ray transmission T_w through the vacuum window which is an integral part of the XRII,

$$\eta = T_w \alpha \quad (3.8)$$

$$= T_w \frac{(\mu/\rho)_{PE,\epsilon}}{(\mu/\rho)_{TOT,\epsilon}} \left\{ 1 - \exp\left[-\left(\frac{\mu}{\rho}\right)_{TOT,\epsilon} (\rho t) \right] \right\} .$$

for x-ray photons with energy ϵ . Here (ρt) is the density-thickness product and $(\mu/\rho)_{PE,\epsilon}$ and $(\mu/\rho)_{TOT,\epsilon}$ are the photoelectric and total mass attenuation coefficients of CsI, respectively.

The scintillation pulse height distribution is determined by three major factors. Among these are 1) the incident x-ray energy distribution (XED); 2) the absorbed energy distribution (AED); and 3) the optical pulse distribution (OPD). The influence of the first factor on the information factor will be discussed later since it is inherent to the incoming photon stream. The remaining two factors are due to various scintillation mechanisms and are dependent on the primary x-ray photon energy. When an x-ray photon with energy above the absorption edge of cesium or iodine is absorbed by photoelectric interaction, a characteristic x-ray may emit. The probability for such emission depends on the vacancy probability and the fluorescent yield of the corresponding electron shell. For CsI, the only significant fluorescences are due to the K-shells of Cs and I. Depending on the layer thickness, this characteristic x-ray will either be reabsorbed or will escape from the scintillating layer. As a result of the k-escape effect, only partial energy of the primary photon is deposited within the screen. Correspondingly, a "k-escape peak" appears in the absorbed energy distribution in addition to the "photo peak" which results from full photon energy deposition.

A physical model from Swank (1973) is shown in Figure 3.1 to indicate the details of x-ray interactions occurring in a CsI layer. This model forms the basis of the numerical analyses in this dissertation regarding the absorbed energy distribution and quantum efficiency. In the figure, one also notices fine structure in the distribution due to the escape of K_α and K_β x-rays from Cs and I. However, to the first order approximation, this structure can effectively be considered as a single line which is separated from the photo peak by an averaged K-fluorescent energy of ϵ_k . Let k_f denote the k-escape fraction, defined as the ratio of the number of escaped events n_k to that of total detected events n_a ,

$$k_f = \frac{n_k}{n_a} \quad (3.9)$$

The information factor $[I_{\text{AED}}(\epsilon)]$ due to the absorbed energy distribution for primary photon energy ϵ can be expressed as

$$I_{\text{AED}}(\epsilon) = \frac{[(1-k_f)\epsilon + k_f(\epsilon - \epsilon_k)]^2}{(1-k_f)\epsilon^2 + k_f(\epsilon - \epsilon_k)^2} \quad (3.10)$$

The k-escape fraction, k_f , which characterizes the AED, is a function sensitive to the CsI layer thickness. This thickness dependence will be explored experimentally in Chapters 4 and 5 to verify the validity of this physical model.

As a result of the deposited x-ray photon energy, a burst of optical photons is emitted with a statistical distribution (OPD).

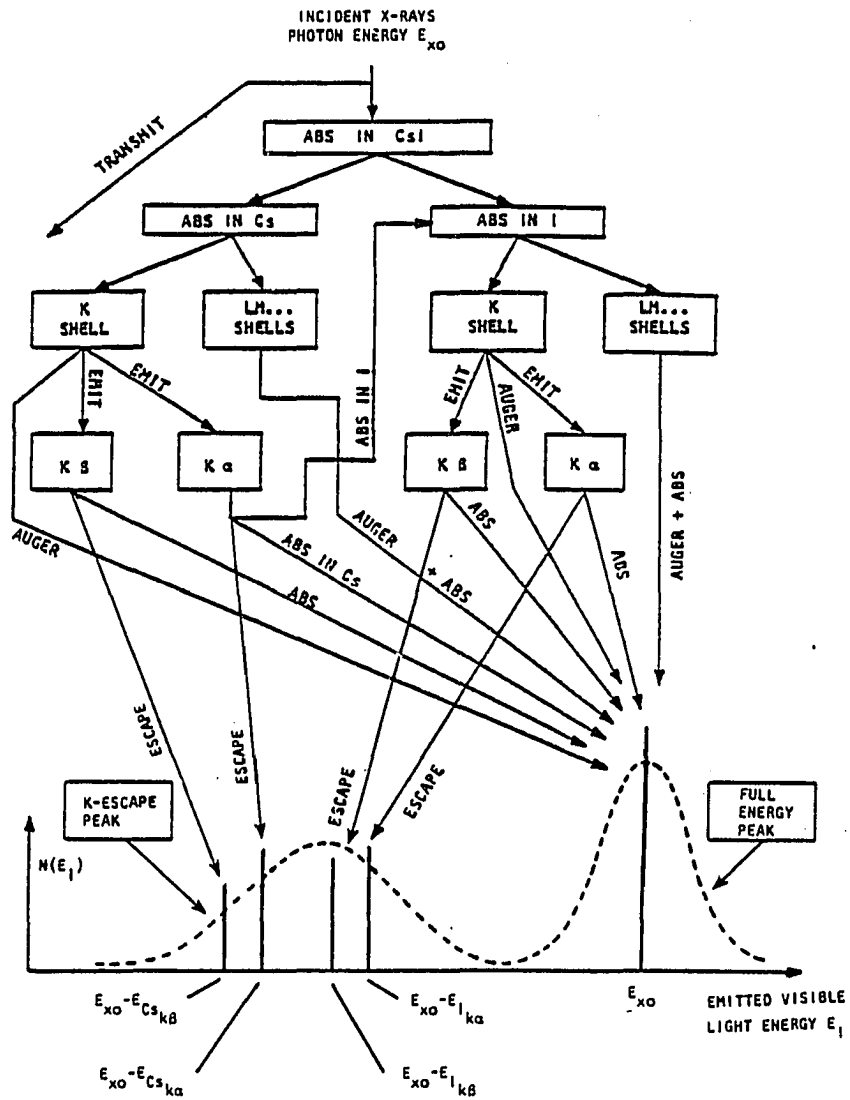


Fig. 3.1. X-ray interactions in the CsI layer.

(Modified from Swank, 1973)

This distribution modifies the line structures of AED to the final smoothed scintillation pulse height distribution (SPHD). Due to the complexity of its underlying physical processes, the OPD is left to be determined experimentally. For now, it is simply assumed that this OPD contribution to information factor (I_{OPD}) is a constant. With this simplification, the information factor resulting from the combined AED and OPD contribution is given by

$$I_{SCIN}(\epsilon) = I_{AED}(\epsilon) I_{OPD} \quad , \quad (3.11)$$

where I_{SCIN} is used to denote the information factor resulting from the scintillation pulse height distribution. As this factor characterizes the information degradation resulting from the scintillation process, a synonym, called "scintillation DQE" (DQE_{SCIN}) is commonly used. Henceforth, both terms will be used interchangeably.

Having discussed the scintillation process, one should determine the total information factor for a bremspectrum exposure, as it is always used in clinical procedures. Due to its inherent energy distribution, the incident x-ray photon stream affects the resultant pulse height distribution in a complicated way. However, as derived in Appendix A, the total information factor can be cascaded as

$$I = I_{XED} \bar{I}_{SCIN} \quad , \quad (3.12)$$

if proper interpretations are given to its components. Here \bar{I}_{SCIN} is the scintillation factor averaged over a modified x-ray spectrum as prescribed by Equation A.9, while I_{XED} is the information factor inherent to the absorbed x-ray spectrum as defined in Equation A.10. As a result, the system information transfer efficiency DQE is given by

$$\begin{aligned} \text{DQE} &= \bar{\eta} I \\ &= \bar{\eta} I_{\text{XED}} \bar{I}_{\text{SCIN}} \end{aligned} \quad (3.13)$$

where $\bar{\eta}$ is the mean quantum efficiency over the incident x-ray spectrum.

Imaging Properties

For an imaging system, the most critical performance characteristic is the image DQE as a function of spatial frequency. The image signal transfer is determined by the system MTF and the noise transfer by the system NPS. In this section, an analytical expression of NPS will be derived to investigate the interplay between the signal and noise propagations through a complicated system.

Image Signal Transfer

As a universal property of any direct-view intensifying imaging device, a signal-induced background is presented at the output image due to a variety of scattering processes. These processes force image carrying quanta to deviate from their paths described by the

respective imaging optics. As a result, the point spread function, PSF, of the system can be separated into two components: one resulting from the micro-imaging effects and the other from those long range scattering processes, as illustrated in Figure 3.2. Let us denote the shapes of the micro-imaging and the background components by $P_i(r)$ and $P_b(r)$, respectively, both with normalized area. The system PSF can then be expressed as

$$P(r) = f_i P_i(r) + f_b P_b(r) , \quad (3.14)$$

with

$$f_i + f_b = 1 . \quad (3.15)$$

Here f_i and f_b are the energy fractions resulting in image formation and the long range background, respectively. The corresponding system MTF is given by

$$MTF(f) = f_i MTF_i(f) + f_b MTF_b(f) . \quad (3.16)$$

The effect of signal-induced background is reflected as an abrupt falloff at the low frequency range of the resultant system MTF. Beyond a certain low frequency, the system transfers fewer image details than if the signal-induced background is absent. Therefore, this background, on first glance, seems to have an equal amount of

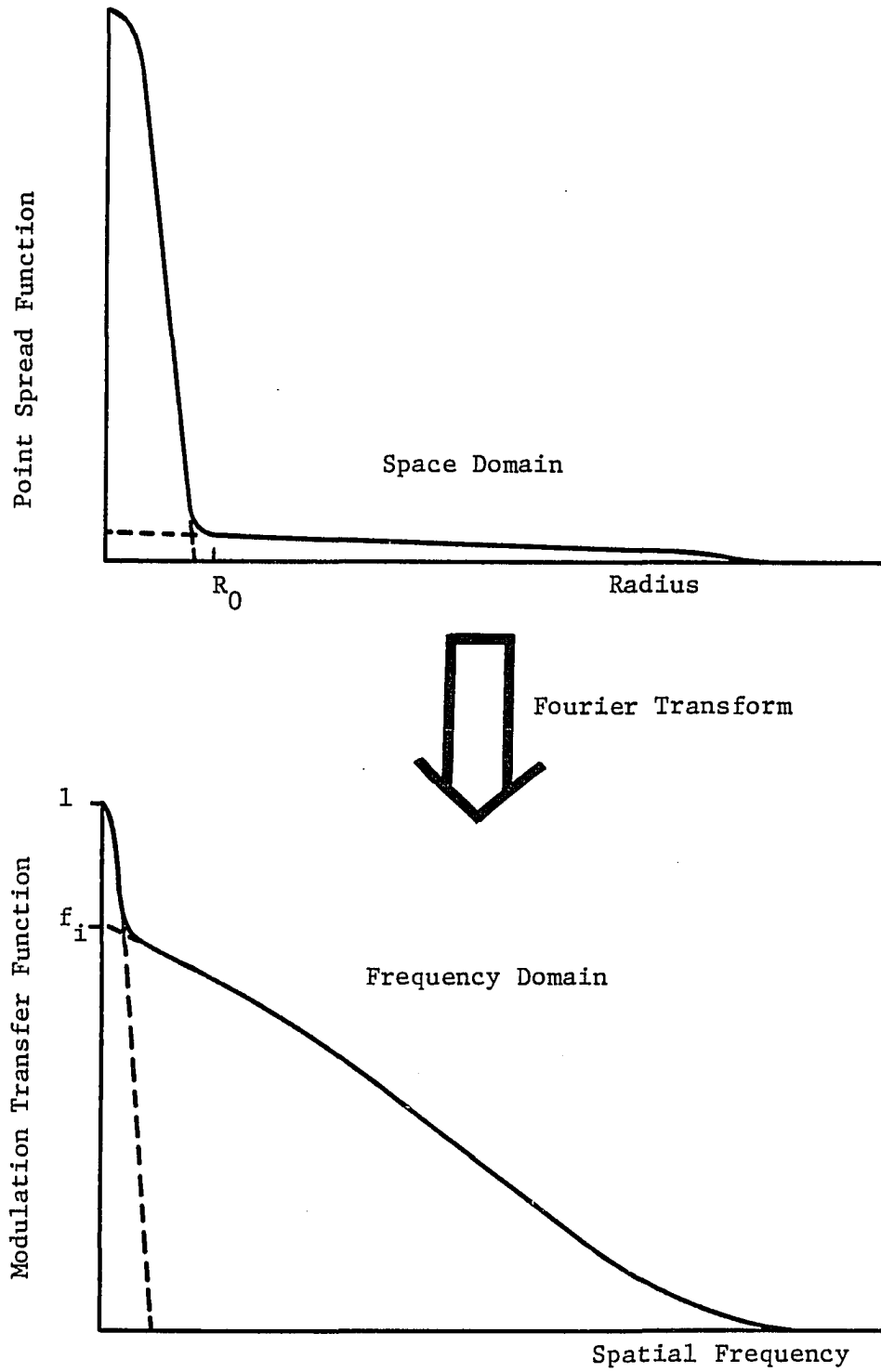


Fig. 3.2. Influence of signal-induced background on the MTF.

effect on the detective quantum efficiency (see Equation 2.7). However, as will be determined by the analysis of NPS below, its effect on the information transfer is much smaller than expected.

Image Noise Transfer

A cascaded intensifying imaging system transfers the image noise in a complicated way, as each system component has its own micro-imaging and statistical effect. However, for a linear system, the image noise property can be studied in an analytical form. With reference to Figure 1.2, the XRII system is identified with seven distinguishable stages with either a gain or a sink source to the quantum propagation. Under normal operating conditions, the overall system can be considered linear. Considering the information carriers as a series of impulses, such as x-ray photons, photoelectrons, or light photons, a general NPS expression for an n-stage linear imaging system is derived in Appendix B:

$$W_{\Delta z/z}(f) = \frac{1}{q} \left[\left(\frac{1}{I_1} - \frac{1}{\bar{m}_1} \right) |F_{1n}(f)|^2 + \frac{1}{\bar{m}_1} \left(\frac{1}{I_2} - \frac{1}{\bar{m}_2} \right) |F_{2n}(f)|^2 \right. \\ \left. + \dots + \frac{1}{\bar{m}_1 \dots \bar{m}_{n-1}} \left(\frac{1}{I_n} - \frac{1}{\bar{m}_n} \right) |F_{nn}(f)|^2 + \frac{1}{\bar{m}_1 \dots \bar{m}_n} \right], \quad (3.17)$$

where

q is the mean primary photon fluence absorbed,

\bar{m}_i is the mean gain of i -th stage,

I_i is the Swank's information factor due to i^{th} stage, and F_{in} is the MTF cascaded from the i^{th} stage throughout the remaining imaging chain.

Here the only provision is that the input primary photon stream is a Poisson random process.

At each stage, the noise power is inversely proportional to the mean number of quanta incident with additional fluctuation determined by the Swank's information factor. This componental noise spectrum has a frequency dependence following the MTF^2 as cascaded through the remaining system. The last term is simply the final recording noise where no further transfer is encountered and no further filtering is applied. In the case of a video pickup device, this white noise is the electron shot noise associated with the readout beam current. However, there are always electronic noise sources associated with the video circuit. This electronic circuit noise as a whole can independently be added to the final term and form the baseline recording noise in the image. If a photographic film is placed in the system as a recording medium, the final term can be thought of as film grain noise although the analysis above is not applicable to such a non-linear device. It is also interesting to note that the quantum threshold requirement which causes the non-linear response for a film may have a coupling effect on the independent statistical packages when they are recorded as bursts of film grains. This coupling effect may sharpen the appearance of the recorded quantum mottle originating from independent x-ray events. As a result,

the NPS may show a broader spectrum compared with that recorded by a linear system such as in the case of video camera tubes. Nevertheless, the system under study in this dissertation is linear and the mathematical analysis developed thus far can readily be adapted to the evaluation of the information efficiency.

Among the various possible statistical processes in the system, two special cases are worth noting. For Poisson and binomial statistics, the information factors are given as

$$I = \begin{cases} \frac{m}{1+m}, & \text{Poisson} \\ m, & \text{binomial} \end{cases} \quad (3.18)$$

Consequently, their corresponding statistical factors in the NPS expression are

$$\frac{1}{I} - \frac{1}{m} = \begin{cases} 1, & \text{Poisson} \\ 0, & \text{binomial} \end{cases} \quad (3.19)$$

The fact that the noise component resulting from a binomial process vanishes greatly simplifies the analysis on NPS. However, this does not imply that a binomial process does not introduce noise to a system. Its effect is to reduce the number of quanta impinging on the following stages and enhances the random fluctuations thereafter.

After identifying binomial processes in the system (see Figure 1.2), there remains only three noise components, namely, of the input CsI layer, the output phosphor, and the recording medium. The NPS of the system can then be expressed as

$$W_{\Delta q/q}(f) = \frac{1}{q} \left[\left(\frac{1}{I_1} - \frac{1}{\bar{m}_1} \right) |F_{1n}(f)|^2 + \frac{1}{\bar{m}_1 \bar{m}_2 \bar{m}_3} \left(\frac{1}{I_4} - \frac{1}{\bar{m}_4} \right) |F_{4m}(f)|^2 + \frac{1}{\bar{m}_1 \bar{m}_2 \dots \bar{m}_n} \right], \quad (3.20)$$

with $n=7$.

The first two noise terms in this equation originate from stages with gains both on the order of 2000. Since the information factor cannot exceed unity, the statistical factors can be approximated as

$$\frac{1}{I_i} - \frac{1}{\bar{m}_i} \approx \frac{1}{I_i}, \quad i=1, 4. \quad (3.21)$$

Therefore, the NPS expression is further simplified to

$$W_{\Delta q/q}(f) = \frac{1}{q} \left[\frac{1}{I_1} |F_{1n}(f)|^2 + \frac{1}{\bar{m}_1 \bar{m}_2 \bar{m}_3 I_4} |F_{4n}(f)|^2 + \frac{1}{\bar{m}_1 \dots \bar{m}_n} \right]. \quad (3.22)$$

These are the three NPS components in an XRII system, as will be observed in Chapter 5.

It should be pointed out that this mathematical analysis applies only to a linear system with each system component having a "thin" quantum conversion layer. This notion is related to an analysis made by Lubberts (1968). If a quantum conversion layer provides different MTF from each sublayer, its NPS component will not follow the combined layer MTF^2 . However, in most modern x-ray image intensifiers, the CsI scintillators are prepared with special

techniques that result in a needle-like structure. Therefore, it is a good approximation to assume that each sublayer contributes identical blurring to the final image. Under this assumption, the CsI NPS component in Equation 3.22, which is of primary importance, is a valid expression.

Effect of Signal-Induced Background on DQE

It was pointed out that the signal-induced background degrades the image signal transfer. In this subsection, its effect on noise transfer is analyzed. As was discussed, any noise source originating from a particular stage undergoes an equal amount of filtering just as does the signal throughout the remaining imaging chain. A practical exercise frequently used in the measurement of the NPS of a screen-film combination is to introduce an air gap between these two components to isolate the film grain noise from the primary x-ray quantum mottle. In this practice, the quantum noise originating from the input screen is filtered out by the air gap which is located behind the noise source. Therefore, one can conclude that any induced background introduced behind the noise source will have an equal effect on noise and signal reduction. In other words, this particular induced background has no effect on information reduction caused by all the noise sources which originated before it. Figure 3.3 shows all the possible sources of XRII contrast reduction. As analyzed by Vosburgh et al. (1977), the dominant component is the output phosphor where light photons diffuse laterally along the interface between the phosphor and its substrate. For a system which is x-ray photon noise limited,

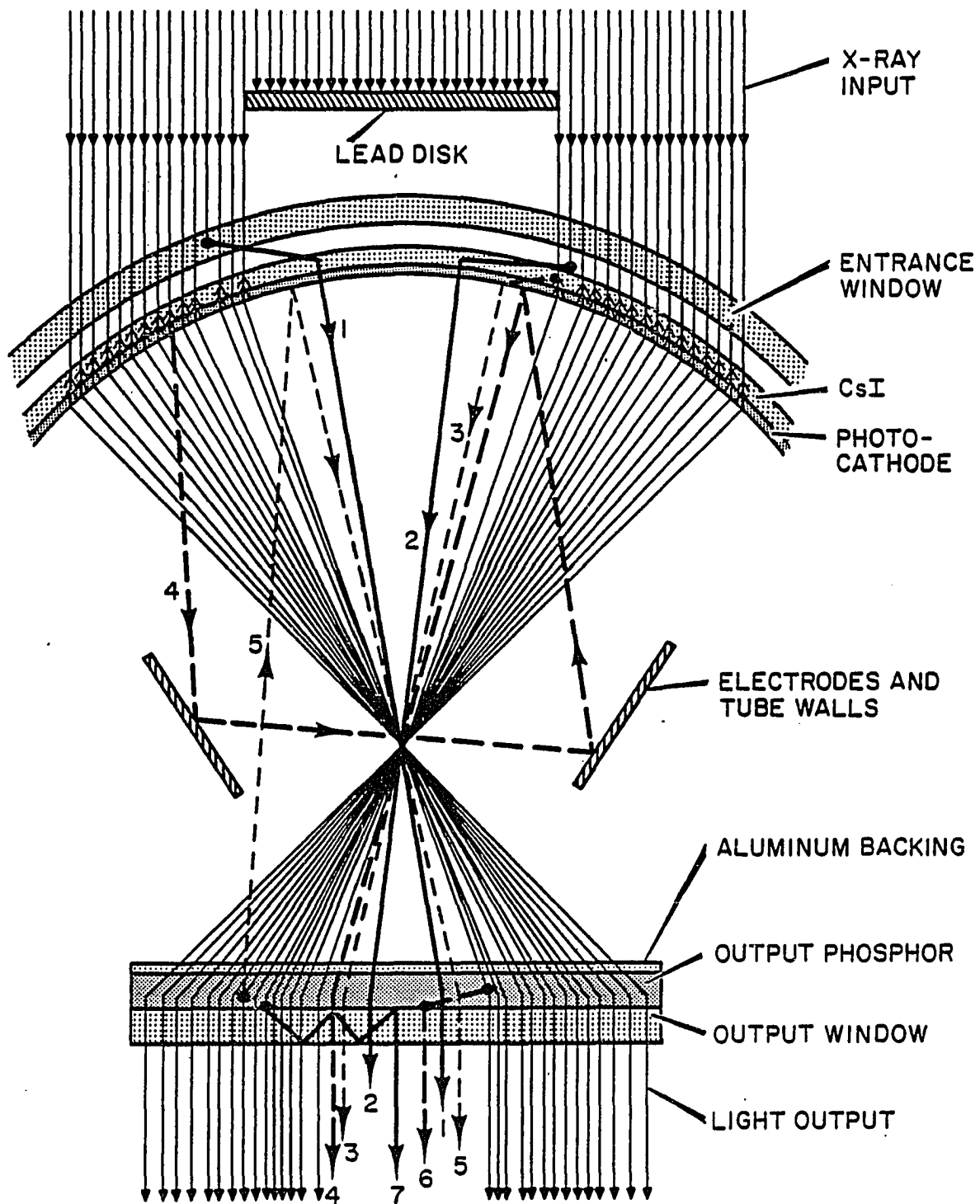


Fig. 3.3. Sources of signal-induced background in an XRII.

only the x-ray scattering occurring prior to x-ray absorption contributes to the information degradation. As will be determined in Chapter 5, its effect is practically negligible.

CHAPTER 4

EXPERIMENTAL METHODS

In this chapter experimental methods will be developed for measuring the information-related characteristics of the system. As discussed in Chapter 3, non-imaging properties such as quantum efficiency, scintillation DQE, and k-escape fraction are functions of two independent parameters: x-ray photon energy and sensor thickness. Experimental studies on those properties are described in the first section. Measurements on the imaging properties, such as signal-induced background, MTF, and NPS follow. Experimental results and their implications on the inherent information efficiency will be discussed in Chapter 5.

Non-imaging Properties

CsI Sensor Thickness

Five CsI x-ray image intensifiers with different layer thicknesses were used to study the thickness dependence of non-imaging properties. Layer thickness was measured non-destructively by the transmitted bremspectrum through an XRII as shown in Figure 4.1. With sufficiently narrow beam geometry, one can observe the absorption edges of Cs and I and calculate the "thickness" from the discontinuities of the spectrum. Let the spectral intensities just above and below an absorption edge be denoted by I_+ and I_- . The

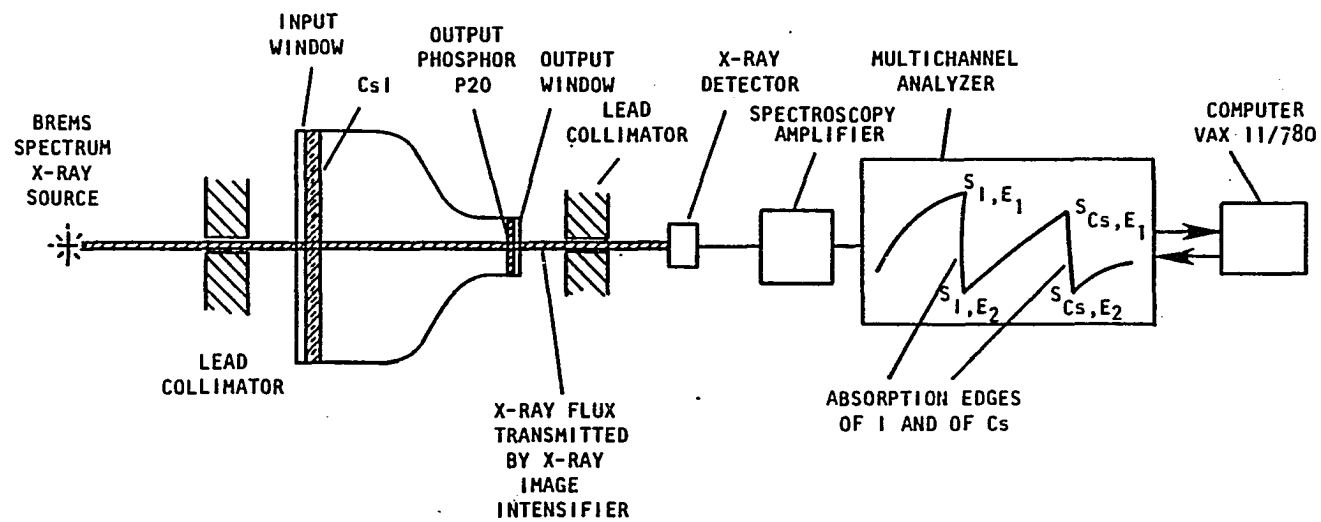


Fig. 4.1. Experimental setup for CsI layer thickness measurement.

density-thickness product due to one particular material in the scintillating layer can be found by

$$\rho t = \frac{\ln\left(\frac{I_-}{I_+}\right)}{\Delta(\mu/\rho)} \quad , \quad (4.1)$$

where $\Delta(\mu/\rho)$ is the discontinuity in mass attenuation coefficient at the edge. Having identified the absorption edges of Cs and I this way, the CsI layer density-thickness product can be calculated by

$$(\rho t)_{\text{CsI}} = (\rho t)_{\text{Cs}} + (\rho t)_{\text{I}} \quad . \quad (4.2)$$

Accuracy was tested by performing this measurement on an experimental x-ray image intensifier made specifically for this purpose by Siemens. This intensifier has a CsI thickness of 0.035 g/cm^2 and a mean value of 0.0361 g/cm^2 was found as averaged over three trials with a standard deviation of 0.0015 g/cm^2 . The corresponding error was about 4%. In addition to this test, measurements on materials like dysprosium, ytterbium, and tungsten with known thicknesses showed a similar accuracy. Of crucial importance for the accuracy of this method is that the x-ray beam geometry be sufficiently narrow so that scatter can be avoided. An x-ray beam diameter of 2 mm or less has proven to be sufficient.

Pulse Height Distributions

Roehrig et al. (1979) used a fast counting technique to measure the scintillation DQEs of an XRII and an x-ray screen. In the present study, a more conventional analog integration method was adopted to measure the pulse height distributions. The advantage of such an approach is that the information-related properties of quantum efficiency and scintillation DQE can be measured by the same technique. At this point, one should distinguish two types of pulse height distributions. A scintillation pulse height distribution (SPHD) is obtained by integrating all the scintillation pulses resulting from each and every detected x-ray photon. On the other hand, a multiple pulse height distribution (MPHD) is obtained by integrating all the scintillation pulses emitted within a certain observation time without prior knowledge of the number of x-ray photons to be detected. From the SPHD, the scintillation DQE and k-escape fraction can be calculated by Equations 3.5 and 3.9, respectively. The quantum efficiency can be derived from the combination of the two distributions provided the incident photon flux rate is known. Let us consider an MPHD with mean μ_m and variance σ_m^2 resulting from repetitive integration of the light pulses emitted within an integration time τ . The mean number of absorbed x-ray photons in τ is given simply by

$$n_a = \frac{\mu_m}{\mu_s} , \quad (4.3)$$

where μ_s is the mean value in the corresponding SPHD. By a parallel approach, this mean absorbed number can be obtained by considering Equations 2.1 and 3.4,

$$\text{DQE} = \frac{(S/N)_{\text{out}}^2}{(S/N)_{\text{in}}^2} = \frac{\mu_m^2}{\sigma_m^2 n_o} \quad (4.4)$$

$$= \eta \text{DQE}_{\text{SCIN}} .$$

By identifying ηn_o as n_a we have

$$n_a = \frac{\mu_m^2}{\sigma_m^2 \text{DQE}_{\text{SCIN}}} . \quad (4.5)$$

The interesting implication from Equations 4.3 and 4.5 is that the accuracy of the pulse height measurements can be self-tested. At this point, we claim that this self-consistency is within an error of 2% for all the measurements done by this method. By knowing the incident flux rate ϕ_o , the quantum efficiency is calculated according to

$$\eta = \frac{n_a}{\phi_o \tau} . \quad (4.6)$$

The experimental setup for pulse height distributions is shown in Figure 4.2. Major components in this setup are the x-ray source, PMT adaptor, and analog integrator. They are described separately in the following subsections.

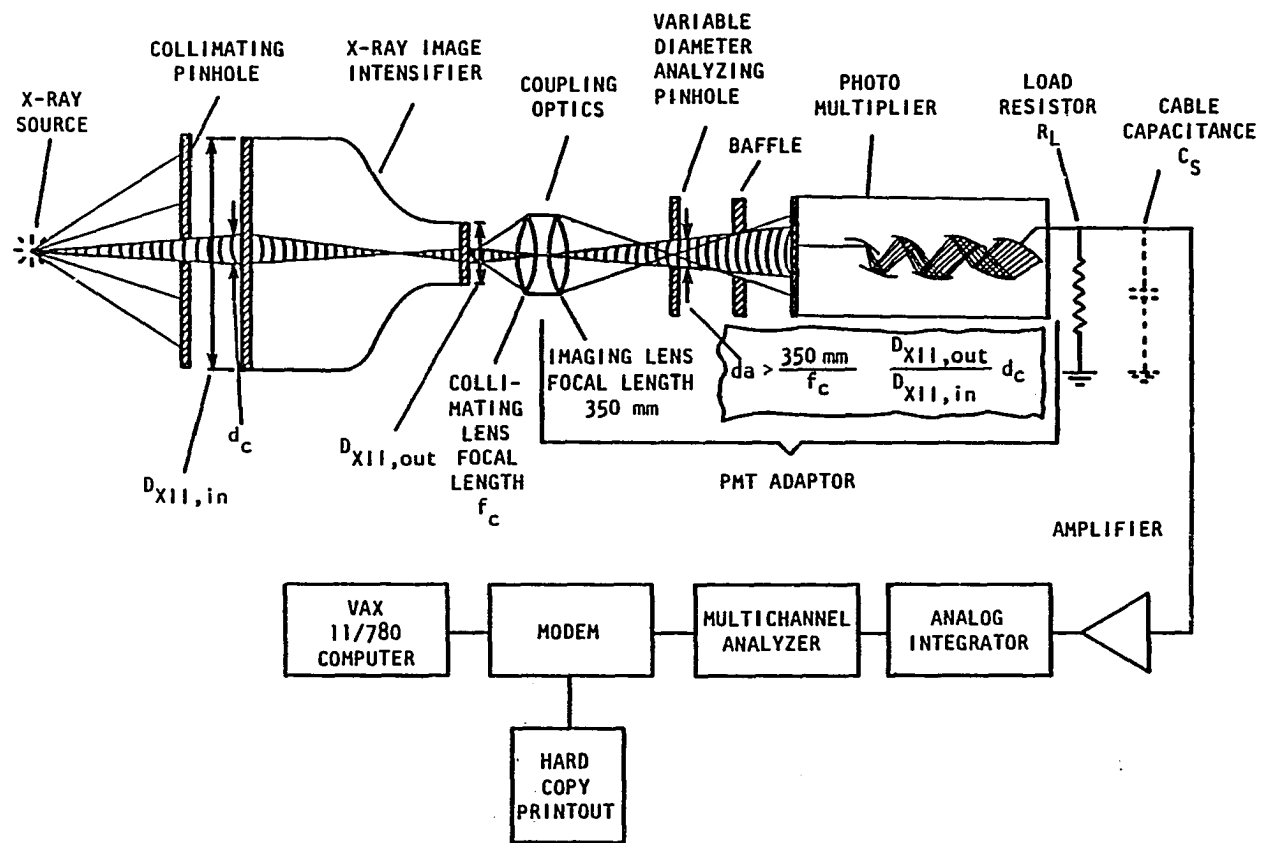


Fig. 4.2. Schematic of pulse height distribution measurements.

X-Ray Source and Calibration

The x-ray source used was a variable energy source marketed by Amersham Searles as Model AMC.2084 with some modifications. It utilizes Am 241 with a half-life of 470 years to excite the K-fluorescence of six switch-selectable materials: thulium, terbium, cerium, barium, silver, and molybdenum. The quasi-monoenergetic spectra resulting from the first five materials were used to study the energy dependence of the non-imaging properties. Their spectral flux contents, as shown in Table 4.1, were calibrated with a hyperpure germanium x-ray spectrometer which has an efficiency of practically 100% for all energies concerned. The source was attached to a collimator/holder with an exit aperture of 2 mm diameter as shown in Figure 4.3. This assembly was used during all measurements and calibrations.

PMT Adaptor

The PMT adaptor was designed specifically for in situ evaluation of XRIIs in their clinical environment. Most XRIIs in clinical use have their controls as an integral part of the x-ray generator's control panel. In addition, the intensifiers are built into a housing that carries the adjusted and focused collimating lens. This lens is usually difficult to remove. Therefore, the PMT adaptor was designed to be installed in place of the system's TV camera or cine camera. It has an imaging lens with a focal length of $f = 350$ mm, a variable field aperture located at the focal plane of the imaging lens, a baffle, and a photomultiplier. When coupled to an XRII through its collimating lens, the adaptor permits measurement of the light

Table 4.1. X-Ray Source Lines and Associated Flux Levels (Collimator diameter: 2mm).

Fluorescent Element	Source flux ϕ (x-ray photons/s)	k-X-Ray Lines (keV)/flux (x-photons/s)				Background	
		$k\alpha_2$	$k\alpha_1$	$k\beta_1$	$k\beta_2$	A	B
Tm	74.7	49.88/ 21.34	50.74/ 36.02	57.5/ 12.95	49/ 4.37	---	---
Tb	69.2	43.74/ 18.38	44.48/ 34.67	50.4/ 12.46	51.7/ 3.36	---	59.49/ 0.34
Ce	34.8	34.28/ 9.1	34.72/ 17.5	39.2/ 5.68	40.2/ 1.67	49.19/ 0.48	59.49/ 0.45
Ba	46.3	31.82/ 11.56	32.19/ 22.23	36.4/ 7.52	37.3/ 1.88	49.19/ 2.62	59.49/ 0.50
Ag	30.7	21.99/ 7.55	22.19/ 14.81	24.9/ ----5.94*----	25.5/ 	49.19/ 1.51	59.49/ 0.88

* $k\beta_1$ and $k\beta_2$ could not be resolved separately

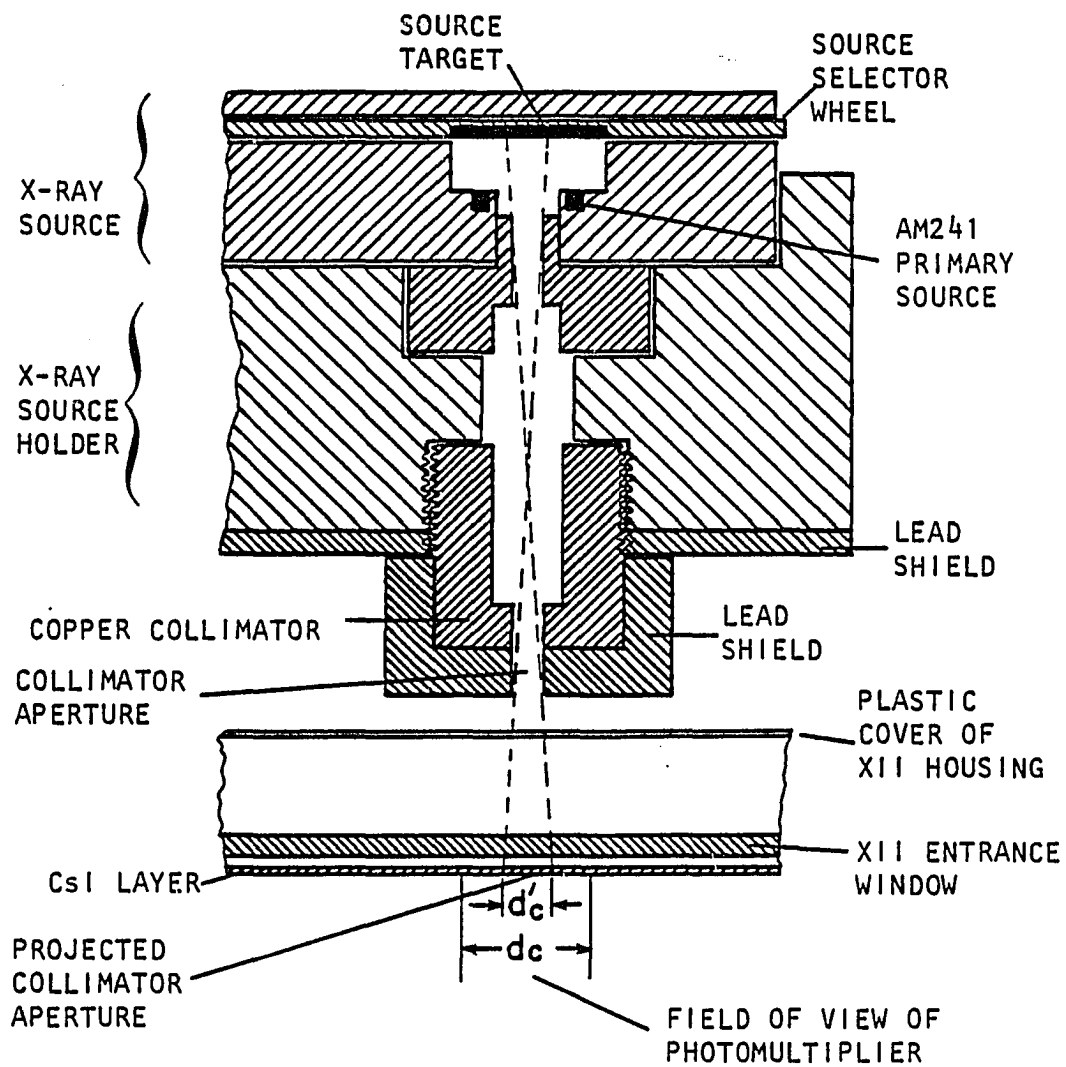


Fig. 4.3. X-ray source, holder, and collimator.

outputs from a small area to eliminate the dark background. The variable field aperture was adjusted to be slightly larger than the collimating pinhole of the x-ray source as projected onto the x-ray sensing layer. This adjustment was verified by a much slower change in PMT current during aperture adjustment.

Analog Integrator

The schematics of the analog integrator are shown in Figures 4.4 and 4.5. Basically, it is a voltage sensitive integrator that performs integration on the voltage drop provided by the load resistor in the PMT's anode circuit. The integrator features internal and external trigger functions and pileup rejection. Its integration time ranges from 30 μ s to 100 ms, or it can be controlled by an external gate signal. The internal trigger mode is used for the scintillation pulse height measurement. In this mode of operation, the integration is synchronized with a detected x-ray event by a variable threshold. A successful integration is concluded by sending out a short command pulse to the multichannel analyzer (MCA) which then samples the integrated value. However, if pileup occurs during the integration period, the integration process terminates immediately without sending out such a command pulse. At this time it is ready for the next event. The integration time is typically set to 10 ms to account for the decay time of the intensifier's output phosphor. For multiple pulse height measurement, the integrator is operated on external trigger mode with a predetermined integration time. In this case, the integrator performs simple integration under the

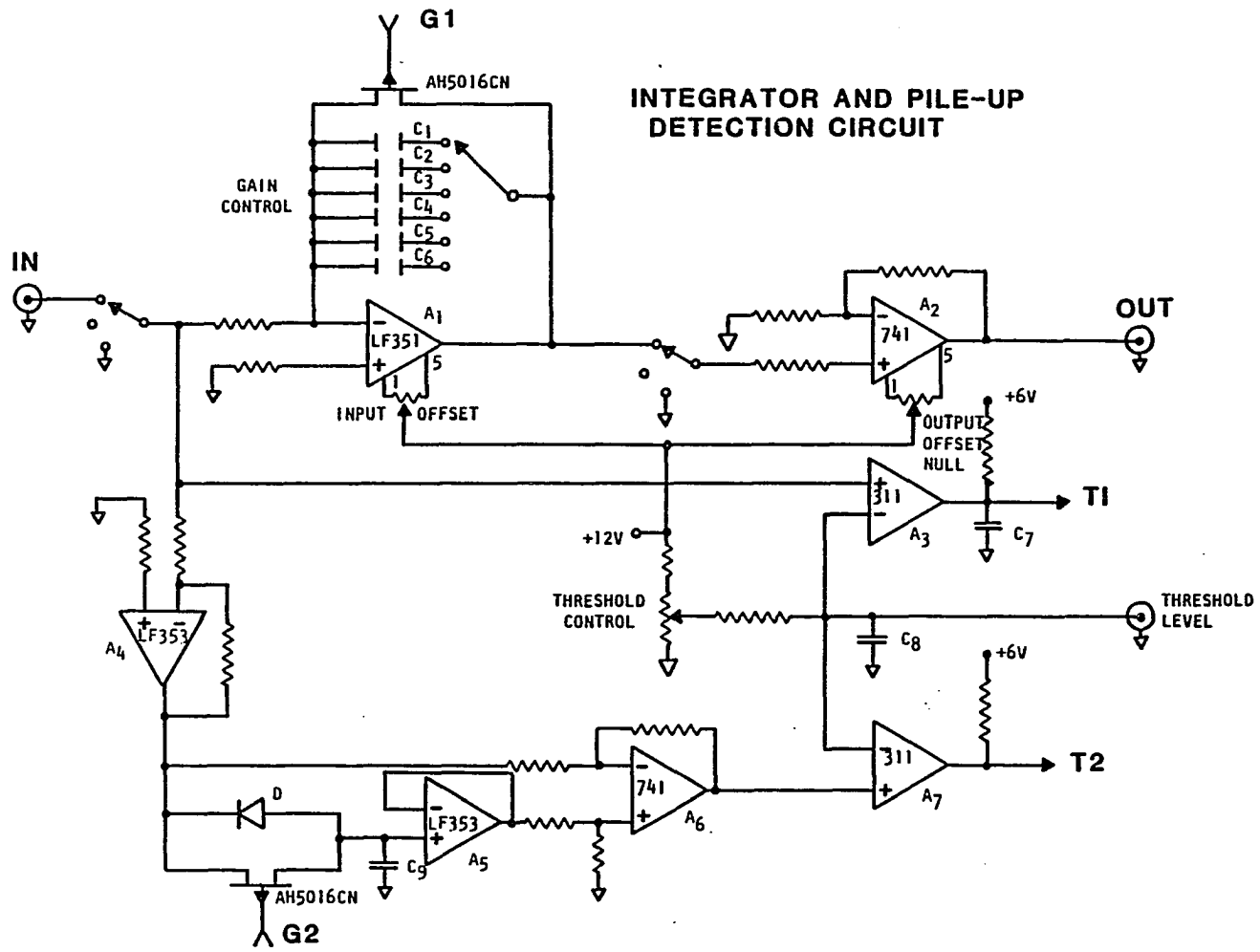


Fig. 4.4 Integrator and pile-up detection circuit.

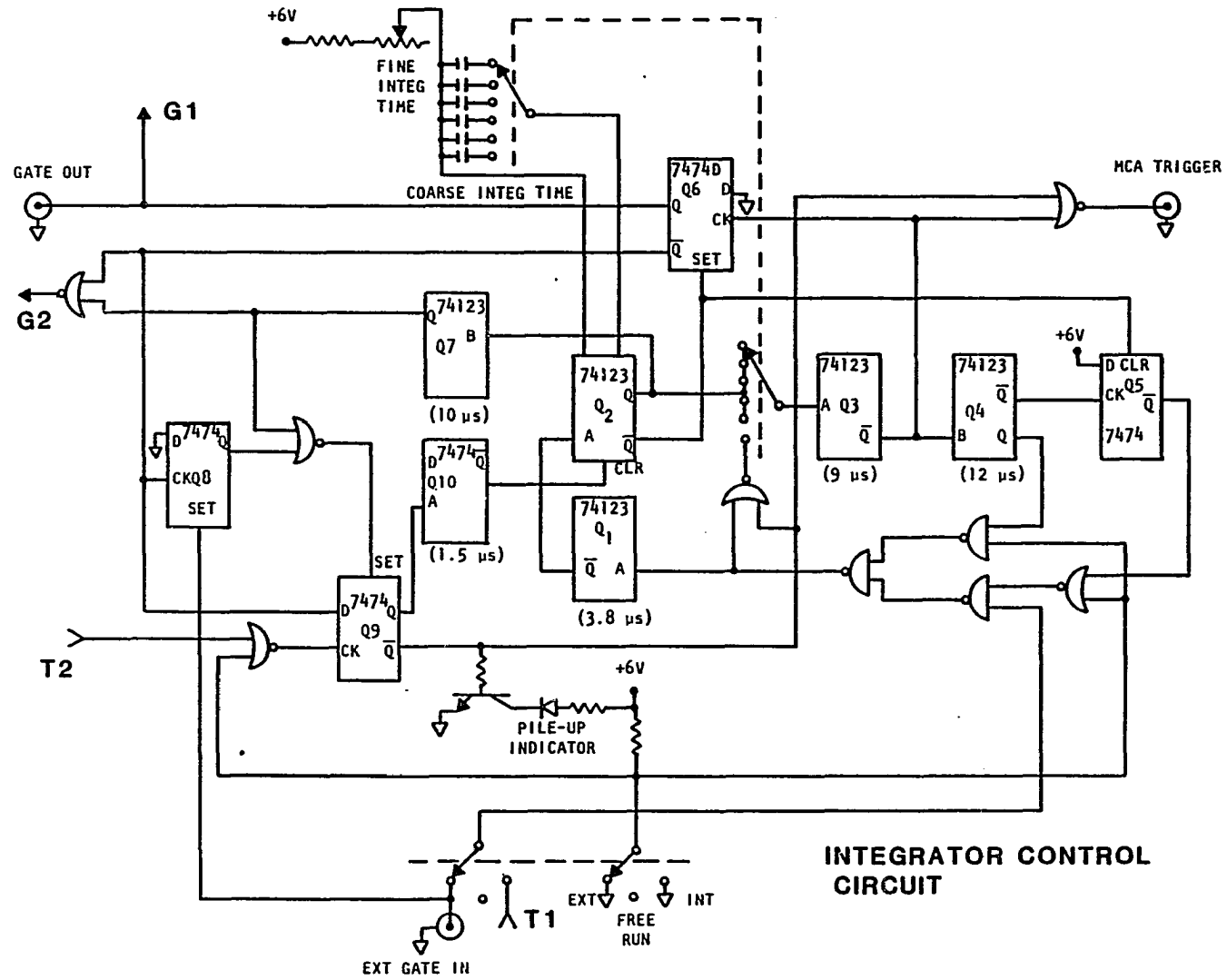


Fig. 4.5. Integrator control circuit.

control of an external gating signal which is independent of the x-ray events. An MCA command pulse is always generated at the end of integration and the pileup circuit is automatically disabled. Typical integration times used for the MPHD range from 100 ms to 400 ms, depending upon the x-ray sources used.

Imaging Properties

Signal-Induced Background

As discussed in Chapter 3, the PSF of the imaging system can be separated into two components with their energy fractions denoted by f_i and f_b . It is the energy fraction f_b that is taken out of the signal by the signal-induced background. Referring to Figure 3.2, there exists a range R_0 , beyond which the system PSF is dominated by the background. Following the method introduced by Stahnke and Heinrich (1966), this background energy fraction f_b can be measured with the help of a set of lead discs.

Consider an XRII which is exposed uniformly within its useful diameter. The brightness B_0 at the center of the intensifier output is given by

$$B_0 = \int_0^{\infty} \phi_0 c P(r) dr = \phi_0 c \quad (4.7)$$

where ϕ_0 is the uniform x-ray exposure rate, and c is the exposure-to-brightness conversion factor.

By placing at the XRII input a lead disc with radius R which is greater than R_0 , the corresponding center brightness $B(R)$ is given by

$$\begin{aligned} B(R) &= \int_R^{\infty} \phi_0 c P(r) dr \\ &= \int_R^{\infty} \phi_0 c f_b P_b(r) dr \quad , \end{aligned} \quad (4.8)$$

since the PSF is dominated by the background.

By using a series of lead discs with different diameters, all larger than $2R_0$, an extrapolated value at vanishingly small diameter can be obtained,

$$\begin{aligned} B(0) &= \int_0^{\infty} \phi_0 c f_b P_b(r) dr \\ &= \phi_0 c f_b \quad . \end{aligned} \quad (4.9)$$

The energy fraction due to signal-induced background can be obtained by

$$f_b = \frac{B(0)}{B_0} \quad . \quad (4.10)$$

A commonly used index for signal-induced background is the "contrast factor." This parameter is usually defined as

$$C = \frac{B_0}{B(R)} \quad (4.11)$$

with the lead disc radius, R , selected to be 10% of the useful XRII area. Therefore, this method is simply an extension of normal practice for the measurement of the contrast factor.

The experimental setup for contrast measurement is shown in Figure 4.6. A lead diaphragm of the specified useful XRII input diameter was placed in front of the intensifier to eliminate the stray scattering outside the useful field. A Gamma Scientific photometric lens with variable aperture was used to provide an optical magnification of 2.5. With an image aperture diameter of $50\mu\text{m}$, the total brightness within a $20\mu\text{m}$ diameter was measured by the PMT. The lens mounting tube was carefully baffled to eliminate optical veiling glare introduced by the measuring device. With this setup, a contrast factor greater than 2000 was achieved when the measuring device viewed a 1 mm diameter black spot surrounded by a 25 mm diameter luminating area. This amount of veiling glare was negligible as compared to the contrast factor provided by the XRII. The diameter of the lead discs used ranged from 4 to 117 mm with a 2 mm step below 20 mm. From prior experience on the resolution test of this particular intensifier, the 4 mm diameter was sufficient to cover the short range PSF in any of the three XRII magnification modes.

General Experimental Conditions

In Equation 2.7 the $\text{DQE}(f)$ is derived from two imaging properties, the MTF and the NPS. Meaningful results can be obtained only if both quantities are measured under the same or nearly the same conditions. In addition, precautions must be exercised for

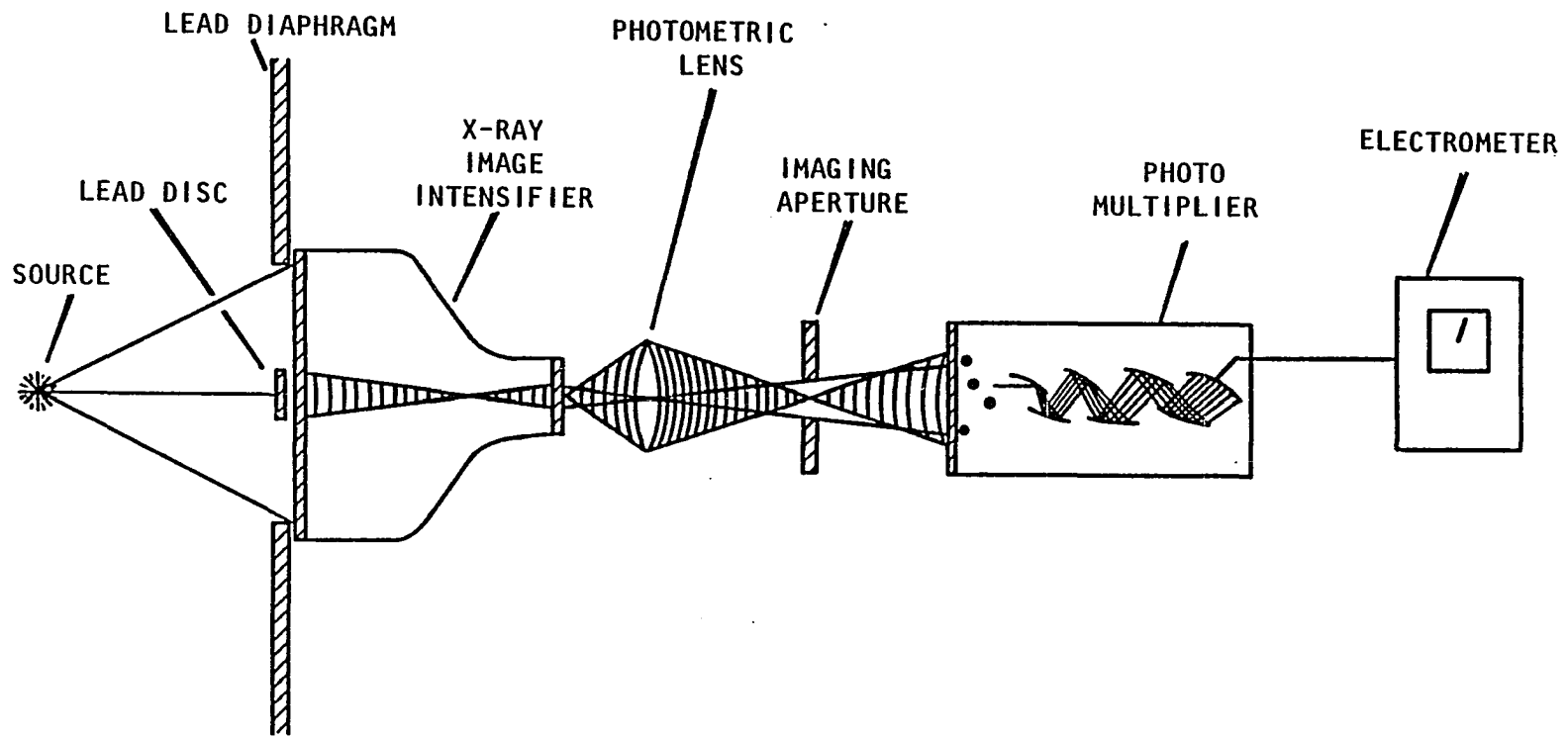


Fig. 4.6. Schematic of contrast factor measurement.

the absolute measurement of NPS. It is therefore necessary to discuss some general considerations before the experimental methods are described.

The experimental system in Figure 1.2 was used for both the MTF and the NPS measurements. By the same reasoning discussed earlier, a lead diaphragm was used to limit the x-ray flux to a useful input diameter. For each pair of measurement, the NPS was done immediately after the MTF data were taken without changing any experimental condition.

Since the NPS is an absolute quantity, it should be measured with great caution, especially when a video camera tube is used as the image pick-up device. A phenomenon commonly known as "lag" exists in all video tubes due to the electrostatic properties of the electron beam. Simply speaking, the lag is the inability to read out all the charges stored on the target during one raster scan. As a result, the charges read out in one scan consist of information recorded during previous exposure frames. This correlation among exposures is certainly not desirable for a meaningful NPS measurement. Therefore, a microprocessor-based camera control system was developed which modified the normal camera operation in a totally programmable fashion. This flexibility enabled us to make a series of uncorrelated images from independent exposures. Figure 4.7a shows the timing relationship among the x-ray exposure, the electron beam, and the image recording for a typical NPS run. The exposure was synchronized to the camera operation with a fixed exposure time of 20 ms. Immediately prior to exposure, the electron beam was shut off (blanked) for one

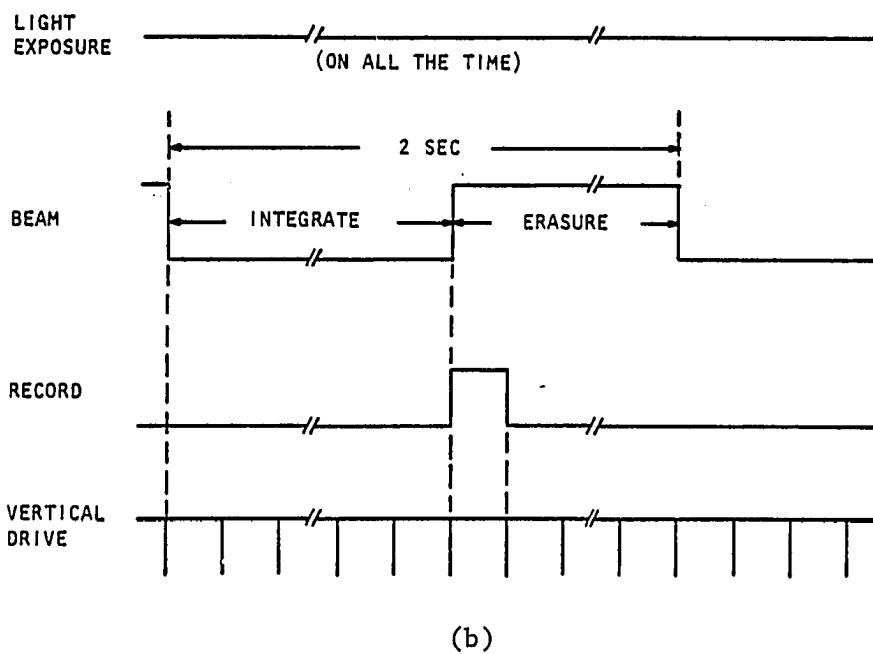
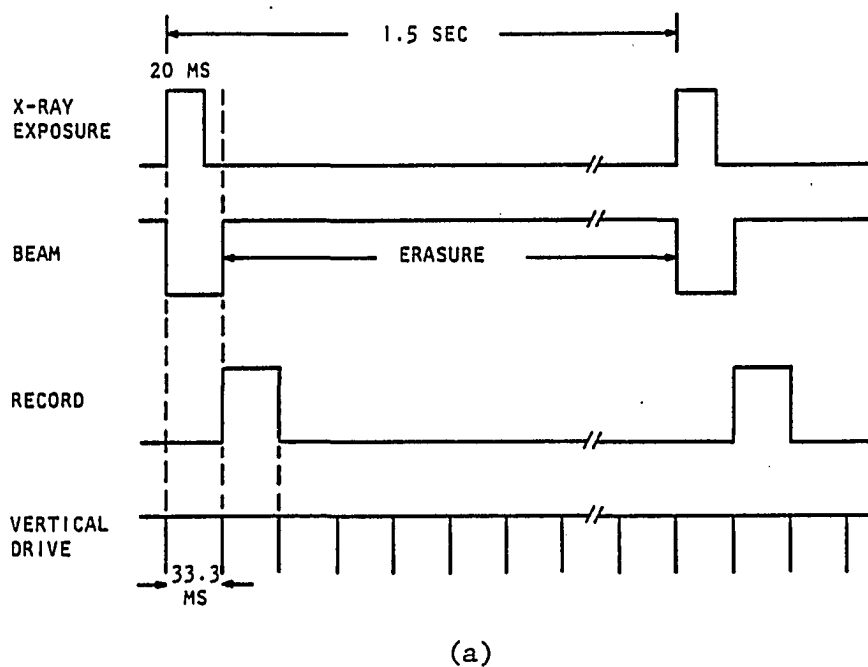


Fig. 4.7. Timing diagram for exposure and camera operation.

- (a) X-ray exposure
- (b) Light exposure

33.3 ms frame to perform charge integration. The extra 13.3 ms takes care of the XRII phosphor decay so that the delayed light photon emissions are collected. Within the next frame, the charge pattern was read out with a sequential (non-interlaced) scan, and recorded by the digital memory. During the remainder of the cycle, the electron beam is constantly reading to erase the residual charges. With a cycle time of 1.5 seconds, 43 erasure scans were used. This scheme ensured that recorded noise images were independent of each other, although readout efficiency was sacrificed.

Compared with screen-film, the PEID system is a rather flexible imaging chain. There are several variables, such as XRII magnification, lens aperture, video gain, and even the black level, that can be selected for a particular application. While each system parameter affects the system performance to some extent, it is practically impossible to evaluate them all in a single study. Since the XRII is of primary importance, the remaining components will be treated as a single unit with fixed parameters during this study.

The tandem configuration was composed of a 100 mm f/1.5 collimating lens and a 400 mm f/6 imaging lens, both operating at their maximum speeds in order to isolate the three NPS components. The 400 mm/100 mm focal ratio was chosen simply because of the limited 512x512 digital store format. The raster was adjusted to a 16 mm square and the video gain was set to deliver 800 mV for a signal current of 150 nA. For all the measurements, the exposure was adjusted so that a level of 800 mV was recorded. X-ray exposure was monitored

during the experiment by a dosimeter. The pedestal level was fixed to 40 mV and corrected in the data analysis.

The imaging properties were investigated with three different x-ray spectra, 50 kVp, 80 kVp, and 90 kVp with 0.25 mm Cu filtration in two XRII magnification modes, 4" and 9", under the above general conditions. In addition to these, three special measurements were performed to provide supplementary information to the general analysis. We will describe them briefly together with the special conditions involved.

Special Experimental Conditions

The system behavior under high flux was studied using 20 times the normal exposure rate. In this study, the optical collection efficiency was reduced correspondingly by stopping down the lens together with a neutral density filter inserted in the optical path. Exposure time and the other parameters were left unchanged.

According to Equation 3.21, the system NPS is composed of three components. In order to eliminate the NPS component resulting from the scintillation layer, the XRII was excited by a fluorescent lamp. This was possible after removal of the normally non-transparent cover of the XRII housing. Due to the inefficient transmission of light photons through the XRII window, the output screen provided a relatively low brightness. Consequently, a long integration time was needed for the camera tube to reach the required signal current. This integration was done by programming the camera controller into an internal frame integration mode without involving a mechanical

shutter. Figure 4.7b shows the timing diagram. During a preparation period, a negligible amount of signal current is constantly read out due to the constant low illumination. The camera is then blanked for charge integration for a 30-frame interval (1 second) which results in the required 800 mV signal level. The beam is then turned on to read out the integrated signal and the preparation period starts. This cycle is repeated every 2 seconds. By this scheme, there is no correlation among the recorded noise images. However, there is a small amount of residual signal in each recorded frame due to the constant low illumination just before the integration. Compared with the 30-frame integration interval, these residual charges can actually be neglected.

The last NPS component due to the camera tube itself was obtained by exposing the camera tube directly with a defocused uniform light source. An interference filter at 550 nm was inserted in the light path to reduce the illumination so that a comparable integration time can be used. The light intensity was reduced to a level such that a 12-frame integration was used with the same repetition rate.

Modulation Transfer Function

The MTF was measured with a set of x-ray patterns composed of a series of 50- μ m thick lead strips of 50% duty cycle. The sine wave modulation of the fundamental Fourier component was extracted from the recorded modulation profile. In order to improve the signal-to-noise ratio, profile data were obtained by summing the five center scan lines for ten repeated exposures. A cardboard pattern holder

was mounted directly on the XR11 input plane to permit easy change of the patterns. This holder was carefully aligned such that the edge deviated by only one pixel across the whole length of the recorded image.

The input modulation of the test patterns was calibrated against the XR11 by x-ray transmission measurement. A coarse pattern was placed in front of the XR11 to intercept a collimated x-ray beam of 2-mm diameter. The XR11 output brightness was then measured by the same arrangement as in Figure 4.6. An imaging aperture of 4 mm was used. By passing the x-ray beam through the clear and black areas of the pattern, the corresponding brightnesses B_o and B_b were measured. The input sine wave modulation is then given by

$$M_o = \frac{(B_o - B_b)}{\pi(B_o + B_b)} \quad , \quad (4.12)$$

where π converts the square wave modulation to sine wave modulation. By the assumption that all the x-ray patterns had equal thicknesses, the modulation transfers were obtained simply by the ratio of output modulations to this input modulation.

In order to isolate the MTF of the XR11, the MTF of the lens/camera combination must be determined. This was done by replacing the XR11 with an Ealing high resolution pattern mounted on a uniform light source. The input square wave modulation for this pattern was assumed to be 100%.

Algorithm of NPS Calculation

For each NPS measurement, 14 independent noise image frames made from uniform exposures were recorded. As the first step, each frame was shading-corrected by a low-pass-filtered reference image derived from the average of all 14 frames. Each corrected frame was then divided into six segments as shown in Figure 4.8. Within each segment, the lines were summed vertically for the slit synthesis in order to obtain a radial slice of the two-dimensional NPS. This gave an equivalent slit dimension of 1 x 128 pixels, or 87 μm x 11 mm at the object plane for 9" operation. At this point, six independent noise profiles were obtained for each frame, each 256 samples long. A first-order least-square fit was then applied to obtain a smoothed mean curve. The noise profile was then normalized, point by point, to its local mean for use in the calculation of the relative noise power spectrum, $W_{\Delta q}/q$.

For the sake of clarity, let us denote by the symbol w_{ki} , the relative noise profile of the k^{th} segment of the i^{th} frame. The next step was to subtract two noise profiles with the same segment index from two different frames,

$$w_{ki} - w_{kj}, \quad i \neq j. \quad (4.13)$$

This subtracted noise profile is then Fourier transformed, squared, and accumulated. This subtraction process was done for all segments on all permuted pairs of frames,

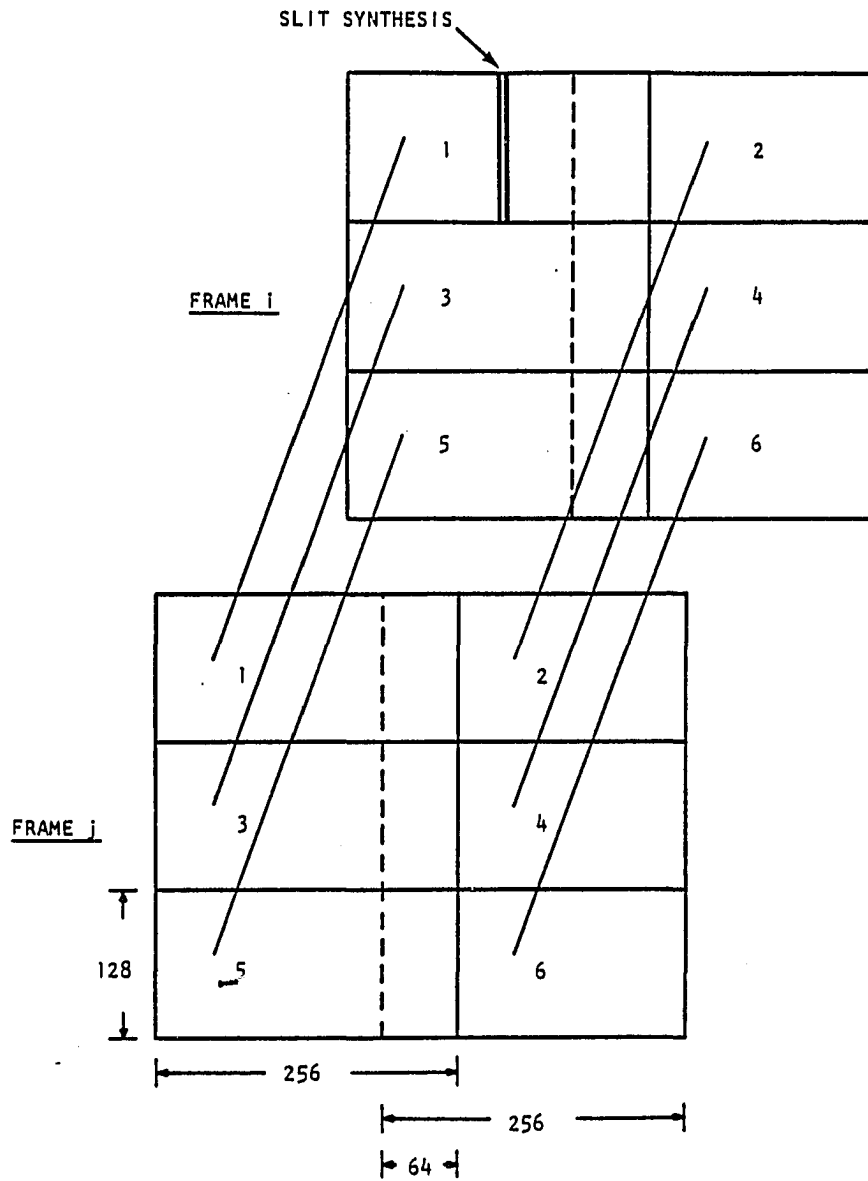


Fig. 4.8. Schematic illustrating the noise power spectrum analysis.

$$S = \sum_k \sum_i \sum_{j=i+2}^{14} \left| \mathcal{F} \left\{ w_{ki} - w_{kj} \right\} \right|^2 . \quad (4.14)$$

Let N denote the number of such subtractions. The relative noise power spectrum is then given by

$$W_{\Delta q/q} = \frac{L_y}{X} \frac{S}{2N} , \quad (4.15)$$

where L_y is the physical slit length, and X is the physical width of the noise profile. (Note that a factor of two is involved, as the subtraction process effectively doubles the noise power.)

With 6×14 independent samples, the statistical error is estimated to be 11%. This fluctuation can be reduced if frequency resolution is sacrificed. For the data presented in the next chapter, the highest frequency resolution is preserved, since the shape of NPS is as important as the absolute value. A high degree of permutation was necessary to average out the cross power due to subtraction. An analysis of NPS by a simple permutation showed significantly more fluctuation in the resultant spectrum.

Subtraction was of crucial importance. Figure 4.9 shows sample noise images before and after subtraction. Those images resulted from the excitation of the XR11 with visible fluorescent light. The phosphor granularity is quite noticeable in the raw image, and is removed by the subtraction procedure. By looking at the line profiles, one observes an appreciable amount of medium-frequency

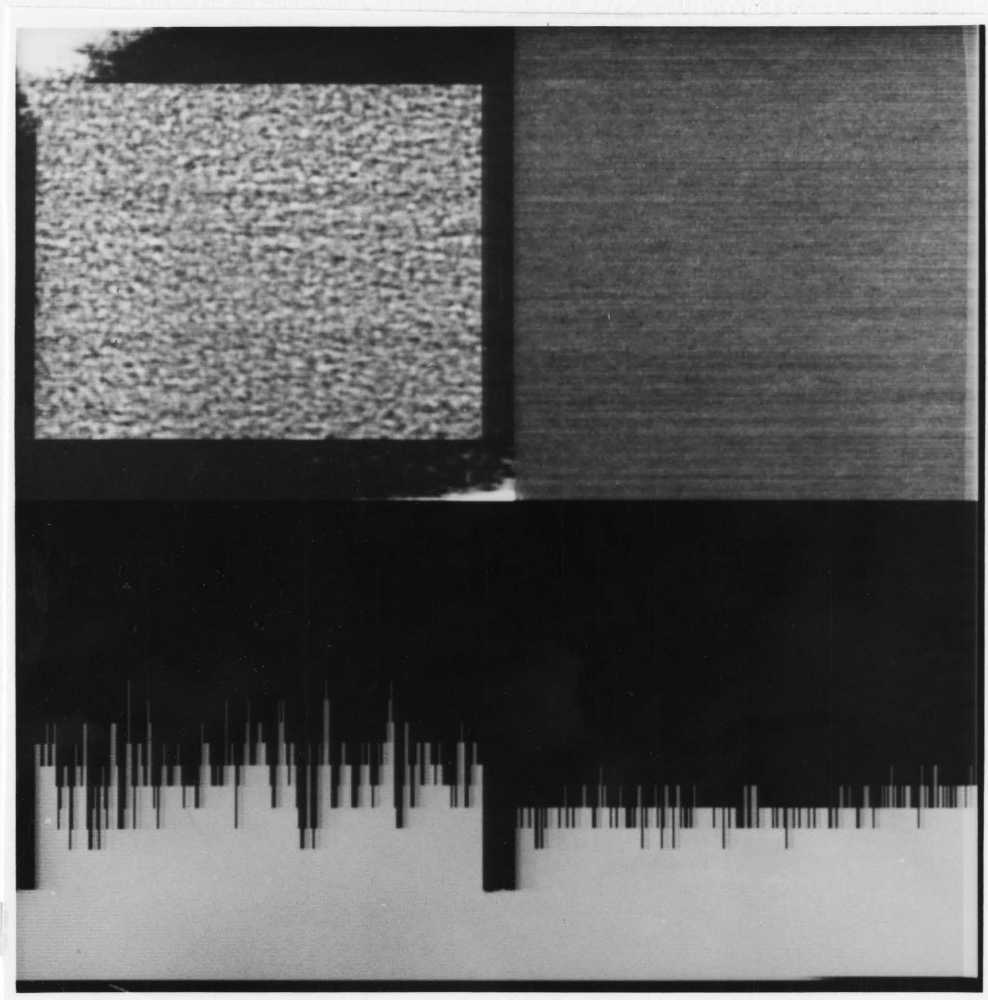


Fig. 4.9. Noise images before and after subtraction of fixed-pattern noise of output phosphor.

Left: before subtraction

Right: after subtraction

noise components. The mean squared noise in the raw image is obviously greater than that of the subtracted image, even though the subtraction effectively doubles the random noise power.

CHAPTER 5

RESULTS AND DISCUSSION

This chapter compares the experimental findings with the numerical calculations developed in Chapter 3. Special considerations for the design of a new system are also discussed.

Numerical Calculations

Numerical calculations on the quantum efficiency, scintillation DQE, and DQE of a bremspectrum exposure are presented in this chapter along with their experimental data. X-ray data involved in the calculations were taken from Plechaty et al. (1975). A computer program was developed to calculate the quantum absorption and the k-escape probability for a given x-ray energy and CsI thickness. In the program, the total thickness was divided into sublayers with a thickness of 1/100th that of the mean free path of the primary x-ray photon. The k-escape probability was calculated for each sublayer by assuming that the fluorescent x-rays are emitted isotropically. Due to a lack of knowledge on the composition and thickness of the intensifiers' vacuum windows, Pyrex glass was assumed for all five XRIIs unless a special window material is specifically noted. Thickness was estimated by fitting the experimentally measured quantum efficiency data. By this procedure, as will be seen later, a reasonably good agreement was achieved.

For measurement which involved a bremspectrum, the relative spectrum was calculated under the assumption of a thick tungsten target (Johns and Cunningham, 1981). A 2 mm inherent aluminum filtration was also assumed. This relative spectrum was converted to absolute photon fluence by the measured exposure. For x-ray tube voltages above 80kV, the tungsten characteristic lines were included in the calculation. This calculation was based on the K-fluorescent yields of tungsten reported by Hoffman and Phelps (1974). A quadratic equation relating the K-fluorescence to the x-ray tube peak voltage was obtained by the least-square fit. From the calculated bremspectrum, the DQE was then evaluated according to Equation 3.13.

Non-imaging Properties

Scintillation Distribution

The scintillation pulse height distributions (SPHDs) for five XRIIs and five energies are shown in Figure 5.1. The distributions are ordered by increasing source effective energy from left to right and by increasing CsI layer thickness from top to bottom. Under each of the distributions, the corresponding scintillation DQE is listed.

As the incident energy is increased beyond the absorption edge of C_s or I, one notices more and more k-escapes. They also occur with the Ba and Ce sources because some of their lines are above the I or Cs edge (see Table 4.1). The small peak at the right side of the Ag distribution, however, is caused by the Am 241 background. This background is always excluded for the analysis.

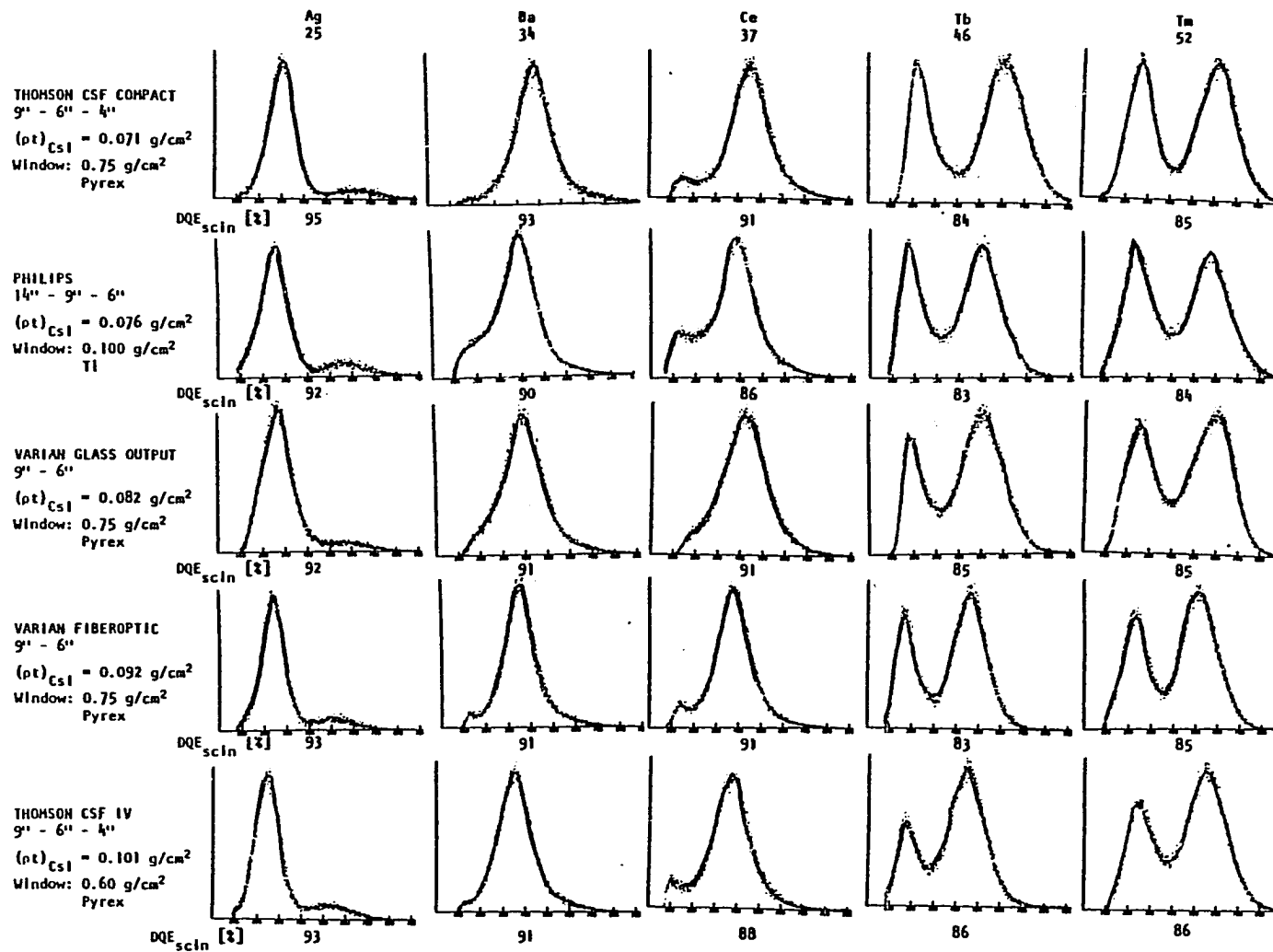


Fig. 5.1. Scintillation pulse height distributions for five XRIIs and five x-ray photon energies.

As was discussed in Chapter 3, the scintillation DQE is determined by two mechanisms: the AED and the OPD. From Equation 3.10, the AED starts contributing its effect once the k-escape occurs. This contribution is noted on Figure 5.1 as a general trend of decreasing DQE as the escape effect becomes more pronounced. However, at higher photon energies the fractional energy loss due to k-escape decreases. This explains the higher DQE value for the Tm source as compared with that for Tb.

The x-ray energy dependence of the optical pulse distribution (OPD) was analyzed using the photo peak distributions. For SPHD showing a k-escape effect, the overlapped region was resolved by curve fitting. The pertinent first order statistical parameters of the resultant distributions are listed in Table 5.1. The relationship between the variance and the mean is of primary interest, as it indicates the nature of the statistical process. If the OPD was determined mainly by the scintillation conversion process, a Poisson-like distribution resulted, indicating a linear relationship between the variance and mean. On the other hand, if the OPD was dominated by unequal light propagation from different parts of the CsI scintillator, the standard deviation instead followed the mean (Swank, 1973). In this case, the information factor resulting from the OPD would be a constant (see Equation 3.4). However, the table shows that neither of these cases is followed. With the exception of Ag, a general trend is observed as a relatively narrower distribution as the energy increases. Nevertheless, its information factor, I_{OPD} ,

Table 5.1. First-order Statistical Parameters of Photo-peak Distributions (XR11: Thomson-CSF compact)

Source	Effective Energy (keV)	σ/m	σ^2/m (keV)	I_{OPD}
Tm	52	0.169	1.51	0.972
Tb	46	0.184	1.61	0.967
Ce	37	0.238	2.06	0.946
Ba	34	0.257	2.41	0.938
Ag	25	0.234	1.25	0.948

is a rather insensitive function of the energy as shown in the last column, indicating a range from 0.94 to 0.97 with a maximum difference of 3%. This confirms our previous assumption about the constant I_{OPD} in Chapter 3. In the following analysis, a mean value of 0.95 would be used, resulting in an error of no more than 2%.

The thickness dependence on AED is more interesting. In Figure 5.1, as one follows the vertical direction on the Tm source, one observes a trend of decreasing k-escape fraction as the layer thickness increases. Figure 5.2 shows the measured k-escape fractions of the five XRIIs at the 52 keV x-ray energy. For comparison, a calculated curve is also shown in the figure. With but one exception, the measured values agree within 4% with the theoretical ones. The exception occurs for the 14" Philips intensifier with a measured CsI layer thickness of 76 mg/cm^2 . Its high k-escape fraction is also observed for other x-ray energies as shown in Figure 5.1. One possible explanation for this peculiar behavior is given below.

During the measurements of sensor thickness, materials in addition to cesium and iodine were noticed in the transmitted spectra of some XRIIs, as demonstrated in Figure 5.3. Of the five XRIIs used in this study, the two Varian intensifiers show appreciable amounts of barium, while the Philips intensifier shows both barium and lanthanum in their spectra. The locations of these additional high-Z materials remained a mystery for a long time. It was finally determined for the Varian intensifiers that barium was located in the output window to absorb the transmitted x-rays. However, the

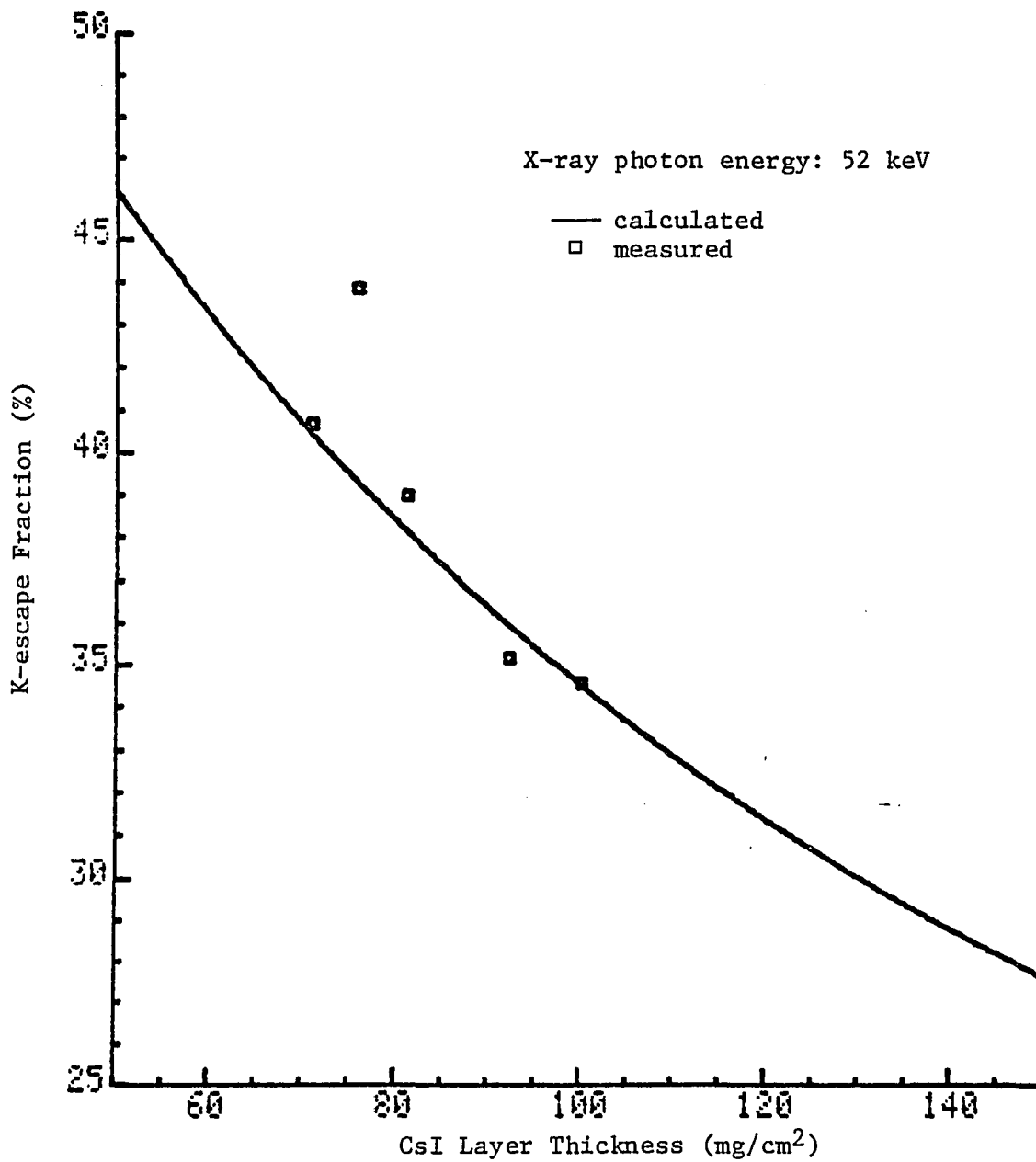
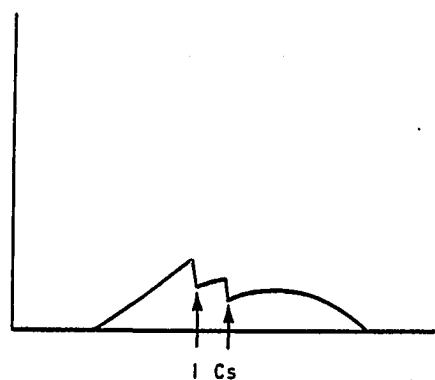


Fig. 5.2. K-escape fraction as a function of CsI layer thickness.

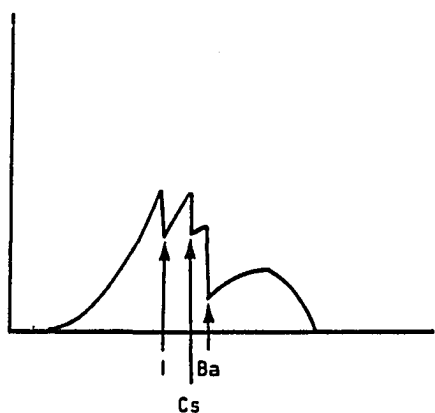


(a) Siemens special XR11

$$(\rho t)_I = 0.0173 \text{ g/cm}^2$$

$$(\rho t)_{Cs} = 0.0188 \text{ g/cm}^2$$

$$(\rho t)_{CsI} = 0.0361 \text{ g/cm}^2$$



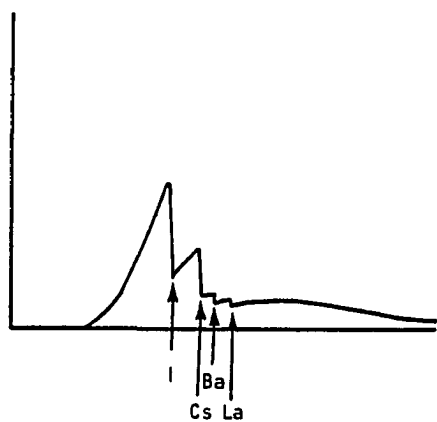
(b) Varian 9-in. 6-in. very high resolution

$$(\rho t)_I = 0.0142 \text{ g/cm}^2$$

$$(\rho t)_{Cs} = 0.0168 \text{ g/cm}^2$$

$$(\rho t)_{CsI} = 0.0309 \text{ g/cm}^2$$

$$(\rho t)_{Ba} = 0.046 \text{ g/cm}^2$$



(c) Philips 14-in. 9-in. 6-in.

$$(\rho t)_I = 0.0376 \text{ g/cm}^2$$

$$(\rho t)_{Cs} = 0.0385 \text{ g/cm}^2$$

$$(\rho t)_{CsI} = 0.076 \text{ g/cm}^2$$

$$(\rho t)_{Ba} = 0.016 \text{ g/cm}^2$$

$$(\rho t)_{La} = 0.01 \text{ g/cm}^2$$

Fig. 5.3. X-ray spectra transmitted by various x-ray image intensifiers.

mystery still exists for the Philips intensifier. Its high k-escape fraction could be understood if either barium or lanthanum was located in its scintillation layer resulting in additional k-escapes.

Quantum Efficiency and DQE

Figure 5.4 shows a typical MPHD with a short integration time, together with the theoretical Poisson distributions. The discrete character is clearly noticeable and is washed out gradually due to the scintillation distributions. With the aid of the corresponding SPHD, the quantum efficiency is calculated by Equation 4.3 or 4.5. As pointed out earlier, the results obtained by these two equations were in self-agreement of 2% for all measurements. With the quantum efficiency data at hand, the window thickness is fitted with the theoretical calculations. In the calculation, spectral lines of individual sources were considered.

Table 5.2 provides an easy comparison of all measured and calculated values of quantum efficiency, scintillation DQE, and total DQE. The experimental values constitute averages over several measurements, often as many as five. The calculated and measured quantum efficiencies are listed in row (a) and row (b), respectively. In most cases, their correlation is within a few percent. This correlation again confirms the validity of the calculations.

The last column lists the total DQE, the product of measured quantum efficiency and scintillation DQE. From the results, an information transfer efficiency of from 30 to 50% over the diagnostic energies can be expected for most commercially available XRIIs.

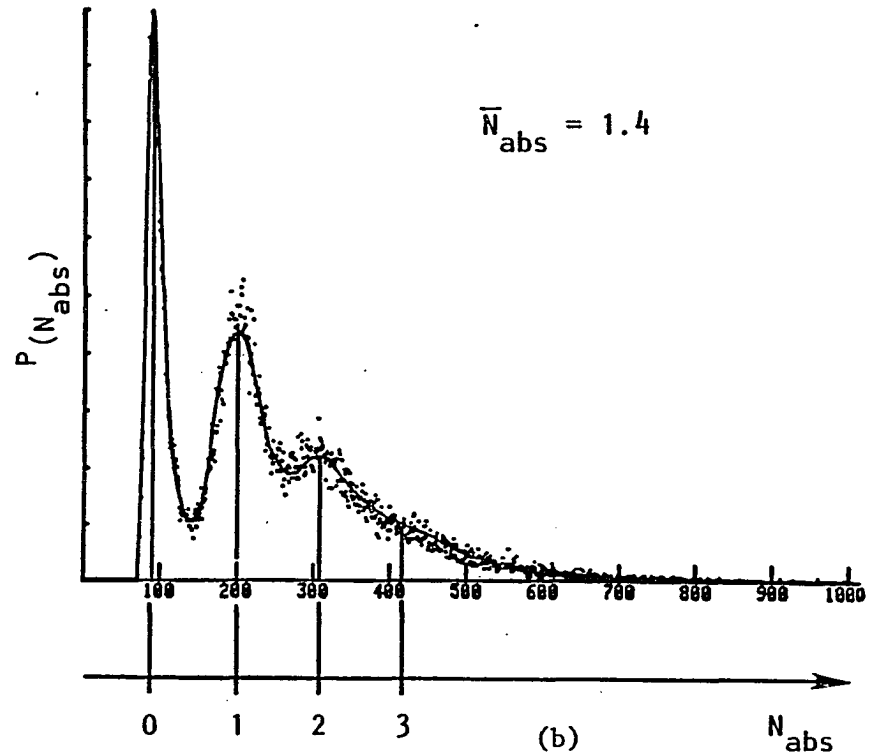
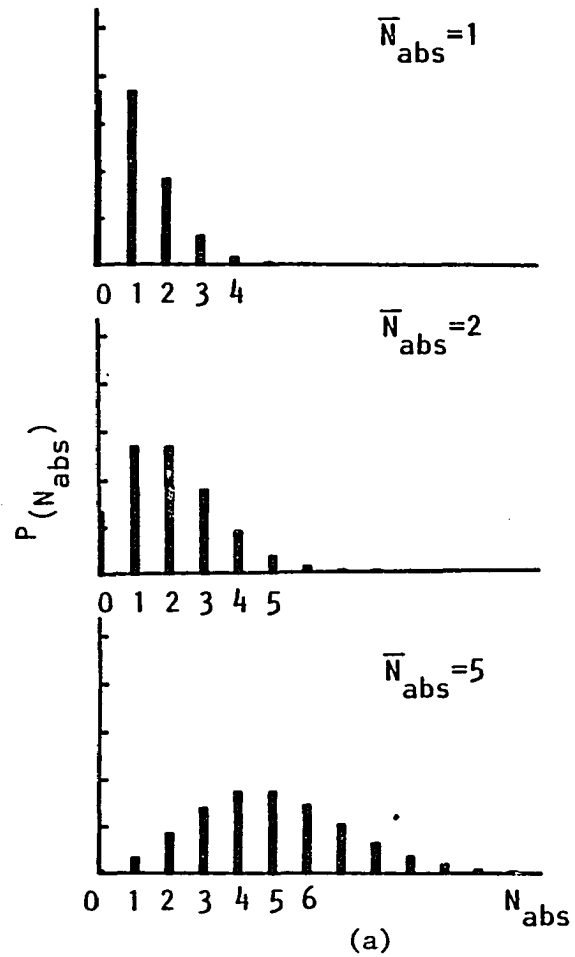


Fig. 5.4. Multiple pulse height distribution as compared to Poisson distributions.

(a) Calculated for different mean absorbed events.

(b) Measured multiple pulse height distribution.

Table 5.2. Summary of Non-imaging Properties of Five XRIIs for Five X-ray Energies.

X-ray Image Intensifiers Under Test	Window Material/ thickness (mg/cm ²)	CsI Layer thickness (mg/cm ²)	Quantum Efficiency (%)					Scintillation DQE (%)					DQE (%)					
			Source, Effective Energy (keV)															
			Ag 25	Ba 34	Ce 37	Tb 46	Tm 52	Ag 25	Ba 34	Ce 37	Tb 46	Tm 52	Ag 25	Ba 34	Ce 37	Tb 46	Tm 52	
Thomson CSF 4-6-9-in. compact	Glass 750	71	a) 23 b) 24	29 28	42 43	53 53	47 51		95	93	91	84	85	23	26	39	44	43
Thomson CSF 4-6-9-in. IV	Glass 600	100	a) 34 b) 29	40 41	53 52	65 63	59 57		93	91	88	86	86	27	37	46	54	49
Philips 6-9-14-in.	Titanium 100	76	a) 27 b) 30	34 34	48 47	61 62	54 56		92	90	86	83	84	28	31	41	52	46
Varian 6-9-in. Glass output	Glass 750	82	a) 25 b) 28	32 34	45 40	57 52	51 49		92	91	91	85	85	26	31	36	44	42
Varian 6-9-in. Fiber-optic output	Glass 750	92	a) 26 b) 30	35 36	48 46	60 63	55 58		93	91	91	83	85	28	33	42	52	50

a) calculated by Eq. (3.8)
 b) measured by pulse height distributions

Imaging Properties

A Thomson-CSF compact XR11 (Model TH 9428D GK-V) was used in the study of imaging properties (see Table 5.2). It has three internal electronic magnifications to provide a 9", 6", or 4" nominal input field. The 9" and 4" modes were used in this study.

Signal-Induced Background and X-Ray Scatter

The amount of signal-induced background was studied first to serve two purposes. Experimental consistency can be verified by comparing it with the corresponding MTF measurement. Most importantly, the amount of x-ray scatter within the XR11 can be estimated by analyzing the contrast data for different x-ray spectra. The results of the contrast measurements are shown in Figure 5.5 for both 9" and 4" modes. During the measurements, x-ray exposure rates were adjusted so that the same brightness level, B_0 , was recorded. This reference brightness was obtained with 60 mR/mn for the 50 kVp spectrum in the 9" mode.

The effect of scattering can be observed as the lower contrast for the higher effective x-ray energy in either mode. As was derived in Equation 4.10, the extrapolated contrast factor at vanishingly small disc diameter is the inverse of the energy fraction f_b of the background. Table 5.3 lists these background energy fractions for easy comparison and reference. Row 4 shows the amount of scatter resulting from the difference between the 50 kVp and 90 kVp spectra. It clearly indicates that the scattering effect is significantly less for the 4" mode due to its smaller input field. At 50 kVp,

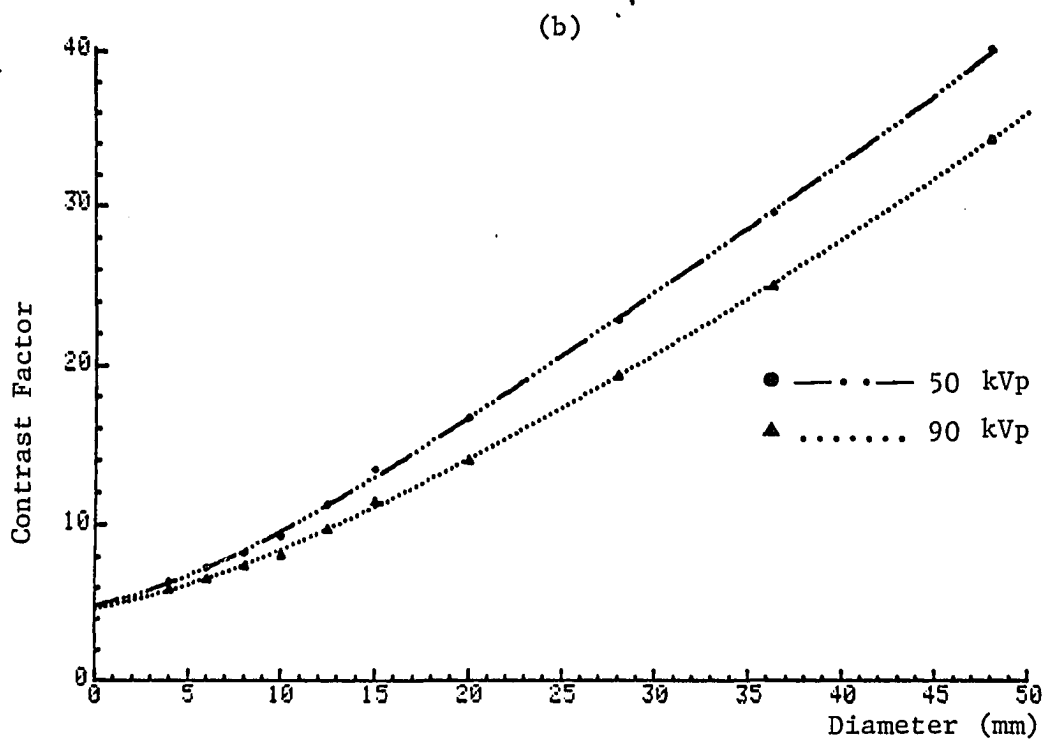
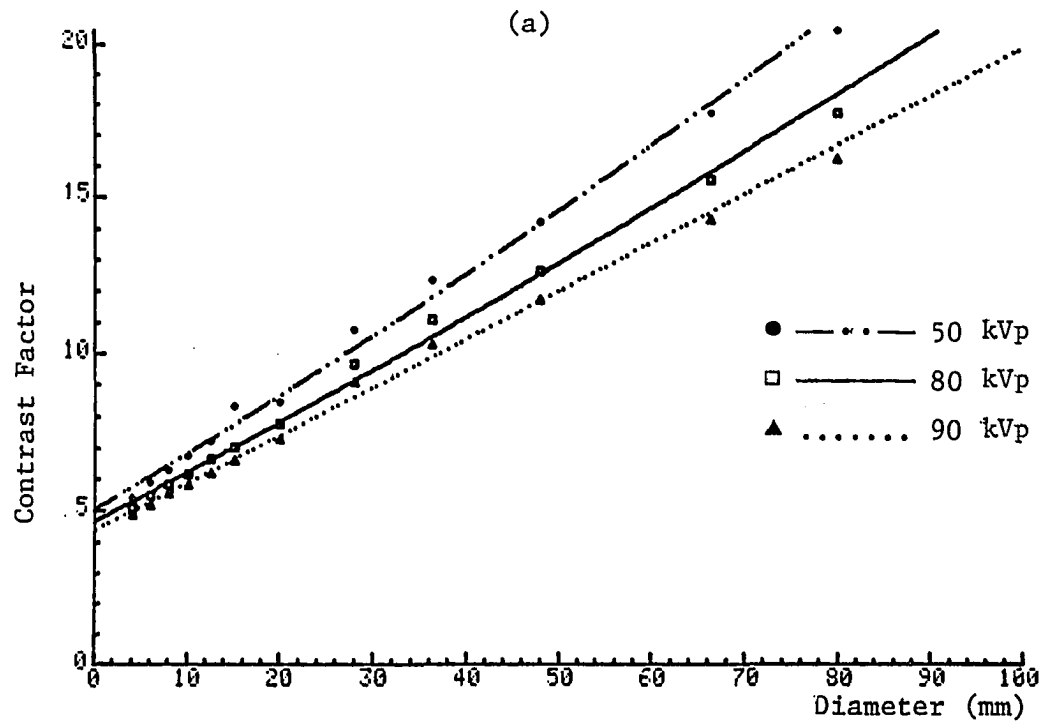


Fig. 5.5. Contrast factor as a function of lead disc diameter.

(a) 9" mode

(b) 4" mode

Table 5.3. Background Energy Fractions for two Magnification Modes and Three X-ray Spectra

	Spectrum	9" Mode	4" Mode
1.	50 kVp	19.8%	20.4%
2.	80 kVp	21.3%	--
3.	90 kVp	22.8%	21.2%
4.	row 3-row 1	3.0%	0.82%

the 4" mode has a slightly higher background than expected, as a higher electron density near the weak field cathode region results in more electron scattering. However, due to the proximity of these two values, one may assume that the x-ray scatter is negligible for this spectrum. Correspondingly, the numbers listed in Row 4 represent the total scatter fractions for the 90 kVp spectrum as 3% and 0.9% for the 9" and 4" modes, respectively.

As was previously discussed, x-ray scattering reduces the image contrast without affecting the noise power spectrum. According to Equation 2.7, the DQE is reduced correspondingly by the square of the x-ray scatter fraction. Therefore, in the worst case as for 90 kVp at the 9" mode, the information loss resulting from x-ray scattering is 6%.

Modulation Transfer Function

Figure 5.6 shows two MTF curves for the 80 kVp spectrum at the 9" mode. The lower curve is the MTF of the overall system and the upper one is that of the XRII alone, as corrected by the lens/camera contribution. System MTFs will be used in connection with the NPS discussion, since the emphasis there is their ratio which determines the information bandwidth. Correction on both quantities is therefore unnecessary. In this subsection, all discussions are related to the MTF of the XRII alone.

Two aspects of MTF can be discussed, namely its contrast reduction and spatial behavior. From Equation 3.15, the extrapolated MTF at zero frequency is simply given by $f_i = 1 - f_b$. Therefore, the

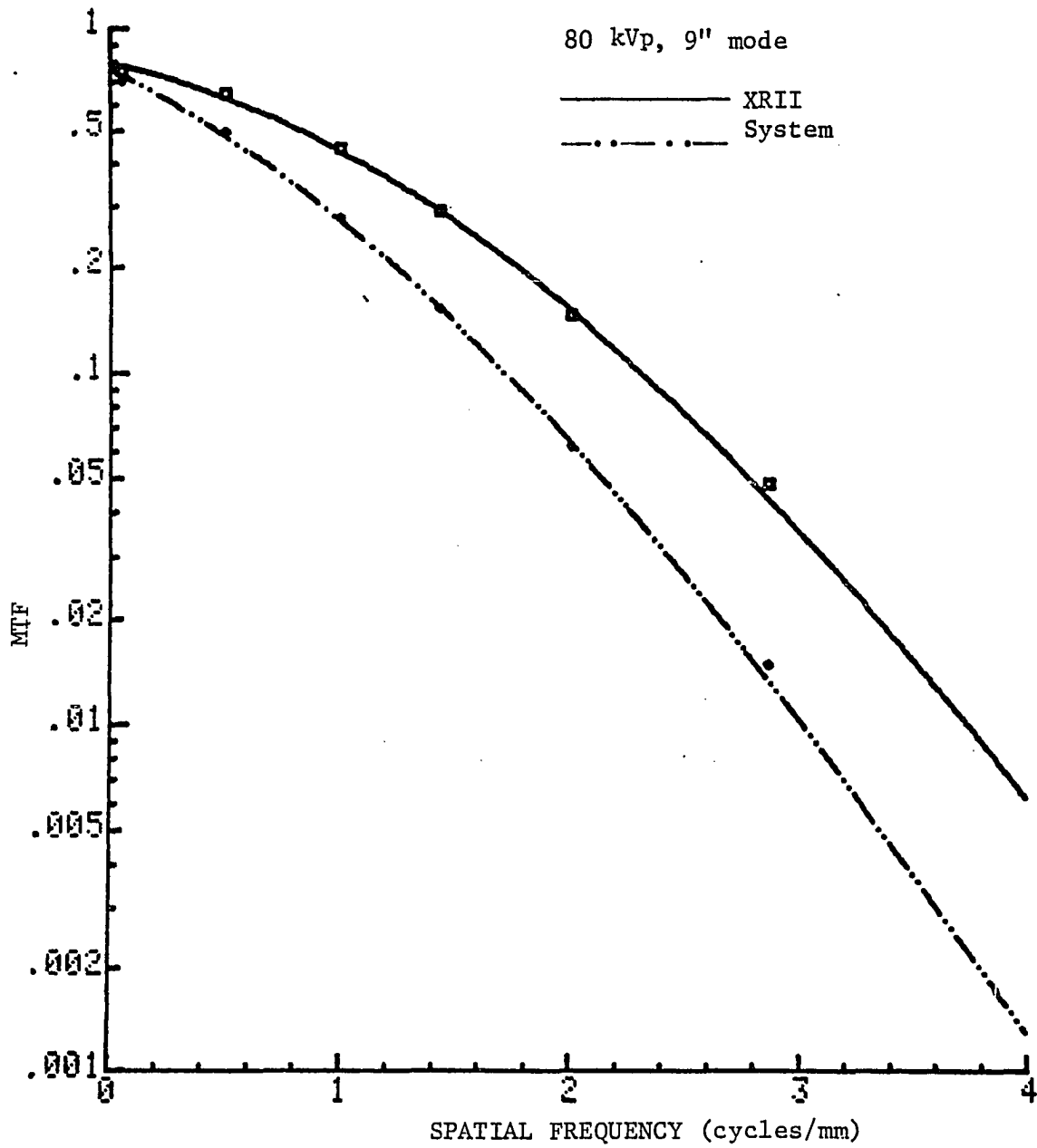


Fig. 5.6. Modulation transfer function of the overall system and XR11 alone.

amount of contrast reduction f_b can be compared with that obtained by the contrast measurements. A 20.7% contrast reduction is noted in this figure as compared to 21.3% in Table 5.3 for 80 kVp at the 9" mode. This agreement holds for all other measurements within an error of 7%.

The spatial behavior of the MTF is independent of the x-ray spectrum, as anticipated. Figure 5.7 shows the MTF for three spectra at the 9" mode. The deviation of 90 kVp MTF at higher frequencies is simply due to the incapability of curve fitting with a limited number of data points. Except for a constant scaling factor, the three follow the same frequency dependence.

Figure 5.8 shows the MTF of the 4" and 9" modes at 80 KVp. At the 5% cutoff, the MTF bandwidths are 2.8 and 4 cycles/mm for the 9" and 4" modes, respectively.

Noise Power Spectrum

The three noise components of the system were obtained from NPS measurements found after exposure of the XRII to x-rays and to visible light and after exposure of the video camera tube to visible light. The results are shown in Figure 5.9. For the case of the x-ray exposure, the resultant NPS contains all the three system components. However, in the case of light exposure on the x-ray image intensifier, the CsI scintillator acts as a binomial stage for transmitting the light photons. Therefore, the CsI noise component is eliminated from the resultant spectrum (notice: light exposures to the x-ray image intensifiers were possible after removal of the

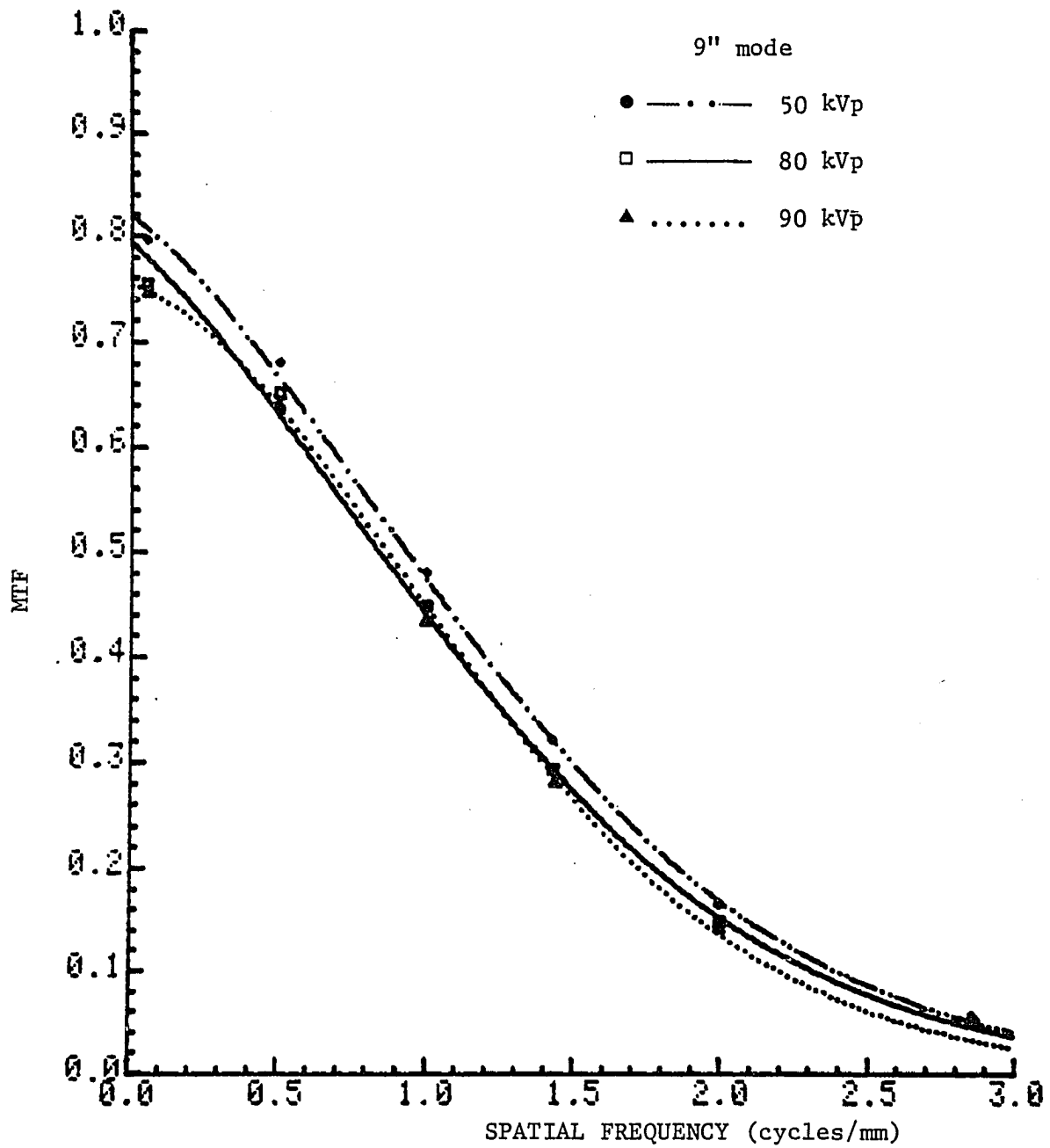


Fig. 5.7. Modulation transfer function of the XR11 for three x-ray spectra.

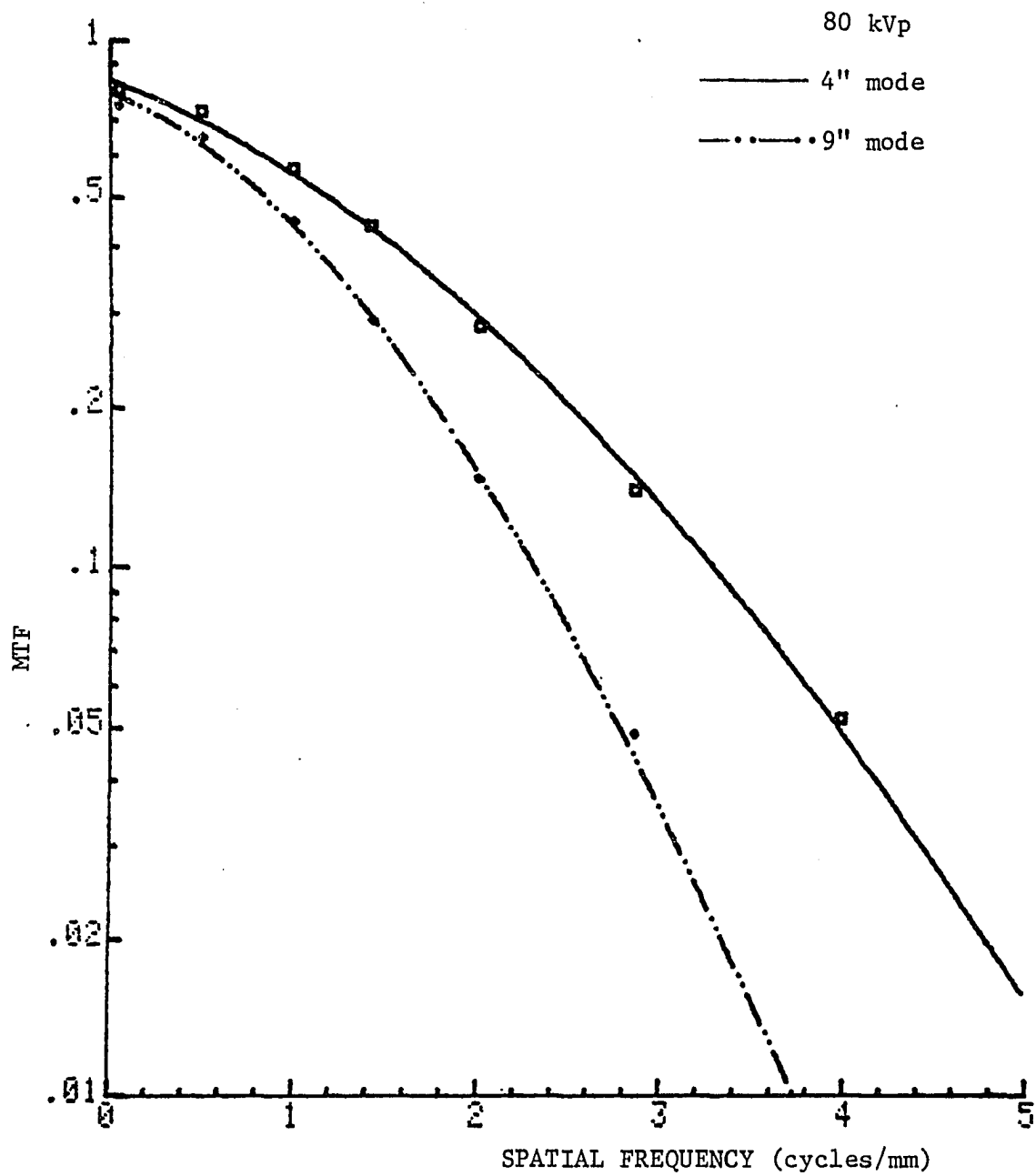


Fig. 5.8. Modulation transfer function of the XRII in 4" and 9" modes.

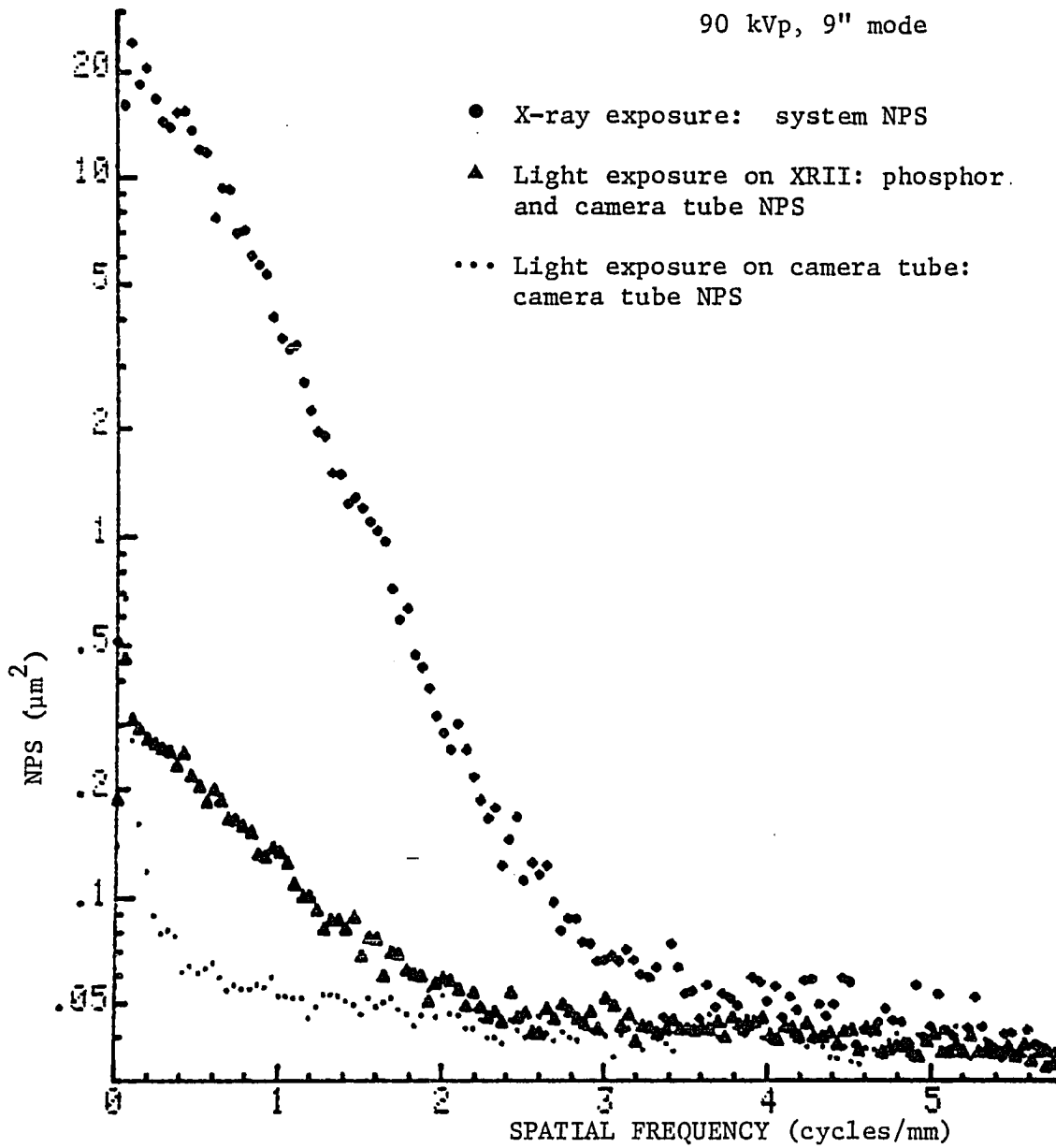


Fig. 5.9. Noise power spectra due to x-ray and light exposure.

light absorbing protective cover of the XII housing). The bottom curve shows the recording white noise which was obtained by light exposure of the video camera tube.

From these three measurements, the three NPS components can be isolated by subtracting one curve from the other. Figure 5.10 shows these three NPS components. In this figure, the phosphor shows a smaller but significantly wider NPS than does the CsI layer. At all frequencies, its NPS is small as compared to either the CsI component or the white noise. Therefore, the phosphor NPS component is omitted from the following discussion regarding the system noise.

At zero frequency, the quantum gain accumulated up to the output phosphor can be determined by the ratio of the NPS values of the CSI layer and the output phosphor. This gain is determined to be about 80. Similarly, the gain of the whole system is estimated to be 600. For comparison, these two measured gains are listed in Table 5.4 along with the calculated gain of each system component. A mean deposited energy of 41 keV calculated for the 90 kVp spectrum was used for the calculation. The readout efficiency of 35% was estimated from the lag characteristics. General agreement exists between them.

Experimental consistency can further be verified by Figure 5.11, which shows the NPS resulting from two exposure levels. The high exposure was accurately controlled to be 20 times that of the other, resulting in the same recording level. Correspondingly, both the system gain and NPS are expected to be reduced by the same factor.

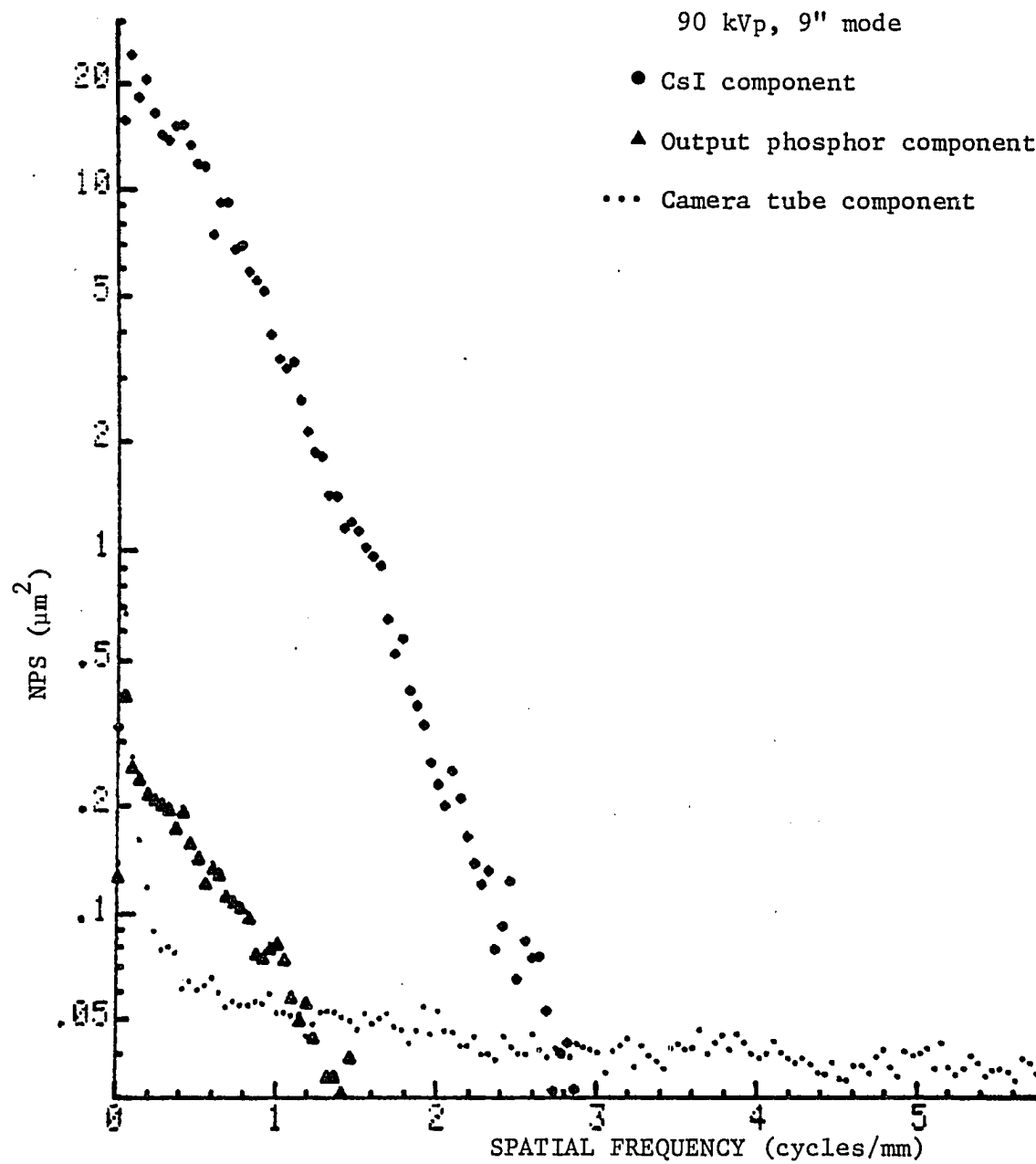


Fig. 5.10. NPS components of CsI layer, output phosphor, and camera tube.

Table 5.4. Cumulative Quantum Gain at Each System Component
(Mean Deposited X-ray Photon Energy: 41 keV*)

Stage	Quantum Conversion	Cumulative Gain	Measured
1. CsI Scintillator	50 scintillations/ keV	2050 photons	-
2. Photocathode	5%	103 photo- electrons	-
3. Electron Optics	80%	82 electrons	80
4. Output Phosphor**	63 photons/keV	1.3×10^5 photons	-
5. Lens***	3.2%	4060 photons	-
6. Video Sensor	60%	2440 electrons	-
7. Readout	35%	850 electrons	600

*Calculated for 90 kVp bremspectrum with 0.25mm Cu filtration

**Anode voltage = 32 kV

***F/1.5 Collimating lens; phosphor substrate index of 1.5; and tandem lens transmission of 70%

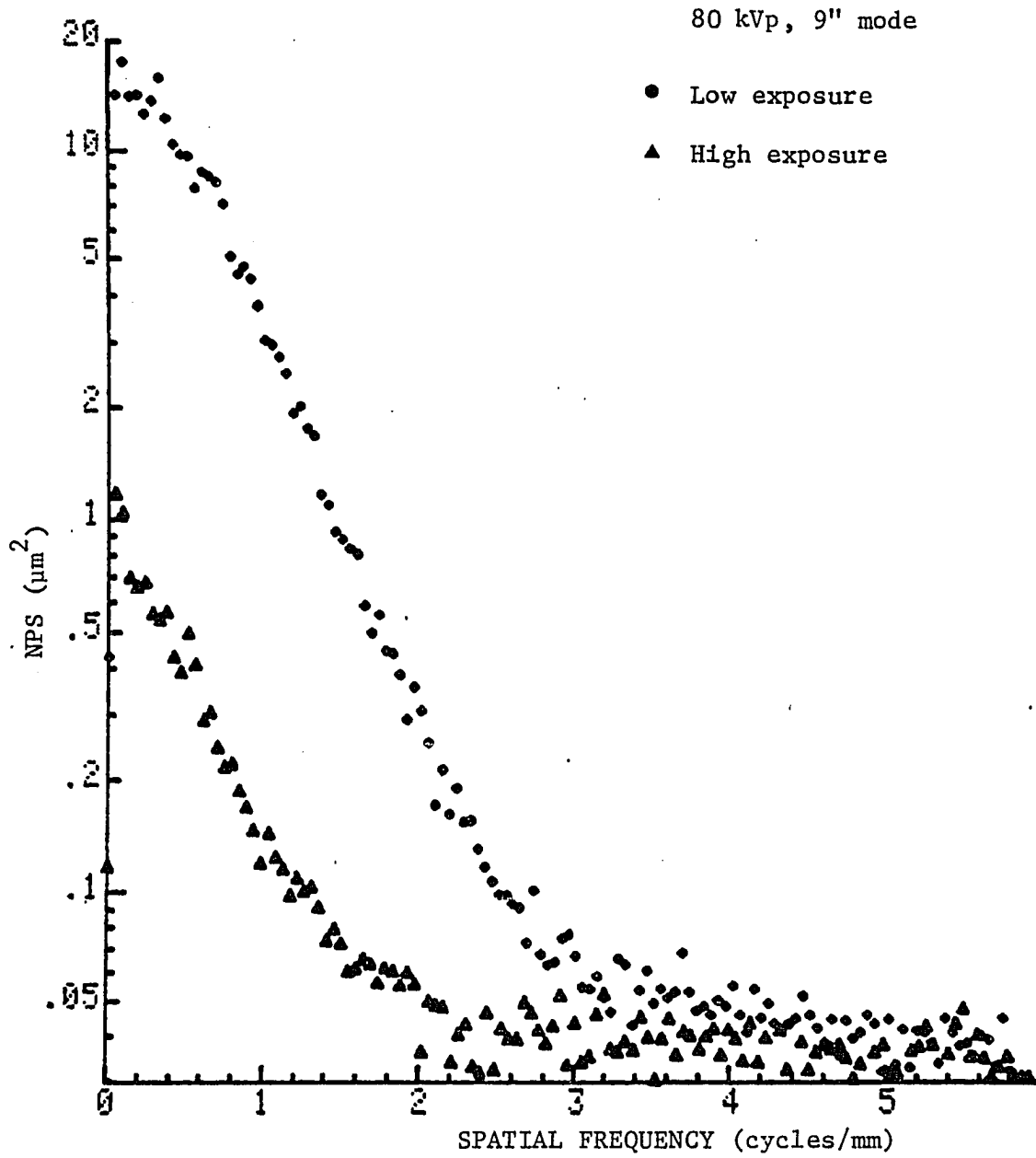


Fig. 5.11. Noise power spectra resulting from high and low x-ray exposures.

This is confirmed in the figure where the two noise power spectra are presented on a logarithmic scale. The high exposure curve is separated from the other by a factor of about 20 and they are in parallel up to 1 cycles/mm. This indicates that the shape of the noise power spectrum is practically independent of the exposure level.

Figure 5.12 shows on a linear scale the NPS curves of three x-ray spectra. The lowest curve corresponds to the 50 kVp spectrum while the highest one corresponds to 90 KVp. As the system gain is linearly proportional to the mean deposited x-ray energy within the CsI layer so is the zero-frequency NPS value. The mean deposited energies for the 90 kVp, 80 kVp, and 50 kVp spectra were calculated to be 40.8 keV, 33.1 keV, and 28.3 keV, respectively. To compare them with the measured NPS data, we chose the 90 kVp spectrum as an absolute reference by converting its NPS value of $24.6 \mu\text{m}$ to 40.8 keV deposited energy. The corresponding measured energies are determined to be 32.8 keV and 26.9 keV for the 80 kVp and 50 kVp spectra, respectively, in very close agreement with calculated ones. The maximum deviation is 5%.

The relationship between NPS and MTF^2 is of primary importance, as it determines the image information transfer efficiency of the system. As discussed in Chapter 3, the CsI NPS component follows the system MTF^2 dependence under the assumption that its needle-like layer structure eliminates the thickness effect. The validity of this assumption is illustrated in Figure 5.13 for 9" mode data, where the MTF^2 curve is scaled to coincide with the NPS curve. The ratio

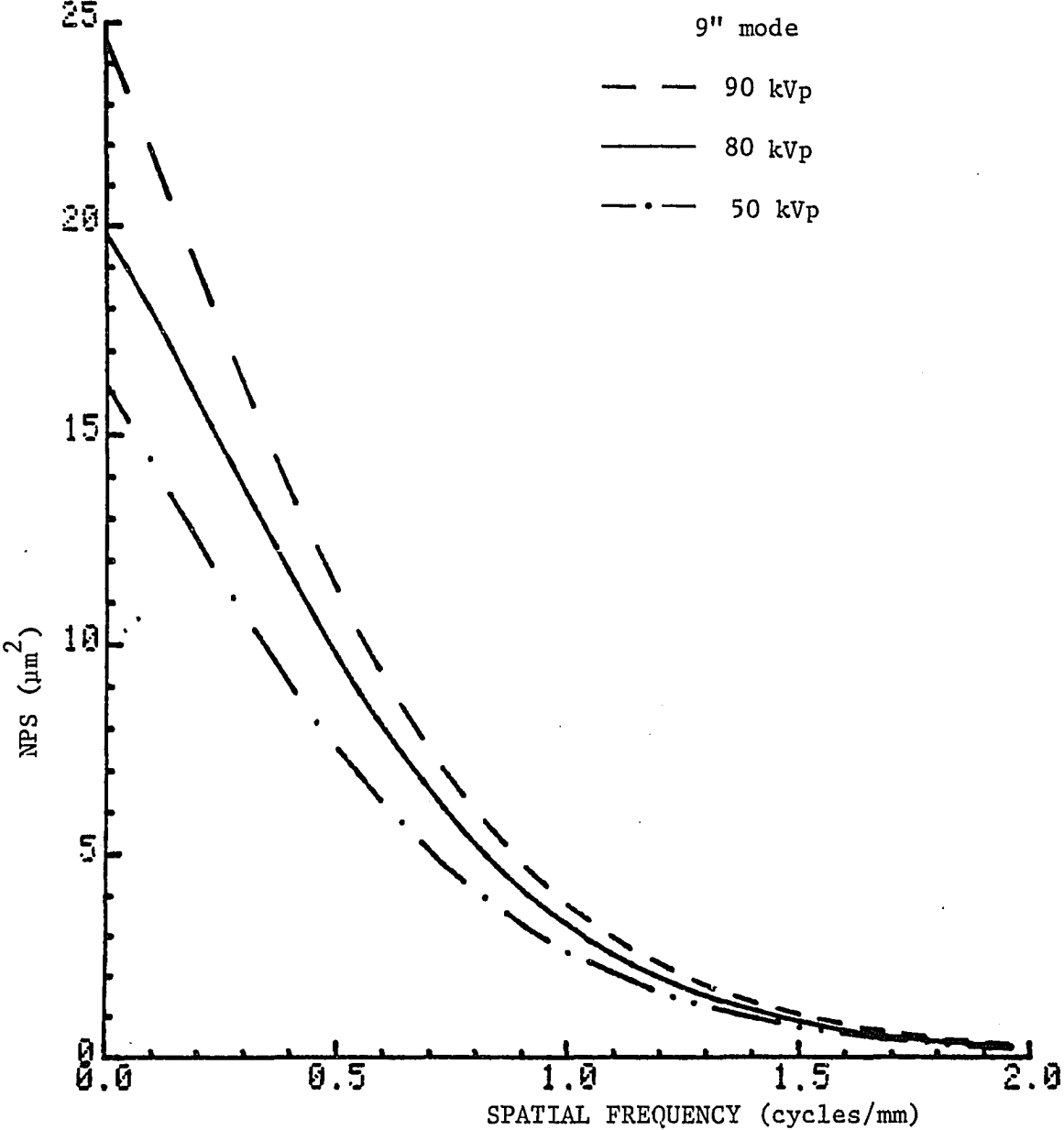


Fig. 5.12. Fitted noise power spectra for three x-ray spectra.

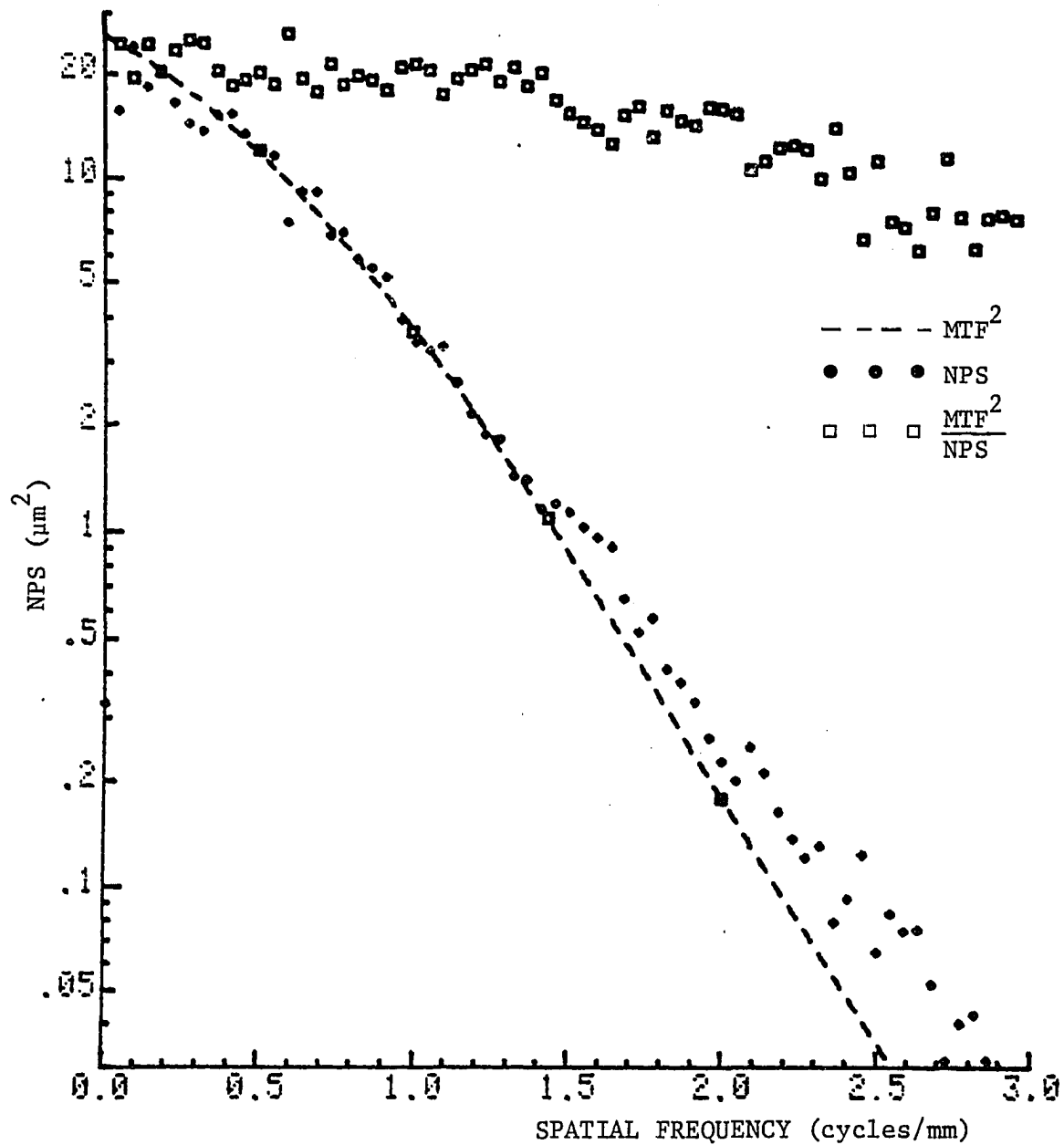


Fig. 5.13. NPS component of the CsI layer as compared with the system MTF² in 9" mode.

The system MTF² is scaled to coincide with the NPS at 0.3 cycles/mm. Their ratio is shown in arbitrary units.

of MTF^2 and NPS, which is proportional to DQE, is also shown in arbitrary units. We will call this ratio "normalized DQE" for ease of reference. The normalized DQE shows a nearly constant information bandwidth up to 3 cycles/mm. Beyond this point the baseline noise dominates the system and no experimental data on the CsI NPS component can be derived. At this frequency, the normalized DQE decreases by a factor of 3 from the zero frequency value. The frequency range is extended in Figure 5.14 for the 4" mode data. In this figure, the normalized DQE is reduced by factors of 3 and 6 at 3 cycles/mm and 5 cycles/mm, respectively. It can be argued that a DQE reduction by a factor of 6 corresponds to an equivalent MTF of 40% for a system with a white noise spectrum. This is a rather satisfactory performance. Furthermore, as will be discussed below, the system information bandwidth is always limited by other noise sources. The inherent wide information band provided by the CsI layer can be realized only within a certain range. Therefore, the effect of the CsI thickness on the MTF^2 dependence of NPS can be neglected for all practical purposes. In other words, we will consider the CsI layer to be providing a flat information band when system information efficiency is evaluated.

The normalized DQE for the experimental system is illustrated in Figure 5.15, together with its constituent MTF^2 and NPS. It shows a constant image information efficiency up to 2 cycles/mm. Beyond this frequency, the normalized DQE decreases gradually to a point where the baseline noise dominates the system. From this point,

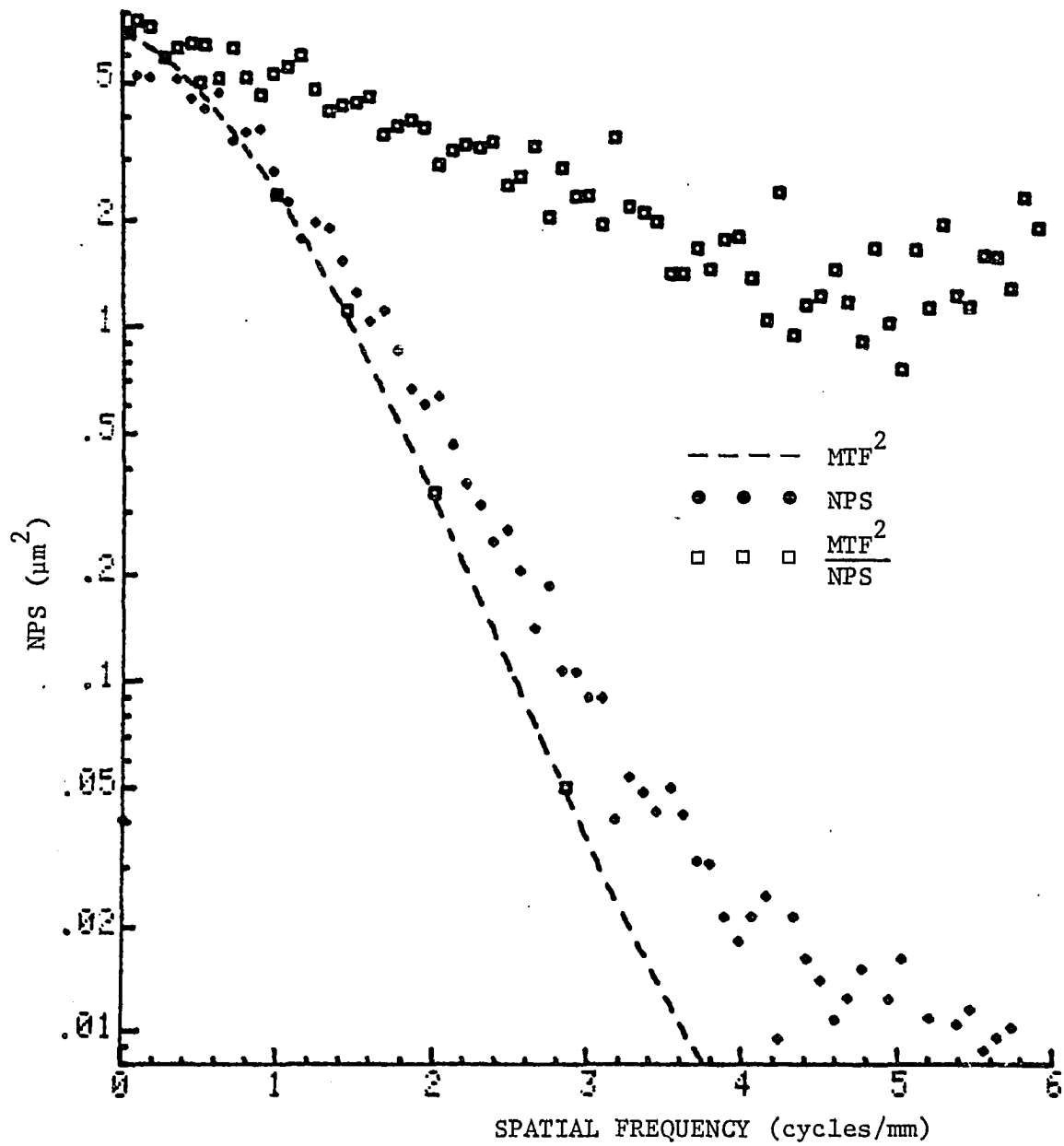


Fig. 5.14. NPS component of the CsI layer as compared with the system MTF^2 in 4" mode.

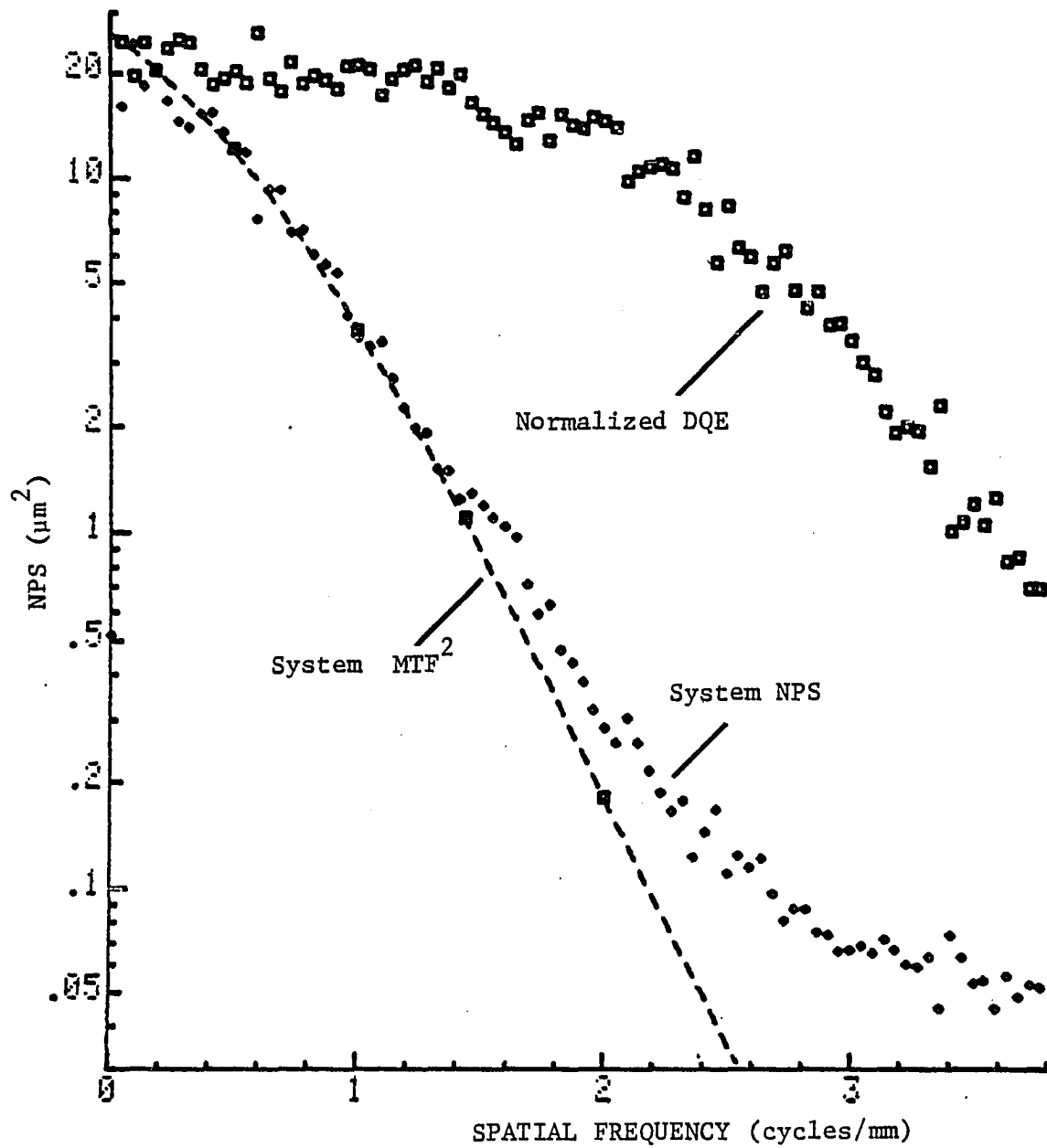


Fig. 5.15. Information transfer of the experimental system.

The information transfer is described by the normalized DQE in arbitrary units. The y axis is labeled for the system NPS.

the DQE drops at the same rate as does the MTF^2 . This is the general pattern of the image information transfer efficiency of an XRII system. It is the constant region which provides efficient image information transfer. The system parameters which determine this bandwidth will be emphasized later in this chapter.

As illustrated in Figure 4.9, an appreciable amount of fixed-pattern phosphor granularity was presented in the noise image. Figure 5.16 shows its effect on the resultant NPS. This was based on an analysis with the same data set as in the previous figure with the exception that the subtraction algorithm was removed from the NPS calculation. A significantly wider NPS spectrum was obtained, demonstrating the importance of the subtraction process used in NPS analysis.

As well, these experimental results are the direct consequence of the system linearity as discussed in Chapter 3. When a photographic film is used in an XRII system to record the image, as in cinefluorography, a grain coupling effect on the recorded NPS may arise. An early attempt to study this effect was made before the significant phosphor granularity was realized. Due to an inability to precisely register two film samples, the phosphor granularity contribution to NPS could not be removed. Consequently, no conclusive result was obtained on this grain coupling effect.

Detective Quantum Efficiency

From the knowledge of the input x-ray photon fluence, the complete image information transfer efficiency $[DQE(f)]$ can be

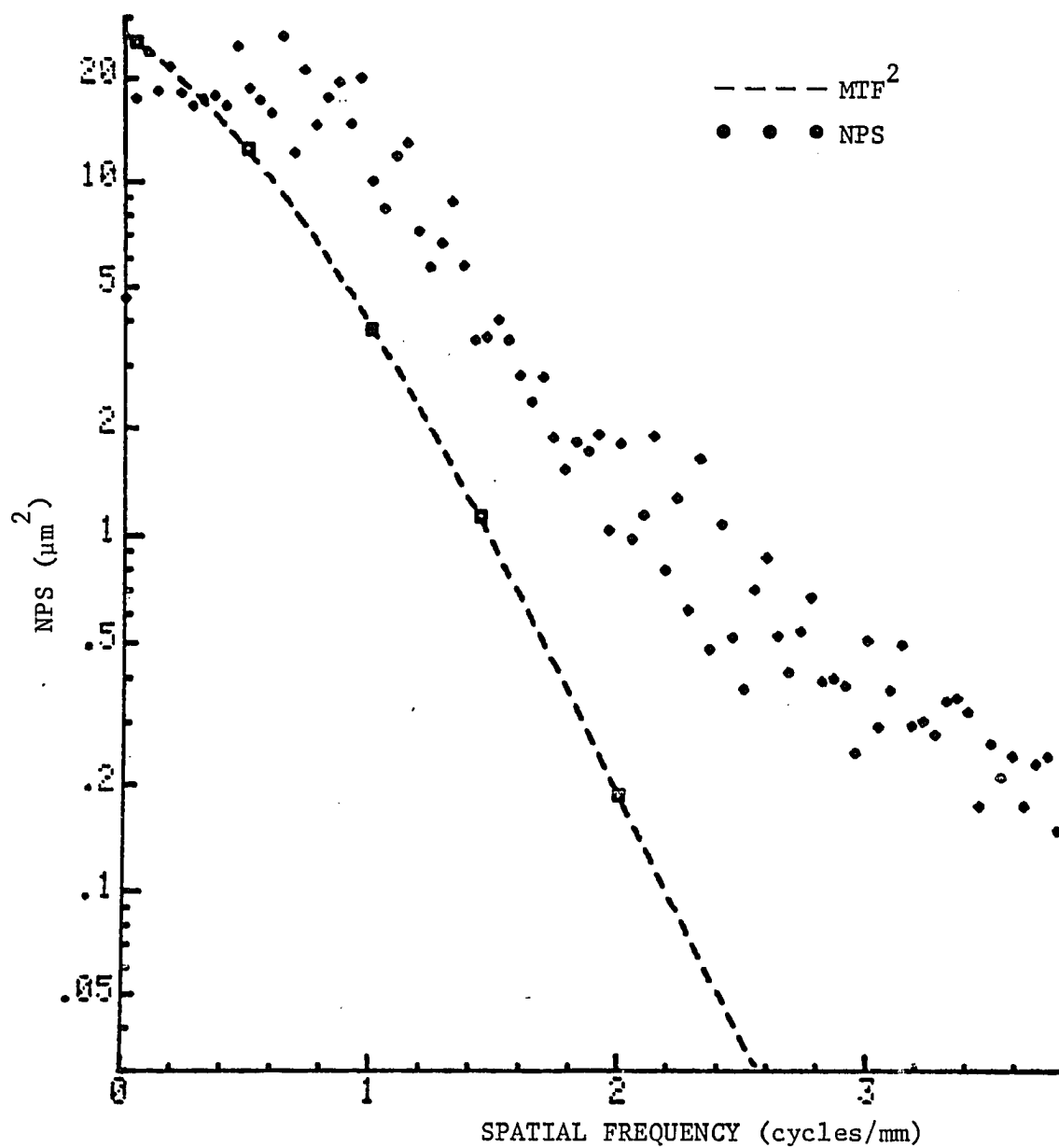


Fig. 5.16. Noise power spectrum obtained without subtraction of fixed pattern noise.

determined by Equation 3.6. The input photon fluence was obtained from the measured exposure using the calculated exposure-to-photon-fluence conversion factor. The image DQE of the CSI layer resulting from the three spectra at the 9" mode are shown in Figure 5.17.

They have a similar frequency dependence with a reasonably flat bandwidth of 3 cycles/mm. Their zero-frequency DQE values are listed in Table 5.5 along with the calculated values. Also shown in this table are the calculated information factors (see Equation 3.13) and the exposure-related data. The zero frequency DQE values vary slightly being higher for the 90 kVp and 80 kVp spectra than for the 50 kVp spectrum.

At first glance, one would expect a higher DQE at lower energy because of the increased energy absorption at lower energy. However, this higher energy absorption is offset by a lower energy transmission of the vacuum window. In Figure 5.18, the system DQE for the 90 kVp spectrum in the 9" mode is displayed in absolute units for future reference.

Design Considerations

Up to this point, the information properties of an experimental XRII system have been systematically analyzed. Physical and mathematical models have correctly been predicting the experimental results. Consequently, a high performance system can properly be designed with special consideration implied by these analytical models. These design considerations will be discussed based on the experimental data of the 90 kVp spectrum at the 9" mode.

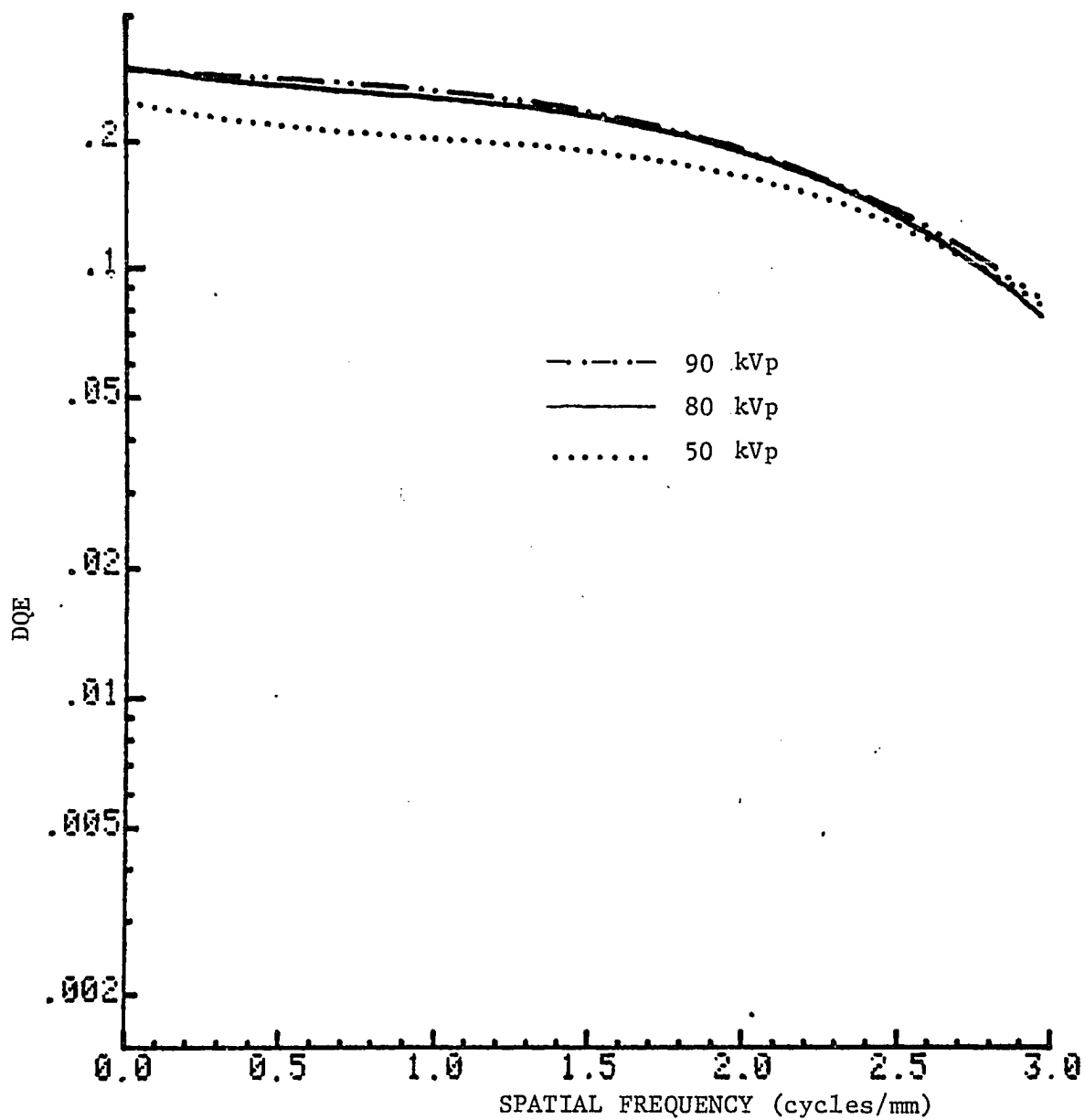


Fig. 5.17. Detective quantum efficiency of the CsI layer for three x-ray spectra.

Table 5.5. Measured and Calculated DQE for Three X-Ray Spectra
 (XRLI: Thomson-CSF compact, CsI = 71.7 mg/cm²,
 Pyrex window = 750 mg/cm²)

Spectrum	90 kVp (228 mg/cm ² Cu)	80 kVp	50 kVp
Exposure (mR)	0.27	0.66	1.74
Photon fluence (photons/mm ²)	7.14 x 10 ⁴	9.31 x 10 ⁴	1.84 x 10 ⁵
Quantum Efficiency	0.382	0.364	0.315
I _{XED}	0.939	0.944	0.985
\bar{I}_{SCIN}^*	0.849	0.837	0.846
DQE (calculated)	0.305	0.288	0.263
DQE (measured)	0.30	0.30	0.25

*I_{OPD} = 0.95 used in the calculation

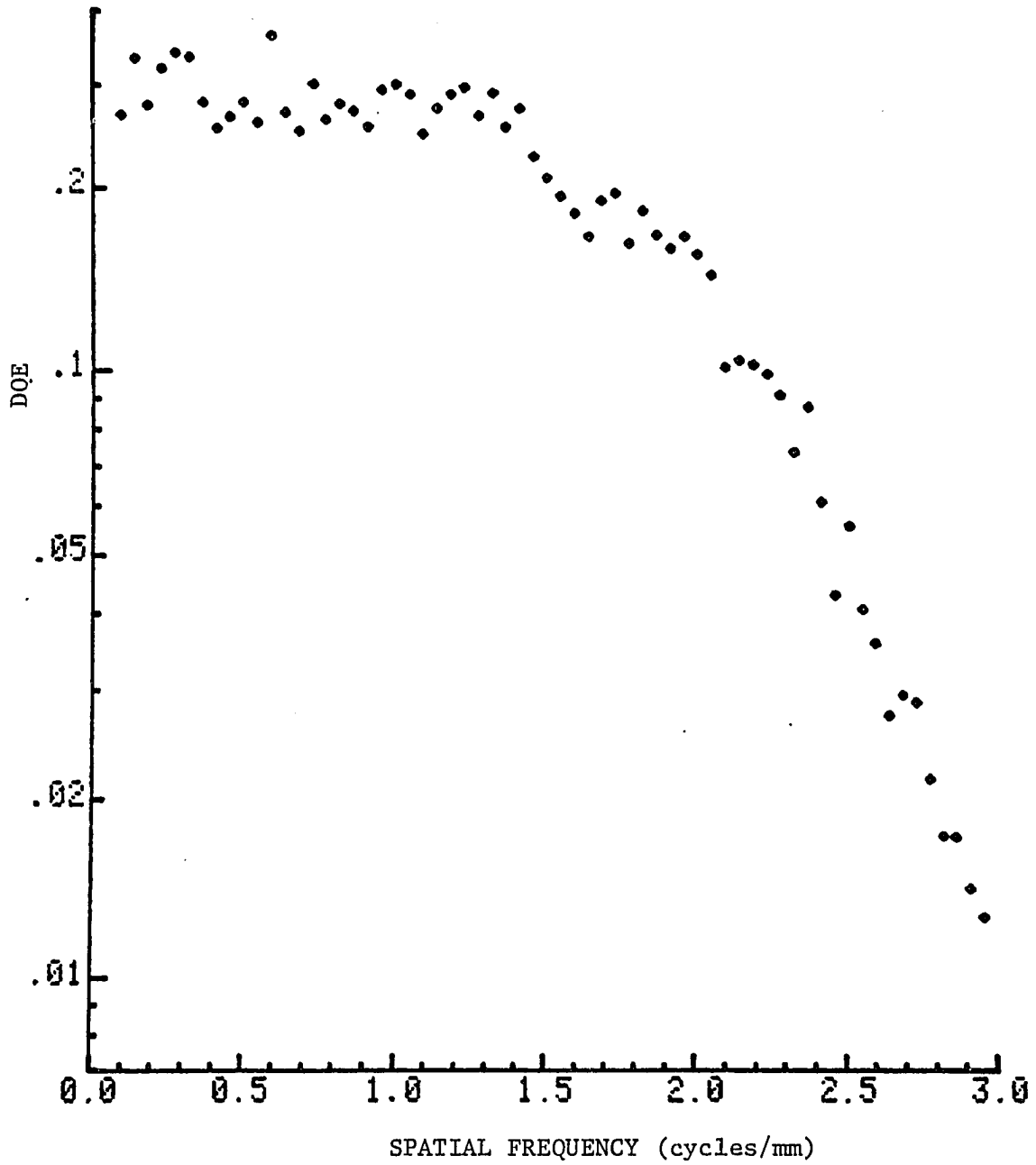


Fig. 5.18. Detective quantum efficiency of the experimental system.

So far, all experimental results presented in this chapter were obtained in an unconventional arrangement in order to study the details of the system. As noted in Chapter 4, an imaging lens was selected to provide an extraordinarily large optical magnification to overcome the limited digital storage format. The system was also operated at its maximum gain in order to study the detailed noise properties. Correspondingly, the x-ray exposure was relatively low as compared to the normal exposure level required for diagnostic radiographs. To study a system which resembles the ones currently in clinical use, the 400 mm imaging lens was replaced by a 135 mm lens, providing a magnification of 1.35 to match the intensifier's useful output diameter to that of the video camera tube. An x-ray exposure of 1 mR was used to simulate the practical situation. The lens was stopped down such that the same recording level used in previous experiments was obtained. Figure 5.19 shows the results. In this arrangement, the maximum frequency of 1.9 cycles/mm corresponds to the Nyquist sampling frequency of the 512x512 digital store format. One immediately notices that the information bandwidth is reduced to about 0.8 cycles/mm as compared to 2 cycles/mm in Figure 5.15. This reduction is caused by two basic parameters of the video camera tube, namely its resolution and its charge storage capacity. These two factors are reflected in this figure as poor system MTF and low system gain.

As previously discussed, information bandwidth is limited by baseline white noise. In other words, the system transfers the

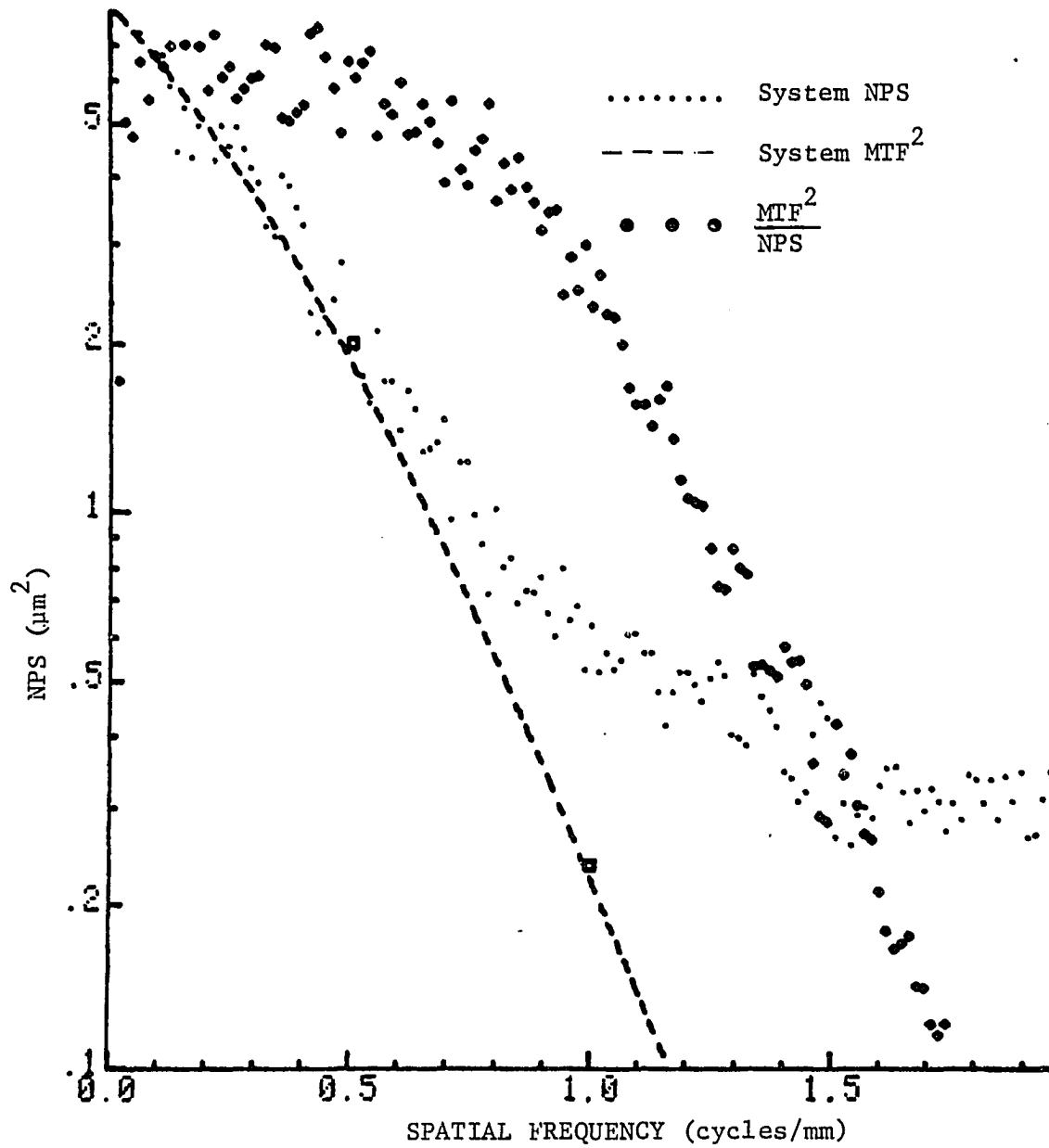


Fig. 5.19. Information transfer of a typical clinical system.

image information up to a frequency where the primary NPS component, resulting from the CsI layer, decreases to a level comparable to the baseline white noise. Since the ratio of these two noise components equals the system gain, this cutoff frequency, f_c , is reached when the product of the system gain and the system MTF^2 is near unity

$$g \text{ MTF}^2(f_c) = 1 . \quad (5.1)$$

Therefore, one can conclude that high system gain and high MTF^2 are essential for a high performance system. However, high system gain can be achieved only if the image recording device has a high storage capacity, as x-ray exposure cannot be sacrificed for a good quality radiograph.

We therefore return to Figure 5.19 to analyze the problems associated with the system currently in clinical use. A system gain of 15 is noted in this figure. With this low gain, the corresponding MTF at the cutoff frequency is 26% according to Equation 5.1. This rather high value indicates the inefficient utilization of the system MTF. This inefficiency is more pronounced if a 14" XR11 is used. In this case, the system gain is reduced to about 6 if the same exposure is used and the system quantum sink is approaching the video camera tube.

The MTFs of the system and XR11 are shown in Figure 5.20. This figure indicates that the system MTF is significantly affected by the camera tube. For convenience, we shall introduce another

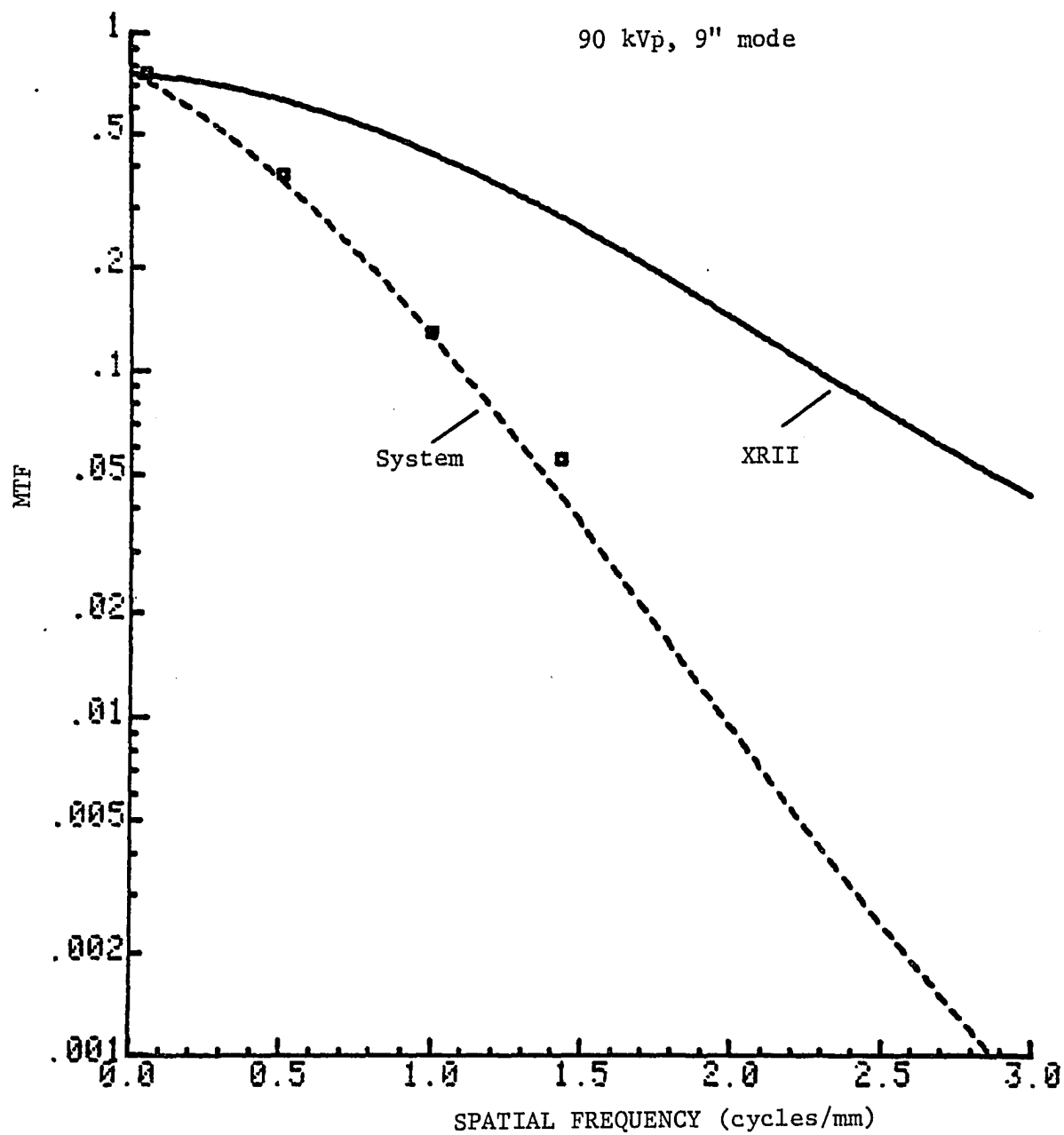


Fig. 5.20. Modulation transfer function of the XR11 and a typical clinical system.

frequency unit for the digitized image. As commonly used in the video industry, a TVL is defined as one-half cycle of a periodic object. The maximum frequency that can be recorded by the 512x512 digital format is then 512 TVLs per picture width. For the system under discussion, it corresponds to 1.9 cycles/mm as referred back to the system input. With this notion, the result shown is not surprising. For broadcasting applications, most camera tubes are intentionally designed to provide a 30 to 50% MTF at 400 TVLs to ensure camera stability when operated at a standard format. This frequency corresponds to an input frequency of 1.5 cycles/mm. Most modern XRIIs provide an appreciable amount of modulation transfer at this frequency.

One therefore realizes that the present system is limited by two critical parameters of the video tube, namely its MTF and charge storage capacity. These two limitations should be removed from a high performance system. Fortunately, these two requirements are running in parallel. Camera tubes with these capabilities exist in space applications. It should be pointed out that the readout time for a high capacity target must be proportionally extended due to the limited beam current. Therefore, no design effort should be spent to develop a system that serves for fluoroscopy and high quality radiography at the same time.

Based on these considerations, a Westinghouse 2" selenium vidicon is currently under study. Its square wave response is shown in Figure 5.21, indicating a modulation depth of 90% at 1000 TVLs.

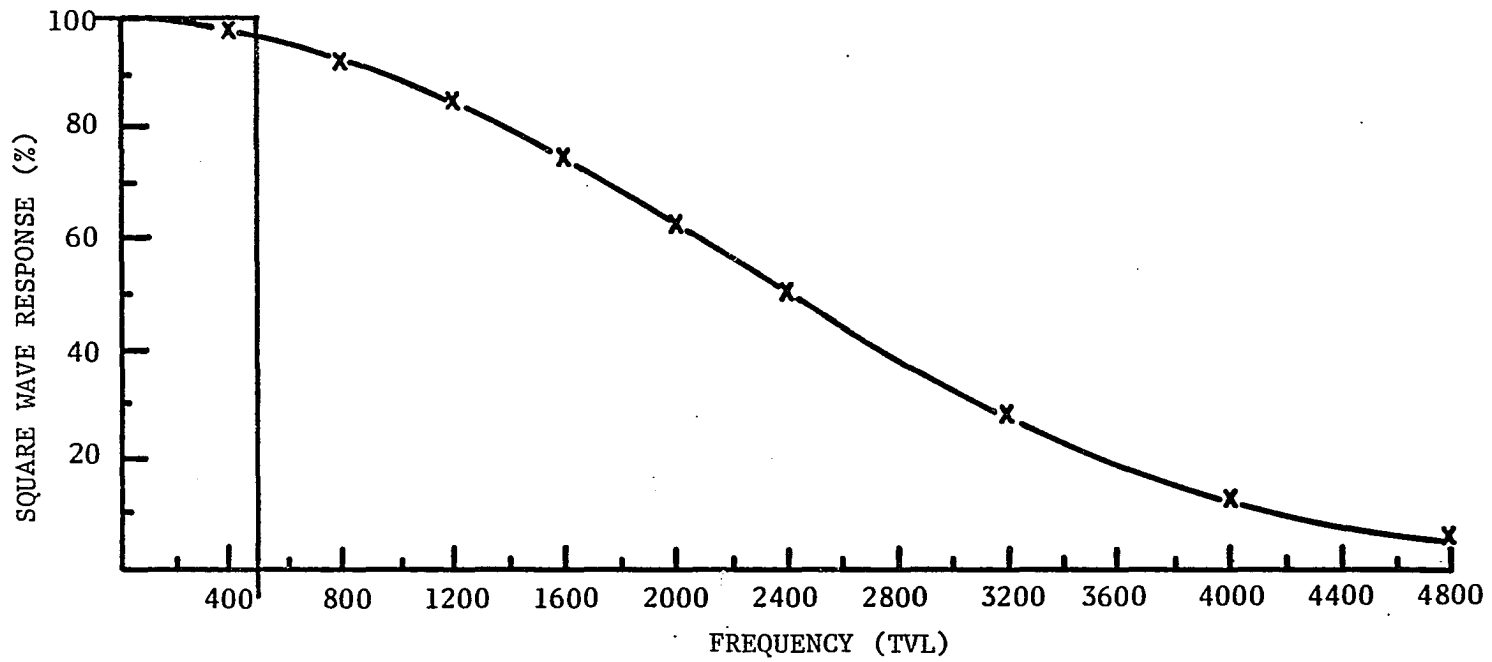


Fig. 5.21. Square wave response of selenium vidicon.

The charge capacity is at least ten times higher than that of commercial devices. When this tube is used in the new system, one can expect system performance to be limited solely by the XRII. This situation is rather similar to the experimental arrangement used in the study of image properties. Consequently, the information transfer efficiency shown in Figure 5.18 can be anticipated for such a system.

CHAPTER 6

CONCLUSION

Suggested Future Work

The analysis above indicates that a proper selection of the image pickup device will result in a system ultimately limited by the resolution capability of the x-ray image intensifier used. It is known that modern CsI sensors are capable of providing a limiting resolution of 10 cycles/mm which is well in excess of most high resolution screens with comparable x-ray detection efficiency. However, this high resolution capability is completely overshadowed by other XRII imaging mechanisms. As a result of the small output image format, both electron optics and the output phosphor contribute appreciably to resolution degradation. Using such a conventional construction, further improvement on resolution performance will be difficult. To meet the more stringent imaging tasks of general diagnostic procedures, an experimental PEID system is currently under investigation. In this system, the conventional XRII is replaced by a micro-channel plate (MCP) low-light-level image intensifier, fiber-optically coupled to an external CsI scintillator. The large output image format is fiber-optically minified to adapt to a number of CCD image arrays. Due to the discrete nature of image transfer, this system is limited essentially by the sampling density. However, the effect of the

noise properties of the MCP and the charge storage density of the CCD arrays on the system information transfer remains to be studied.

In the theoretical development of Chapter 3, an interesting question was raised regarding the film grain coupling effect on the noise power spectrum. Experimental study of this effect was not conclusive due to the dominant phosphor granularity in the XR11. For screen-film systems, wider noise power spectra were also observed and usually interpreted according to Lubberts' model (Sandrik and Wagner, 1982). However, no experimental data have been reported to confirm that the wider NPS is merely due to this screen thickness effect. As digital film radiography is evolving, one feels that the photographic film deserves more serious study regarding its effect on the noise power spectrum transferred by x-ray scintillation phosphors.

This film grain coupling effect can be analyzed if an extremely thin x-ray screen with fine phosphor grains is available. A thicker protective coating should be used to provide a blur size comparable to that in common use. With this screen sample, the NPS and the MTF^2 recorded on film can be compared to determine whether the grain coupling effect is significant.

A more quantitative study can be performed if the film sample is first prepared by a uniform pre-exposure in a controlled fashion, then exposed to the scintillation light outputs from the thin x-ray screen. Each scintillation light burst is recorded by the film grains which have effectively a lower average quantum threshold level.

As a function of the pre-exposure level, the strength of the coupling effect can be inferred from its corresponding NPS measurement.

Summary

Detective quantum efficiency as a system evaluation criterion was defined which weights the object power spectrum to determine the ultimate object detectability. Its scaling value was determined to be governed by x-ray transmission and absorption, and the scintillation processes within the XRII. The image information transfer was treated by considering the system to be composed of a series of independent frequency channels. Channel characteristics of image signal and noise transfers determine the useful information bandwidth of the system.

Five commercial CsI XRIIs were evaluated for their non-imaging performances as a function of five x-ray energies within the spectrum commonly used in diagnostic radiology. Results indicate that the performances of all practical intensifiers are alike, with DQE values ranging from 30 to 50% over the diagnostic x-ray spectrum. These rather satisfactory DQE values are primarily limited by the absorbing power of the CSI layer which is compromised for the image resolution. In addition, the experimental results show a general agreement with those calculated by a simple physical model. This evidence makes it possible that the intensifier be evaluated by numerical calculations provided that system parameters such as thickness and window composition are provided by the manufacturer.

Imaging properties such as signal-induced background, MTF, and NPS were investigated both theoretically and experimentally. The amount of x-ray scattering which degrades the information transfer was determined to be not greater than 3% in the worst case. The NPS components of the system were analyzed by a mathematical model and identified experimentally. The phosphor NPS component was proven negligible in all frequencies and there remain two dominant components resulting from the CsI scintillator and the final image recording medium. The CsI layer shows a potentially wide information bandwidth as a result of its needle-like structure. This inherent imaging efficiency can be achieved if the overall system is properly designed to minimize the effect of the final recording noise. Important design parameters for selecting a proper recording medium are its MTF and recording capacity. The low frequency data derived from the measurements of imaging properties further verify the analyses of the non-imaging properties.

Finally, an unconventional XRRI system was described which is anticipated to attain the requirements of general diagnostic procedures. In addition, methods for studying the film grain coupling effect on the recorded noise spectrum are suggested as the NPS is an important characteristic in determining the image information transfer of a digital imaging system.

APPENDIX A

DERIVATION OF THE INFORMATION FACTOR
RESULTING FROM AN X-RAY ENERGY DISTRIBUTION

Let us denote the resultant pulse height distribution by $P(z)$ with z standing for the number of output scintillation pulses. By its definition, Eq. (3.5), the information factor is given by

$$I = \frac{M_1^2}{M_0 M_2} = \frac{[\int zP(z)dz]^2}{\int P(z)dz \int z^2 P(z)dz} \quad (A.1)$$

In order to determine $P(z)$ from an x-ray energy distribution (XED), let us first define the following notations:

- ϵ : the x-ray photon energy,
- $\phi(\epsilon)$: the absorbed x-ray photon fluence, and
- $P_\epsilon(z, \epsilon)$: the scintillation distribution resulting from mono x-ray energy with

$$\int P_\epsilon(z, \epsilon) dz = 1. \quad (A.2)$$

For the monoenergetic scintillation distribution, the corresponding statistical moments are given by

$$\begin{aligned} M_{\epsilon 0}(\epsilon) &= \int P_\epsilon(z, \epsilon) dz = 1, \\ M_{\epsilon 1}(\epsilon) &= \int z P_\epsilon(z, \epsilon) dz, \text{ and} \\ M_{\epsilon 2}(\epsilon) &= \int z^2 P_\epsilon(z, \epsilon) dz. \end{aligned} \quad (A.3)$$

The corresponding scintillation information factor is then given

by

$$I_{\text{SCIN}}(\epsilon) = \frac{M_{\epsilon 1}^2(\epsilon)}{M_{\epsilon 2}(\epsilon)M_{\epsilon 0}(\epsilon)} = \frac{M_{\epsilon 1}^2(\epsilon)}{M_{\epsilon 2}(\epsilon)} \quad (\text{A.4})$$

With these notations, the resultant pulse height distribution $P(z)$

is expressed as

$$P(z) = \int \phi(\epsilon) P_{\epsilon}(z, \epsilon) d\epsilon \quad (\text{A.5})$$

Substituting Eq. (A.5) into (A.1), we obtain

$$\frac{1}{I} = \frac{\int \phi(\epsilon) P_{\epsilon}(z, \epsilon) z^2 dz d\epsilon \int \phi(\epsilon) P_{\epsilon}(z, \epsilon) dz d\epsilon}{\left[\int \phi(\epsilon) P_{\epsilon}(z, \epsilon) z dz d\epsilon \right]^2} \quad (\text{A.6})$$

Integrating z first, we have

$$\frac{1}{I} = \frac{\int \phi(\epsilon) M_{\epsilon 2}(\epsilon) d\epsilon \int \phi(\epsilon) d\epsilon}{\left[\int \phi(\epsilon) M_{\epsilon 1}(\epsilon) d\epsilon \right]^2} \quad (\text{A.7})$$

Using Eq. (A.4), the information factor can be expressed as

$$\begin{aligned} \frac{1}{I} &= \frac{\int \phi(\epsilon) M_{\epsilon 1}^2(\epsilon) \frac{1}{I_{\text{SCIN}}(\epsilon)} d\epsilon \int \phi(\epsilon) d\epsilon}{\left[\int \phi(\epsilon) M_{\epsilon 1}(\epsilon) d\epsilon \right]^2} \\ &= \frac{\int \phi(\epsilon) M_{\epsilon 1}^2(\epsilon) \frac{1}{I_{\text{SCIN}}(\epsilon)} d\epsilon}{\int \phi(\epsilon) M_{\epsilon 1}^2(\epsilon) d\epsilon} \frac{\int \phi(\epsilon) d\epsilon}{\left[\int \phi(\epsilon) M_{\epsilon 1}(\epsilon) d\epsilon \right]^2} \end{aligned} \quad (\text{A.8})$$

At this point, let us introduce two quantities:

$$\frac{1}{\bar{I}_{\text{SCIN}}} = \frac{\int \phi(\epsilon) M_{\epsilon 1}^2(\epsilon) \frac{1}{\bar{I}_{\text{SCIN}}(\epsilon)} d\epsilon}{\int \phi(\epsilon) M_{\epsilon 1}^2(\epsilon) d\epsilon} \quad (\text{A.9})$$

and

$$\frac{1}{\bar{I}_{\text{XED}}} = \frac{\int \phi(\epsilon) M_{\epsilon 1}^2(\epsilon) d\epsilon \int \phi(\epsilon) d\epsilon}{\left[\int \phi(\epsilon) M_{\epsilon 1}(\epsilon) d\epsilon \right]^2} \quad (\text{A.10})$$

The information factor can then be cascaded as

$$I = \bar{I}_{\text{SCIN}} I_{\text{XED}} \quad (\text{A.11})$$

To interpret these two quantities in words, one realizes that $M_{\epsilon 1}(\epsilon)$ is the mean number of scintillations resulting from a single x-ray energy ϵ . The averaged scintillation information factor \bar{I}_{SCIN} is derived from the scintillation "power" spectrum instead of the absorbed x-ray spectrum. On the other hand, the information factor (I_{XED}) inherent in the x-ray energy distribution is derived from the absorbed x-ray spectrum with corresponding moments defined by mean scintillations instead of x-ray energies.

APPENDIX B

THE NOISE POWER SPECTRUM OF A CASCADED LINEAR SYSTEM

In this appendix, the noise power spectrum of a cascaded linear imaging system will be derived by considering the information carriers as a series of impulses transferred through the system. At each stage, secondary events are generated with statistical distributions in number and in position. In the following derivation, the statistical functions are denoted by P and f for the number and position, respectively, with corresponding subscripts. With the exception of the primary photon stream, all the position functions can be treated as the point spread functions (PSF) of individual system components. For simplicity, position and frequency vectors are implied by their scalar notations. A Poisson random process is assumed for the primary photon stream. That is, the primary events are uniformly distributed in the image area A with the total number of events obeying Poisson's law.

Let us consider a single-stage system which is composed of a gain stage and a recording medium. The output can be expressed as the sum of a series of random impulses,

$$\underline{z}(\underline{r}) = \sum_i^N \left[\sum_j^{m_i} \delta(\underline{r} - \underline{r}_i - \underline{r}'_{ji}) \right] \quad (\text{B.1})$$

The symbol, \underline{z} , denotes a random variable,

\underline{N} is the number of detected primary events,

\underline{r}_i is the position of the primary event, i .

\underline{m}_i is the number of secondaries resulting from the primary event i , and

\underline{r}'_{ji} is the relative position of secondary event, j , from its primary i .

The autocorrelation function $R_z(r_0)$ is then given by

$$R_z(r_0) = \langle \underline{z}(r) \underline{z}(r+r_0) \rangle \quad (\text{B.2})$$

$$= \sum_N P_n(N) \left\langle \sum_i^N \sum_u^N \sum_j^{\underline{m}_i} \sum_v^{\underline{m}_u} \delta(r - \underline{r}_i - \underline{r}'_{ji}) \delta(r+r_0 - \underline{r}_u - \underline{r}'_{vu}) \right\rangle ,$$

where:

$P_n(N)$ is the probability function for the number of detected primaries, assumed to be a Poisson distribution, and

$\langle \rangle$ stands for an ensemble average over all the random variables.

Considering the second and third summations in Eq. (B.2), we may separate the discussion into two cases:

Case (1): $i = u$

In this case, $\underline{m}_i = \underline{m}_u = m$. Evaluating the ensemble average by corresponding probability functions, the self-term contributes to the autocorrelation function,

$$R_{z,1}(r_0) = \sum_N P_n(N) \sum_i^N \sum_m^{\infty} P_m(m) \int dr_1 \dots dr_N dr'_1 \dots dr'_m [f_n(r_1) \dots f_n(r_N)$$

$$f_m(r'_1) \dots f_m(r'_m) \sum_j^m \sum_v^m \delta(r - r_i - r'_j) \delta(r+r_0 - r_i - r'_v)] \quad (\text{B.3})$$

where $f_n(r_i)$ and $f_m(r'_j)$ are the position distributions of the primary and secondary events, respectively, with

$$f_n(r_i) = \frac{1}{A},$$

and

$$\int f_m(r'_j) dr'_j = 1. \quad (\text{B.4})$$

Performing the integration on r_i , we have

$$R_{z,1}(r_0) = \sum_N P_n(N) \sum_i^N \sum_m^\infty P_m(m) \frac{1}{A} \left[\sum_j^m \sum_v^m \int dr'_1 \dots dr'_m f_m(r'_1) \dots f_m(r'_m) \delta(r_0 + r'_j - r'_v) \right]. \quad (\text{B.5})$$

Considering the summations of j and v , we can further divide into two subcases:

a) For $j=v$, we have a simple δ function in Eq. (B.5) and

$$R_{z,1a}(r_0) = \sum_N P_n(N) \sum_i^N \sum_m^\infty P_m(m) \sum_j^m \left[\frac{1}{A} \delta(r_0) \right] = \frac{\bar{N} \bar{m}}{A} \delta(r_0). \quad (\text{B.6})$$

b) For $j \neq v$, by performing an integration on r'_v , we have

$$R_{z,1b}(r_0) = \sum_N P_n(N) \sum_i^N \sum_m^\infty P_m(m) \frac{1}{A} \sum_{\substack{j,v \\ j \neq v}}^m \int dr'_j f_m(r'_j) f_m(r_0 + r'_j) = \frac{\bar{N}(\bar{m}^2 - \bar{m})}{A} [f_m(r_0) \star f_m(r_0)], \quad (\text{B.7})$$

where \star denotes the autocorrelation integral.

Case (2): $i \neq u$

We now consider the cross interaction resulting from different primaries. Since the primary events are independent, we can evaluate the summations of i and u separately,

$$R_{z,2}(r_0) = \sum_N P_n(N) \left[\sum_i^N \sum_{m_i}^{\infty} P_{m_i}(m_i) \sum_j^{m_i} \int dr_i dr'_{ji} f_n(r_i) f_m(r'_{ji}) \delta(r-r_i-r'_{ji}) \right] \\ \left[\sum_{u \neq i}^N \sum_{m_u}^{\infty} P_{m_u}(m_u) \sum_v^{m_u} \int dr_u dr'_{vu} f_n(r_u) f_m(r'_{vu}) \delta(r+r_0-r_u-r'_{vu}) \right] \quad (\text{B.8})$$

Performing integrations on r_i and r_u within each bracket, we have

$$R_{z,2}(r_0) = \sum_N P_n(N) \left[\sum_i^N \sum_{m_i}^{\infty} P_{m_i}(m_i) \frac{m_i}{A} \right] \left[\sum_{u \neq i}^N \sum_{m_u}^{\infty} P_{m_u}(m_u) \frac{m_u}{A} \right] \\ = \sum_N P_n(N) \frac{N\bar{m}}{A} \frac{(N-1)\bar{m}}{A} \\ = \frac{(N^2 - \bar{N}) \bar{m}^2}{A^2} \\ = \frac{\bar{N}^2 - \bar{m}^2}{A^2}, \quad (\text{B.9})$$

since the primary obeys Poisson distribution.

Combining Eqs. (B.6), (B.7), and (B.9), we obtain the autocorrelation function

$$R_z(r_0) = q \bar{m} \delta(r_0) + q (\bar{m}^2 - \bar{m}) [f_m(r_0) \star f_m(r_0)] + q^2 \bar{m}^2, \quad (\text{B.10})$$

where $q = \frac{\bar{N}}{A}$ is the detected primary quantum fluence.

On the other hand, the output mean \bar{z} can be derived in a similar way as

$$\bar{z} = \langle z(r_0) \rangle = q \bar{m}. \quad (\text{B.11})$$

By using Eqs. (B.10) and (B.11), we obtain the autocorrelation function of the fluctuations about the mean

$$\begin{aligned} R_{\Delta z}(r_0) &= R_z(r_0) - \bar{z}^2 \\ &= q \bar{m} \delta(r_0) + q (\bar{m}^2 - \bar{m}) [f_m(r_0) \star f_m(r_0)]. \end{aligned} \quad (\text{B.12})$$

However, the quantity we are interested in is the relative fluctuation $\Delta z/z$. Its autocorrelation function is thus given by

$$\begin{aligned} R_{\Delta z/z}(r_0) &= \frac{R_z(r_0)}{\bar{z}^2} \\ &= \frac{\delta(r_0)}{q\bar{m}} + \left[\frac{1}{qI} - \frac{1}{q\bar{m}} \right] [f_m(r_0) \star f_m(r_0)]. \end{aligned} \quad (\text{B.13})$$

where

$$I = \frac{M_1^2}{M_0 M_2} = \frac{\bar{m}^2}{\bar{m}^2}$$

is the Swank's information factor as defined in Eq. (3.5).

The noise power spectrum of a single-stage system can be directly obtained by Fourier transformation of the autocorrelation function,

$$W_{\Delta z/z}(f) = \frac{1}{q\bar{m}} + \left(\frac{1}{q} \frac{1}{I} - \frac{1}{q\bar{m}} \right) |F(f)|^2, \quad (\text{B.14})$$

where $F(f)$ is the Fourier transform of $f_m(r_0)$, or the MTF of the gain stage.

We now extend this derivation to a two-stage system with the output represented by

$$z(r) = \sum_{i=1}^N \sum_{j=1}^{m_1} \sum_{k=1}^{m_2} \delta(r - r_{i,j,k}) \quad (\text{B.15})$$

Parallel to Eq. (B.2), the autocorrelation function is given by

$$R_z(r_0) = \sum_N P_n(N) \langle \sum_{i=1}^N \sum_{j=1}^{m_1} \sum_{k=1}^{m_2} \sum_{u=1}^N \sum_{v=1}^{m_1} \sum_{w=1}^{m_2} \delta(r - r_{i,j,k} - r' - r'_{u,v,w}) \rangle. \quad (\text{B.16})$$

By a similar approach, we divide our discussion into two cases:

Case (1): $i = u$

Performing the integration on r_i , we have

$$R_{z,1}(r_0) = \sum_N P_n(N) \frac{N}{A} \sum_{m_1} P_{m_1}(m_1) \sum_{j=1}^{m_1} \sum_{v=1}^{m_1} \sum_{k=1}^{m_2} \sum_{w=1}^{m_2} \int dr'_j dr'_{k'} dr'_{v'} dr'_{w'} \quad (\text{B.17})$$

$$f_{m_1}(r'_j) f_{m_2}(r'_{k'}) f_{m_1}(r'_{v'}) f_{m_2}(r'_{w'}) \delta(r_0 + r'_j + r'_{k'} - r'_{v'} - r'_{w'})$$

where the ensemble average applies to m_{2j} and m_{2v} .

The discussion will further be nested into higher indices.

Let us consider the summation over j and v :

a) For $j = v$, we have

$$R_{z,1a}(r_0) = q\bar{m}_1 \left\langle \sum_k^{\bar{m}_2} \sum_w^{\bar{m}_2} \int dr_k' dr_w' f_{m_2}(r_k') f_{m_2}(r_w') \delta(r_0 + r_k' - r_w') \right\rangle \quad (\text{B.18})$$

i) For $k = w$, the ensemble average is given by

$$\sum_{m_2}^{\infty} P_{m_2}(m_2) m_2 \delta(r_0) = \bar{m}_2 \delta(r_0) \quad (\text{B.19})$$

ii) For $k \neq w$, the corresponding term is given by

$$(\bar{m}_2^2 - \bar{m}_2) [f_{m_2}(r_0) \star f_{m_2}(r_0)] \quad (\text{B.20})$$

b) For $j \neq v$. Integrating r_v' in Eq. (B.17), we obtain

$$\begin{aligned} R_{z,1b}(r_0) &= q \sum_{m_1}^{\infty} P_{m_1}(m_1) (m_1^2 - m_1) \left\langle \sum_k^{\bar{m}_2} \sum_w^{\bar{m}_2} \int dr_j' dr_k' dr_w' \right. \\ &\quad \left. f_{m_1}(r_j') f_{m_1}(r_0 + r_j' + r_k' - r_w') f_{m_2}(r_k') f_{m_2}(r_w') \right\rangle \\ &= q (\bar{m}_1^2 - \bar{m}_1) \sum_{m_{2j}}^{\infty} P_{m_2}(m_{2j}) m_{2j} \sum_{m_{2v}}^{\infty} P_{m_2}(m_{2v}) m_{2v} \\ &\quad [f_{m_1}(r_0) \star f_{m_1}(r_0)] \star [f_{m_2}(r_0) \star f_{m_2}(r_0)] \\ &= q (\bar{m}_1^2 - \bar{m}_1) \bar{m}_2^2 [f_{m_1} \star f_{m_1}](r_0) \star [f_{m_2} \star f_{m_2}](r_0), \quad (\text{B.21}) \end{aligned}$$

where \star denotes the convolution integral.

We now go to Case 2 where the contribution results from different primary events.

Case (2): $i \neq u$

This case has a similar form as that of the single-stage system because of the statistical independence of the primary events. Due to the length of the expression, we will simply give the result here,

$$R_{z,2}(r_0) = q^2 \bar{m}_1^{-2} \bar{m}_2^{-2} . \quad (\text{B.22})$$

As well, the mean value of z is given by

$$\bar{z} = q \bar{m}_1 \bar{m}_2 . \quad (\text{B.23})$$

Following the same approach as in a single-stage system, the autocorrelation function of the relative fluctuation $\Delta z/z$ is given by

$$\begin{aligned} R_{\Delta z/z}(r_0) &= \frac{\delta(r_0)}{q \bar{m}_1 \bar{m}_2} + \frac{\bar{m}_2^{-2} - \bar{m}_2}{q \bar{m}_1 \bar{m}_2^{-2}} [f_{m2}(r_0) \star f_{m2}(r_0)] \\ &\quad + \frac{\bar{m}_1^{-2} - \bar{m}_1}{q \bar{m}_1^{-2}} [f_{m1} \star f_{m1}] \star [f_{m2} \star f_{m2}](r_0) \\ &= \frac{\delta(r_0)}{q \bar{m}_1 \bar{m}_2} + \left(\frac{1}{q \bar{m}_1 I_1} - \frac{1}{q \bar{m}_1 \bar{m}_2} \right) [f_{m2} \star f_{m2}](r_0) \\ &\quad + \left(\frac{1}{q I_1} - \frac{1}{q \bar{m}_1} \right) [f_{m1} \star f_{m1}] \star [f_{m2} \star f_{m2}](r_0) , \end{aligned} \quad (\text{B.24})$$

where I_1 and I_2 are the information factors of the first and second stage statistics, respectively.

The noise power spectrum is then given by

$$W_{\Delta z/z}(f) = \frac{1}{q \bar{m}_1 \bar{m}_2} + \left(\frac{1}{q \bar{m}_1 I_2} - \frac{1}{q \bar{m}_1 \bar{m}_2} \right) |F_2(f)|^2 + \left(\frac{1}{q I_1} - \frac{1}{q \bar{m}_1} \right) |F_1(f)|^2 |F_2(f)|^2, \quad (\text{B.25})$$

where $F_1(f)$ and $F_2(f)$ are the Fourier transforms of $f_{m1}(r_0)$ and $f_{m2}(r_0)$, respectively, and can be interpreted as the MTFs of the two stages.

Rearranging the order in Eq. (B.25), we have for a two-stage system,

$$W_{\Delta z/z}(f) = \frac{1}{q} \left[\left(\frac{1}{I_1} - \frac{1}{\bar{m}_1} \right) |F_{12}(f)|^2 + \frac{1}{\bar{m}_1} \left(\frac{1}{I_2} - \frac{1}{\bar{m}_2} \right) |F_2(f)|^2 + \frac{1}{\bar{m}_1 \bar{m}_2} \right], \quad (\text{B.26})$$

where $F_{12}(f)$ is the combined MTF of first and second stages.

With its systematic appearance, Eq. (B.26) can be generalized to an n-stage system,

$$\begin{aligned}
W_{\Delta z/z}(f) = \frac{1}{q} & \left[\left(\frac{1}{I_1} - \frac{1}{\bar{m}_1} \right) |F_{1n}(f)|^2 + \frac{1}{\bar{m}_1} \left(\frac{1}{I_2} - \frac{1}{\bar{m}_2} \right) |F_{2n}(f)|^2 \right. \\
& \left. + \dots + \frac{1}{\bar{m}_1 \dots \bar{m}_{n-1}} \left(\frac{1}{I_n} - \frac{1}{\bar{m}_n} \right) |F_{nn}(f)|^2 + \frac{1}{\bar{m}_1 \dots \bar{m}_n} \right],
\end{aligned}
\tag{B.27}$$

where $F_{in}(f)$ is the MTF cascaded from the i^{th} stage through the system.

For an ideal system where each system component introduces no statistical fluctuation and no image blur, we have

$$\begin{aligned}
I_i &= 1, \text{ and} \\
F_{in}(f) &= 1, \quad i = 1, 2, \dots, n.
\end{aligned}
\tag{B.28}$$

In this ideal case, the noise power spectrum results solely from the detected photon stream, as given by

$$W_{\Delta z/z}^0(f) = \frac{1}{q}.
\tag{B.29}$$

With this in mind, the contents of the brackets in Eq. (B.27) can be interpreted as the inverse of the system information factor as a function of spatial frequency. For a non-imaging detector, the system information factor I is given as the special case at zero frequency,

$$\begin{aligned}
\frac{1}{I} &= \frac{W_{\Delta z/z}(f=0)}{0} \\
&\quad W_{\Delta z/z} \\
&= \left(\frac{1}{I_1} - \frac{1}{\bar{m}_1}\right) + \frac{1}{\bar{m}_1} \left(\frac{1}{I_2} - \frac{1}{\bar{m}_2}\right) + \frac{1}{\bar{m}_1 \bar{m}_2} \left(\frac{1}{I_3} - \frac{1}{\bar{m}_3}\right) \\
&+ \dots + \frac{1}{\bar{m}_1 \dots \bar{m}_{n-1}} \left(\frac{1}{I_n} - \frac{1}{\bar{m}_n}\right) + \frac{1}{\bar{m}_1 \dots \bar{m}_n} .
\end{aligned} \tag{B.30}$$

Rearranging the terms, we have

$$\begin{aligned}
\frac{1}{I} &= \frac{1}{I_1} + \frac{1}{\bar{m}_1} \left(\frac{1}{I_2} - 1\right) + \frac{1}{\bar{m}_1 \bar{m}_2} \left(\frac{1}{I_3} - 1\right) \\
&+ \dots + \frac{1}{\bar{m}_1 \dots \bar{m}_{n-1}} \left(\frac{1}{I_n} - 1\right) ,
\end{aligned} \tag{B.31}$$

as used in Eq. (3.6).

REFERENCES

- Capp, M. P., S. Nudelman, H. D. Fisher, T. W. Ovitt, G. Pond, M. M. Frost, H. Roehrig, J. Seeger, and D. Ouimette. 1981. Photoelectronic radiology department. Proc. SPIE 314:2-8.
- Charman, W. N. and A. Olin. 1965. Tutorial-image quality criteria for aerial camera systems. Photo. Sci. Eng. 9(6):385-397.
- Christenson, P. C., T. W. Ovitt, H. D. Fisher, M. M. Frost, S. Nudelman, and H. Roehrig. 1980. Intravenous angiography using digital video subtraction: intravenous cervicocerebrovascular angiography. Am. J. Nucl. Radiol. 1:379-386.
- Dainty, J. C. and R. Shaw. 1974. Image Science. Academic Press, London.
- Fano, R. M. 1968. Transmission of information: a statistical theory of communications M.I.T. Press, Massachusetts Institute of Technology, Cambridge, Massachusetts.
- Hoffman, E. J. and M. E. Phelps. 1974. Production of monoenergetic x-rays from 8 to 87 keV. Phys. Med. Biol. 19(1):19-35.
- Johns, H. E. and J. R. Cunningham. 1981. The physics of radiology, 3rd. ed. Thomas Publisher, Springfield, Illinois.
- Johnson, J. Image Intensifier Symposium held at Fort Belvoir, Va., Oct. 6-7, 1958, AD 220160.
- Lubberts, G. 1968. Random noise produced by x-ray fluorescent screens. J. Opt. Soc. Am. 58:1475.
- Nudelman, S. 1983. Photoelectronic-digital radiology: past, present, and future. Digital imaging in cardiovascular radiology, P. H. Heintzen and R. Brennecke, eds. Thieme-Stratton Inc., New York.
- Plechaty, E. F., D. E. Cullen, and R. J. Howerton. 1975. Tables and graphs of photon interaction cross sections from 1 keV to 100 Mev derived from the LLL evaluated nuclear data library. UCRL-50400, vol. 6, Revision 1, Oct. 31, 1975, University of California, Livermore, California.
- Roehrig, H., B. Lum, H. D. Fisher, D. Ouimette, M. P. Capp, M. M. Frost, and S. Nudelman. 1979. Digital method to evaluate the noise of x-ray image intensifiers. Proc. SPIE 206:135-145.

- Rose, A. 1946. A unified approach to the performance of photographic film, television pickup tubes, and the human eye. *J. Soc. Motion Picture Television Engrs.* 47:273-294.
- Rose, A. 1948. The sensitivity performance of the human eye on an absolute scale. *J. Opt. Soc. Am.* 38:196-208.
- Rosell, F. A. 1969. Limiting resolution of low-light-level imaging sensors. *J. Opt. Soc. Am.* 59(5):539-547.
- Rosell, F. A. and R. H. Willson. 1973. Recent psychophysical experiments and the display signal-to-noise ratio concept. Perception of displayed information, L. M. Biberman ed. Plenum, New York.
- Sandrik, J. M. and R. F. Wagner. 1982. Absolute measures of physical image quality: measurement and application to radiographic magnification. *Med. Phys.* 9:540.
- Shannon, C. E. 1948. A mathematical theory of communication. *Bell Syst. Tech. J.* 27:379, 623.
- Stahnke, I. and H. Heinrich. 1966. Special problems in measuring the modulation transfer function of x-ray image intensifiers. Advances in electronics and electron physics, vol. 22A, L. Marton ed. Academic Press, New York.
- Vosburgh, K. G., R. K. Swank, and J. M. Houston. 1977. X-ray image intensifiers. Advances in electronics and electron physics, vol. 43, L. Marton ed. Academic Press, New York.
- Wiener, N. 1949. Extrapolation, interpolation, and smoothing of stationary time series with engineering applications. John Wiley, New York.